Title

Cytotoxic Conditioning-Induced Changes in Bone Marrow Microenvironment: A Study in Wild-Type and AML Mouse Models

Author

ABBASIZADEH, NASTARAN

Publication Date

2024

Peer reviewed|Thesis/dissertation

UNIVERSITY OF CALIFORNIA, MERCED

Cytotoxic Conditioning-Induced Changes in Bone Marrow Microenvironment: A Study in Wild-Type and AML Mouse Models

A dissertation submitted in partial satisfaction of the requirements for the degree Doctor.

of Philosophy in Quantitative and Systems Biology

by

Nastaran Abbasizadeh

Committee in charge:

Professor Jennifer O. Manilay, Chair

Professor Kara McCloskey

Professor Changqing Li

Professor Joel A. Spencer

2024

The Dissertation of Nastaran Abbasizadeh is approved, and it is acceptable in quality and form for publication on microfilm and electronically:

_____

Dr. Joel A. Spencer

_____

Dr. Kara McCloskey

_____

Dr. Changqing Li

_____

Dr. Jennifer O. Manilay, Chair

University of California, Merced

2024

DEDICATION

To my loving family, who have been my source of support and encouragement throughout this academic journey. Despite the physical distance that separated us across borders, your always unwavering belief in me reminds me that the bonds of family are not confined by geography. I also would like to express my heartfelt appreciation to my beloved, Omid, whose unlimited emotional support, patience, and understanding sustained me throughout the challenges that I faced during doctoral experience.

TABLE OF CONTENTS

LIST OF ABBREVIATIONS

Hematopoietic stem cells (HSCs)

Bone marrow (BM)

Acute myeloid leukemia (AML)

Low intensity (LI)

High intensity (HI)

Endothelial cells (ECs)

Busulfan/ Cyclophosphamide (BU/CY)

Minimal residual disease (MRD)

Osteoblasts (OBs)

Osteocytes (OTs)

Osteoclasts (OCs)

Mesenchymal stem cells (MSC)

Transforming growth factor beta (TGF-β)

Hypoxia-inducible factor (HIF)

Wingless-int (Wnt)

Stem cell factor (SCF)

Leukemia inhibitory factor (LIF)

Interleukin-3 (IL-3)

Interleukin-6 (IL-6)

Growth factor independent-1 (GFI-1)

Runt-related transcription factor-1 (RUNX1)

Vascular endothelial growth factor (VEGF)

Long-term subset (LT-HSC)

Short-term subset (ST-HSC)

Multipotent progenitors (MPPs)

Common myeloid progenitors (CMP)

Common lymphoid progenitors (CLP)

Granulocyte-macrophage progenitors (GMPs)

Megakaryocyte-erythrocyte progenitors (MEPs)

Dendritic cells (DCs)

Natural killer (NK)

C-X-C motif chemokine ligand 12 (CXCL12)

Acute lymphoblastic leukemia (ALL)

Chronic myeloid leukemia (CML)

Chronic lymphoblastic leukemia (CLL)

Pre-leukemic stem cells (pre-LSCs)

Leukemic stem cell (LSC)

Nitric oxide (NO)

Nuclear factor-kappa B (NF-kB)

Sympathetic nervous system (SNS)

Beta-2 adregenic receptor (B2-adrenergic)

Interleukin-1 (IL-1)

Colony stimulating factors (CSF)

C-X-C chemokine receptor type 4 (CXCR4)

Very late antigen-4 (VLA-4)

De novo AML (dn-AML)

Secondary AML (s-AML)

Myelodysplasia-related changes AML (AML-MRC)

Therapy-related AML (t-AML)

Myelodysplastic syndrome (MDS)

Myeloproliferative neoplasm (MPN)

FLT3 internal tandem duplications (FLT3-ITD)

Center for international blood and marrow transplant research (CIBMTR)

Hematopoietic stem cell transplantation (HCT)

Overall survival (OS)

Myeloablative conditioning (MAC)

Reduced intensity conditioning (RIC)

Nonmyeloablative conditioning (NMA)

Total body irradiation (TBI)

Gray (Gy)

T regulatory cells (Treg)

Transplant-related mortality (TRM)

Chronic graft-versus-host disease (GVHD)

Graft-versus-tumor (GVT)

Cytarabine (Ara-C)

FMS-like tyrosine kinase 3 (FLT3)

Arteriolar endothelial cells (AECs)

Sinusoid endothelial cells (SECs)

Hematopoietic stem and progenitor cells (HSPCS)

Vascular endothelial growth factor receptor 2 (VEGFR2)

Tyrosine kinase with immunoglobulin and epidermal growth factor homology domains 2 (Tie2)

Osteopontin (OPN)

Two-photon (2P)

Reactive oxygen species (ROS)

Deoxyribonucleic acid (DNA)

Green fluorescent protein (GFP)

Department of Animal Research Services (DARS)

Institutional Animal Care and Use Committee (IACUC)

Intraperitoneal injection (IP)

Dimethyl sulfoxide (DMSO)

Phosphate buffer solution (PBS)

Fluorescence-activated cell sorting (FACS)

Ammonium-chloride -potassium (ACK)

Peripheral blood (PB)

Dipotassium ethylenediaminetetraacetic acid (K2EDTA)

Dihydrogen oxide H2O (Di H2O)

Rpm (rotations per minute)

Red blood cell (RBC)

Allophycocyanin-cyanine7 (APC/Cy7)

Peridinin chlorophyll protein-cyanine5 (PerCP/Cy5)

Field of view (FOV)

Second harmonic generation (SHG)

Numerical aperture (NA)

Paraformaldehyde (PFA)

Optimal cutting temperature (OCT)

Line scanning particle image velocimetry (LSPIV)

Deposition type (D-type)

Mixed type (M type)

Resorption type (R-type)

Max intensity projections (MIP)

Granulocyte-macrophage colony-stimulating factor (GM-CSF)

Stromal cell-derived factor-1 (SDF-1)

Neural/glial antigen 2 (NG2)

Platelet-derived growth factor (PDGFB+)

Bone formation rate (BFR)

Bone surface (BS)

Mineral apposition rate (MAR)

University of California Cancer Research Coordinating Committee (UC CRCC)

Stem Cell Instrumentation Foundry (SCIF)

Two-photon phosphorescence lifetime microscopy (2PLM)

Partial pressure of oxygen (pO_2)

Millimeter of mercury (mmHg)

Electron paramagnetic resonance (EPR)

Electro-optic modulator (EOM)

Photomultiplier tube (PMT)

Complete remission (CR)

Allogeneic hematopoietic cell transplantation (alloHCT)

Membrane-tomato/membrane-green (mTmG)

Enhanced green fluorescent protein (EGFP)

Fetal bovine serum (FBS)

Tandem-dimer-tomato (TdTomato)

Infrared (IR)

Standard deviation (SD)

Patient-Derived Xenograft (PDX)

LIST OF SYMBOLS

α alpha

β beta

° degree

μ micro

+ positive expression

- negative expression

LIST OF FIGURES

LIST OF TABLES

Table 1. List of Fluorescent-Labeled Antibodies Used for Flow cytometry and Imaging.

Antigen	Clone	Fluorophore	Source
CD 31	MEC13.3	Alexafluor 647	Biolegend
CD144	BV9	Alexafluor 647	Biolegend
Sca-1	D7	Alexafluor 647	Biolegend
CD45.2	104	APC/Cy7	Biolegend
CD45.1	A20	PerCP/Cy5	Biolegend
CD19	6D5	PerCP-Cy5.5	Biolegend
CD11b	M1/70	APC-CY7	Biolegend
Gr-1	RB6-8C5	PE/Cy7	Biolegend
CD3	145-2C11	APC	Biolegend
CD4	RM4-5	PE-Cy7	Biolegend
CD25	M-A251	PerCP-Cy5.5	Biolegend
Ob-R Leptin	B-3	Alexafluor 594	Santa Cruz Biotechnology

ACKNOWLEDGEMENT

The research and findings shared in this dissertation have been made achievable through the collective efforts of numerous people. I am deeply appreciative of my advisor, Dr. Joel Spencer, whose support and expertise have been a cornerstone during my time in his lab. Throughout my Ph.D. journey, he served as an exceptional mentor not only in the scientific realm but also as a guiding person in my personal life. His profound empathy and support were especially invaluable during the difficult times I faced, particularly in light of the tragedies affecting my home country. His sympathy, both in words and actions, was a deeply cherished aspect of my doctoral experience.

I wish to thank my committee members Dr. Jennifer O. Manilay, Dr. Kara McCloskey, and Dr. Changqing Li for their guidance and support throughout my Ph.D. Their expertise, feedback, and commitment to my academic growth have been influential in shaping the success of this work. My sincere thanks to Dr. Jennifer O. Manilay lab, especially Dr. Betsabel Chicana and Janna Emery for always being available to assist me with my questions and needs. Their willingness to share their knowledge, provide guidance, and lend a helping hand has been an essential part of my research journey.

I would like to extend my thanks to the members of our lab, my colleagues, Christian Burns and Kai Siang Hu whose collaborative spirit have made our lab a welcoming and productive environment, and I am truly appreciative of the sense of teamwork we have fostered. Thanks to my undergrads Farhad Ghazali, Ruth Verrinder, Orlando Hernandez, Marlene Marquez Villanueva, Zeth Carmona and Robert Dudkin for not only affording me the privilege of mentorship experience but also for their contributions to my experiments and data analysis.

Moreover, I would like to acknowledge Dr. David Gravano from the Stem Cell Instrumentation Foundry (SCIF) for his supportive nature towards all the people, including me. Thanks to the staff of the Department of Animal Research Services (DARS) for their expertise in animal care and technical support. I cannot express my gratitude enough for all the other people, my family, and friends, who played a part in my Ph.D. journey and facilitated my transition from this stage of my life to the next.

FUNDING, COPYRIGHTS, AND CONTRIBUTIONS

CHAPTER 1-4

This work was funded by the University of California Cancer Research Coordinating Committee (CRCC) grant and Center for Cellular and Biomolecular Machines (CCBM) graduate fellowship.

CHAPTER 2: Age and Dose Dependent Changes to the Bone Marrow Microenvironment after Cytotoxic Conditioning with Busulfan

This section is a copy of my manuscript ready to submit in BioRxiv. All the experimental data collected and images generated by Nastaran Abbasizadeh. Christian Burns, Farhad Ghazali, Ruth Verrinder, and Negar Seyedhasantehrani contributed to data analysis.

Abbasizadeh N., Burns CS., Verrinder R., Ghazali F., Seyedhassantehrani N., Spencer JA., (2024), Age and Dose Dependent Changes to the Bone Marrow Microenvironment after Cytotoxic Conditioning with Busulfan.

Part of the project focusing on investigation of BM partial pressure of oxygen (pO_2) measurement through 2 photon phosphorescence microscopy was unpublished. Nastaran Abbasizadeh, Christian Burns, Ruth Verrinder, and Mario Muniz conducted the groundwork for this work. More information will be provided under the unpublished section of this chapter. One chapter on this subject has been published in the book titled "Optical Imaging in Human Disease and Biological Research."

Abbasizadeh, N., & Spencer, J. A. (2021). Two-Photon Phosphorescence Lifetime Microscopy. In *Optical Imaging in Human Disease and Biological Research* (pp. 63-82). Springer, Singapore.

CHAPTER 3: Evaluation of the Bone Marrow Microenvironment Around Resistant AML Cells before and after Cytotoxic Conditioning.

Abbasizadeh N., Hernandez O., Marquez Villanueva M., Dudkin R., Burns CS., Spencer JA., (2023), Evaluation of the Bone Marrow Microenvironment around MRD AML Cells After Cytotoxic Conditioning with Busulfan/Cyclophosamide", (under preparation).

All the experimental data and analysis collected by Nastaran Abbasizadeh with assistance of Orlando Hernandez, Marlene Marquez Villanueva, Robert Dudkin, and Christian Burns.

CHAPTER 4: Future Directions and Conclusions

CURRICULUM VITAE

EDUCATION

- **2019-2024:**
  Doctor of Philosophy, Quantitative and Systems Biology, University of California at Merced, CA, USA
- **2019-2022:**
  Master of Science, Quantitative and Systems Biology, University of California at Merced, CA, USA
- **2014-2017:**
  Master of Science, Nanobiotechnology, Department of Life Science Engineering, Tehran university, Iran
- **2010-2014:**
  Bachelor of the science, Biotechnology, Chemistry department, Kashan university, Kashan, Iran
- **2006-2010:**
  Bachelor of the science, Health Care Services Management, Isfahan University of Medical Sciences and Health Services, Isfahan, Iran

RESEARCH & PROFESSIONAL EXPERIENCE

- **2020-2024** Joel A. Spencer, Jennifer O. Manilay (UC Merced)
  Contribution to a R15 NIH grant titled "Exploring the B cell microenvironment in von-Hippel Lindau (Vhl) Dmp1-specific knockout mice".

- **2019-2024** Joel A. Spencer (UC Merced)
  Conducting my Ph.D. project under a Cancer Research Coordinating Committee (CRCC) grant titled "Investigation of microenvironmental changes to the bone marrow after cytotoxic conditioning in wild-type and AML mouse model".

- **2018-2019** Jessica Yue Wang (UC Merced)
  Conducting the study on Stereolithography (SLA) printing/interfacial polymerization coupling for the fabrication of conductive hydrogels.

- **2014-2016** Ali Hossein Rezayan (Tehran University)
  Conducting my master research on HHC-36 antimicrobial peptide loading on silk fibroin (SF)/hydroxyapatite (HA) nanofibrous- coated implants for the enhancement of osteoblast and bactericidal functions.

- **2015-2016** Hamid Reza Bakhsheshi-Rad
  Contribution to the project titled "Synthesis of novel nanostructured bredigite–amoxicillin scaffolds for bone defect treatment: Cytocompatibility and antibacterial activity".

- **2011-2013** Hossein Ali Rafiepour
  Undergrad research assistant in the lab to design a biosensor enabling detection of the Breast cancer-bearing antigen, Biotechnology laboratory, Kashan University

PUBLICATIONS

- **Abbasizadeh, N.**, Hernandez, O., Marquez Villanueva, M., Dudkin, R., Burns, CS., Spencer, JA., (2023), Evaluation of the Bone Marrow Microenvironment around MRD AML Cells After Cytotoxic Conditioning with Busulfan/Cyclophosamide", (In preparation).

- **Abbasizadeh, N.**, Burns, CS., Verrinder, R., Ghazali, F., Seyedhassantehrani, N., Spencer, JA., Age and dose dependent changes to the bone marrow microenvironment after cytotoxic conditioning with Busulfan, Ready to submit in bioRxiv; (2024).

- Seyedhassantehrani, N., Burns, CS., Verrinder, R., Okafor, V., **Abbasizadeh, N.**, Spencer, JA., Intravital Two-Photon Microscopy of the Native Thymus. bioRxiv; (2023). p. 2023.04.10.536267.

- Chicana, B., **Abbasizadeh, N.**, Burns, C., Taglinao, H., Spencer, J. A., & Manilay, J. O. (2022). Deletion of Vhl in Dmp1-expressing cells causes microenvironmental impairment of B cell lymphopoiesis. Frontiers in immunology, 13.

- **Abbasizadeh, N.**, & Spencer, J. A. (2021). Two-Photon Phosphorescence Lifetime Microscopy. In *Optical Imaging in Human Disease and Biological Research* (pp. 63-82). Springer, Singapore.

- Jordan, R. S., Frye, J., Hernandez, V., Prado, I., Giglio, A., **Abbasizadeh, N.**, ... & Wang, Y. (2021). 3D printed architected conducting polymer hydrogels. *Journal of Materials Chemistry B*.

- **Abbasizadeh, N.**, Rezayan, A. H., Nourmohammadi, J., & Kazemzadeh-Narbat, M. (2019). HHC-36 antimicrobial peptide loading on silk fibroin (SF)/hydroxyapatite (HA) nanofibrous-coated titanium for the enhancement of osteoblast and bactericidal functions. *International Journal of Polymeric Materials and Polymeric Biomaterials*.

- Bakhsheshi-Rad, H. R., Hamzah, E., **Abbasizadeh, N.**, Najafinezhad, A., & Kashefian, M. (2018). Synthesis of novel nanostructured bredigite–amoxicillin scaffolds for bone defect treatment: cytocompatibility and antibacterial activity. *Journal of Sol-Gel Science and Technology*, *86*, 83-93.

HONORS & AWARDS

- QSB Graduate Dean's Dissertation fellowship, spring **2024**.
- CCBM Training grant award, fall **2023**.
- CCBM fellowship, fall **2023**.
- CCBM travel grant award, **2022** and **2023**.
- QSB travel grant award, **2022** and **2023**.
- UCSB Bioengineering Symposium travel Award, Summer **2022**.
- ORED Core Facilities Seed Grant, summer **2022**.
- MBSE Bobcat Fellowship, summer **2019**.
- Highest ranking Master student in Nanobiotechnology group of the Tehran University GPA 4.00/4.00, **2014-2016**.

TEACHING EXPERIENCES

- Teaching Assistant Bio001 Contemporary Biology (2 semesters)
- Teaching Assistant Bio 002 Introduction to Molecular Biology (1 semester)
- Teaching Assistant BioE 002 Molecular Biology for Engineers (1 semester)
- Teaching Assistant Bio110 Cell Biology (1 semester)
- Teaching Assistant BioE 106 Cell Biology for Engineers (2 semesters)

MENTORING EXPERIENCES

- February 2024 – May 2024 Rayan McCoy, University of California, Merced, CA
- July 2023 – May 2024 Marlene Marquez Villanueva, University of California, Merced, CA
- February 2023 – May 2024 Orlando Hernandez, University of California, Merced, CA
- February 2023 – May 2024 Robert Dudkin, University of California, Merced, CA
- June 2022 – August 2022 Reagan Chan, University of California, Merced, CA
- February 2022 – Dec 2022 Ruth Verrinder, University of California, Merced, CA
- June 2021 – Dec 2022 Farhad Ghazali, University of California, Merced, CA

ORAL AND POSTER PRESENTATION

- Poster presentation at Annual Bioengineering Symposium, 2023, USA
- Poster presentation at AACR conference, 2023, USA
- Poster presentation at ASBMR conference, 2022, USA
- Poster presentation at Annual Bioengineering Symposium, 2022, USA

- Oral presentation at Annual Bioengineering Symposium, 2022, USA
- Poster presentation at ASBMR virtual conference, 2021, USA
- Poster presentation at virtual ISEH conference, 2021, USA
- Oral presentation at virtual ISEH conference, 2021, USA
- Oral presentation at Annual Bioengineering Symposium, 2021, USA
- Poster presentation at virtual IMMUNOLOGY2021™ AAI conference, 2021, USA
- Poster presentation at ASBMR virtual conference, 2020, USA
- Oral presentation at Medical High Technology International Congress (MHTIC), 2016, Iran

Cytotoxic Conditioning-Induced Changes in Bone Marrow Microenvironment:
A Study in Wild-Type and AML Mouse Models

by

Nastaran Abbasizadeh

Doctor of Philosophy in Quantitative and Systems Biology

University of California, Merced 2024

Professor Joel A. Spencer

Hematopoiesis relies on complex interactions between hematopoietic stem cells (HSCs) and the bone marrow (BM) microenvironment. However, alterations in this regulated system can result in malignant transformation and hematopoietic diseases. Acute myeloid leukemia (AML) is associated with an uncontrolled growth of leukemic blasts in the BM and has been considered as the most common acute leukemia in adults. AML survival after cytotoxic treatment remains a major therapeutic challenge mediating disease relapse and impacting the overall clinical outcome for patients. Fine-tuning the cytotoxic conditioning regimen to discover the most effective treatment plan has the potential to significantly improve outcomes in AML patients, thereby reducing the risk of relapse. The mechanism by which conditioning achieves therapeutic outcomes is through BM ablation. Additionally, conditioning can impact different compartments of the BM microenvironment. In this study, we investigated microenvironmental alterations to the BM after receiving low intensity (LI) and high intensity (HI) cytotoxic conditioning in the context of animal age. We later expanded our findings to investigate changes to BM niche around resistant tumor cells after cytotoxic conditioning in an AML model. Hematopoietic recovery appeared to be both age and dose dependent with more donor cells in HI compared to the LI group and more in young compared to the adult mice. Furthermore, vascular leakage outcomes revealed long-lasting disruption in the vascular integrity despite hematopoietic recovery overtime. *Ex vivo* imaging of the BM in the long bone indicated faster recovery of the blood vessels as a matter of morphology in young mice compared to the adult mice. In addition, our analysis demonstrated delayed response to the busulfan in the bone remodeling characterized by a shift towards bone resorption. BM and peripheral blood studies demonstrated promising results in slowing down the tumor proliferation in the AML mouse model after application of busulfan and cyclophosphamide (BU/CY) combination. Residual tumor cells exhibited a preference in their localization in endosteal niche where more vascular disruption was observed. Besides, cell size measurement demonstrated enhanced size of residual tumor cells in comparison to the primary AML cells. By examining the impact of chemotherapy dosage and recipient age on treatment response as well as BM microenvironment adjacent to the residual tumor cells after therapy,

we sought to optimize chemotherapy regimens and establish the groundwork for tailoring treatment strategies to AML cancer patients.

CHAPTER 1

Background and Introduction

1.1. Bone Marrow Microenvironment

The BM microenvironment, also known as the BM niche, is a complex and specialized environment playing a crucial role in the regulation and maintenance of HSCs[1]. HSCs are a group of stems cells that differentiate into various types of blood cells, including red blood cells (RBCs; erythrocytes), white blood cells (leukocytes), and platelets (thrombocytes)[2]. Based on the anatomical locations, BM microenvironment divides into two distinct niches: the central niche, located within the inner BM and the endosteal niche, found near the bone surface. As another classification, the BM niche is spatially organized by the vascular system, the bone structure, and a network of perivascular cells[3,4] (**Fig. 1.1**).

Structural and molecular differences in the BM vascular system separate them into three types of sinusoids, arterioles, and transiting zone vessels. Sinusoids and arterioles are primarily located within the central marrow cavity while transition zone vessels as a connecting network between arterioles and sinusoids is concentrated in the endosteal niche[5]. The endosteal niche as another BM microenvironment component can be found in the diaphysis, as the central part of a long bone, with dense cortical bone and metaphysis or epiphysis with the trabecular meshwork bone[3,6]. The endosteal niche consists of osteoblasts (OBs) as the primary cell type, osteocytes (OT_S), and osteoclasts (OCs) within this niche[7]. Unlike central BM which is highly enriched with HSCs (85%), endosteal niche harbors approximately 15% of the population. It is important to note that since central and endosteal BM are functionally different, they support different subsets of HSCs; the former promotes HSCs activation while the latter promotes the HSC quiescence[8–10]. Mesenchymal stem cells (MSCs) as another group of stem cells that differentiates into various cell types such as osteoblasts, chondrocytes, or adipocytes are essential for the maintenance and regulation of HSCs[11,12].

Besides anatomical components, the BM niche is regulated by a network of hematopoietic signaling pathways (e.g. TGF-β, HIF, Wnt, Notch), growth factors (e.g. SCF, LIF, IL-3, IL-6), cell cycle regulators (e.g. p18 and p21 inhibitors, p53) and transcription factors (e.g. GFI-1, RUNX1)[13]. Hypoxia as another key factor in the BM contributes to hematopoietic regulation and supports the function of HSCs[14]. In the BM, regardless of location and cell cycle phase of HSCs, they exhibit a hypoxic characteristics[15,16]. Hypoxia-inducible factors (HIFs) serve as the primary transcriptional regulators of the hypoxic responses in BM stem cells and activation of a wide variety of genes such as erythropoietin, Vascular endothelial growth factor (VEGF), and glucose transporters[17–19].

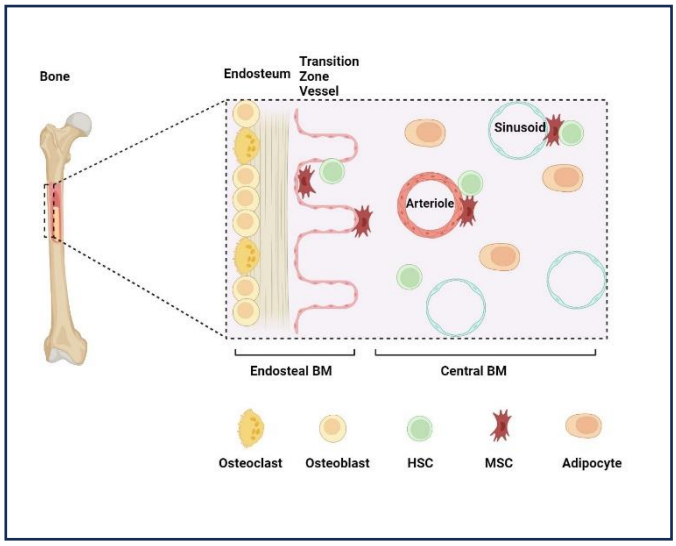

Figure 1.1. Main Features of Anatomically Defined Hematopoietic Stem Cells (HSCs) Niches in the BM Microenvironment. The BM vascular niche is categorized into three main types of sinusoids, arterioles, and transiting zone vessels. The endosteal niche comprises osteoblasts, osteocytes, and osteoclasts. Mesenchymal stem cells (MSCs), as another critical group of stem cells, play an essential role in the maintenance and regulation of HSCs within the BM microenvironment.

1.2. Hematopoiesis

Hematopoiesis is the process in the BM microenvironment by which HSCs differentiate into all the cellular components of the blood cells. This process is crucial to replenishing the blood cells that are damaged by normal cellular processes, diseases, or trauma. Depending on the hematopoiesis stage, HSCs and their progenitors show different extents of the self-renewal and differentiation capacity. Before developing into different types of mature blood cells, HSCs undergo hierarchical maturation steps to form a series of intermediate progenitors. According to **Fig. 1.2**, HSCs can be categorized into two subsets: the long-term subset (LT-HSC), characterized by its potential for indefinite self-renewal, and the short-term subset (ST-HSC), capable of self-renewal for a limited duration before their differentiation into multipotent progenitors (MPPs). MPPs, while lacking self-renewal capabilities, still possess the potential for lineage differentiation into common myeloid progenitors (CMP) or common lymphoid progenitors (CLP). CMPs will then generate granulocyte-macrophage progenitors (GMPs) and megakaryocyte-erythrocyte progenitors (MEPs). MEPs, in turn, can give rise to either erythrocytes or platelets. GMPs differentiate into granulocytes, including neutrophils, basophils, and eosinophils, or they can develop into macrophage or myeloid dendritic cells (DCs). CLP on the other hand can develop into immune cells including T cells, B cells, and natural killer (NK) cells[20–24].

Normal hematopoiesis relies on complex interactions between HSCs and the BM microenvironment leading to a balance in proliferation, differentiation, and overall homeostasis of the stem cell compartment. Different regions of the niche can promote the development of specific blood cell lineages. Studies have demonstrated the loss of lymphoid progenitors after conditionally deleting osteoblast cells in the endosteal

niche[25,26]. In addition, it has been reported that depletion of the CXCL12, as a chemoattractant, from osteolineage cells results in lymphoid progenitors depletion highlighting the importance of the endosteal niche in providing support for lymphopoiesis[27]. The regulatory role of ECs toward hematopoiesis has been evidenced by deletion of Jagged-1, as a type of Notch ligand, that result in decline of HSCs self-renewal[28]. MSCs as another key elements in the BM niche play an important role in hematopoiesis. Deletion of CXCL12 or SCF from all MSCs has been shown to affect the HSC population[29]. Taken together, the preservation of the HSC population and their functional properties requires BM niche homeostasis and alterations in this regulated system can result in malignant transformation, such as hematopoietic diseases.

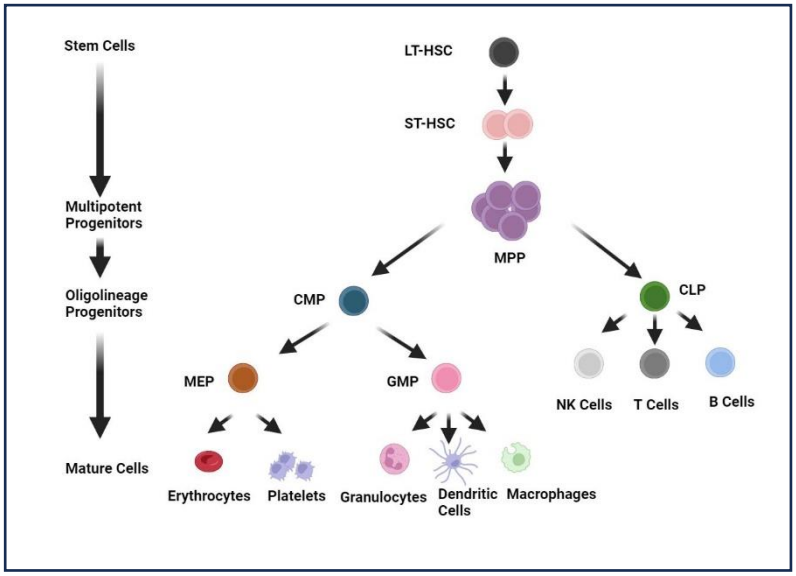

Figure 1.2. Hematopoietic Differentiation Model. HSCs can be classified into two main subsets of long-term subset (LT-HSC) and the short-term subset (ST-HSC) generating multipotent progenitors (MPP). MPPs further differentiate into common myeloid progenitors (CMPs) and common lymphoid progenitors (CLPs). CMPs commit to the myeloid lineage, generating granulocyte-macrophage progenitors (GMPs) and megakaryocyte-erythrocyte progenitors (MEPs). GMPs give rise to granulocytes, myeloid dendritic cells, and macrophages, while MEPs differentiate into platelets or erythrocytes. Conversely, CLPs commit to the lymphoid lineage, ultimately producing T cells, B cells, and natural killer (NK) cells. Arrows indicate the flow of differentiation from more primitive progenitors to more specialized cell types.

1.3. Leukemogenesis

Leukemia is characterized by uncontrolled expansion of white blood cells originating from the malignant transformation of a progenitor cell during hematopoiesis[30]. Depending on the originating cell lineage and some clinical criteria such as the speed of onset, the duration, and the persistence of the symptoms, leukemia classified into 4 groups: acute lymphoblastic leukemia, acute myeloid leukemia, chronic lymphoblastic leukemia, and chronic myeloid leukemia. Acute leukemia is characterized by rapidly progressive disease

followed by severe and short-term symptoms while chronic leukemias typically have a slow course of the disease with less severe but persistent symptoms. In addition, in acute leukemia, undifferentiated monoclonal cells are involved whereas chronic leukemia exhibit a clonal proliferation of pluripotent HSC. Acute myeloid leukemia (AML), and acute lymphoblastic leukemia (ALL) as the most frequent malignancies in adult and children, respectively are two main types of acute leukemia[31]. Chronic leukemias are subclassified into chronic myeloid leukemia (CML) and chronic lymphoblastic leukemia (CLL)[30].

Based on the leukemogenesis model in **Fig. 1.3**, the malignant transformation process which is common between various types of leukemia involves multiple steps, starting with an initial mutation in either normal HSCs or progenitor cells. Mutation in self-renewing HSCs leads to the generation of pre-leukemic stem cells (pre-LSCs) which develop to fully transformed leukemia stem cells following subsequent mutations. A progenitor cell can also undergo a transformation due to a mutation that keeps its ability to self-renew. This pre-leukemia progenitor cell can persist and, with additional mutations, eventually evolves into LSCs. In contrast, when a first mutation occurs in a progenitor without promoting self-renewal, the pre-malignant cell could be eliminated if subsequent mutations don't occur to develop them into an LSC[13].

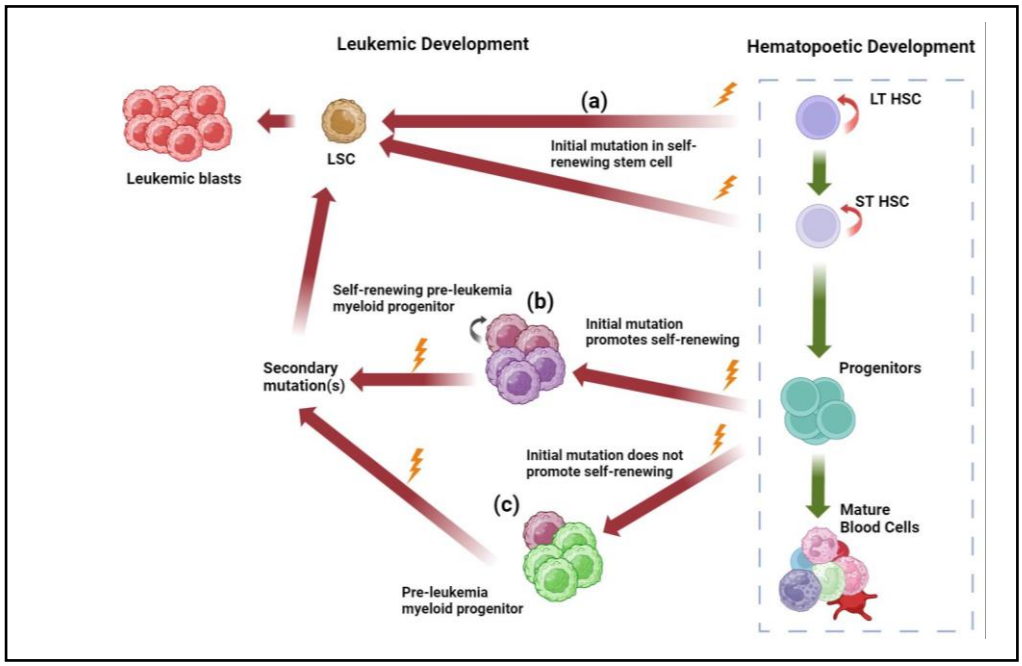

Figure 1.3. Leukemogenesis Model. The malignant transformation process in leukemia involves initial mutations occurring in either normal HSCs or progenitor cells, leading to the generation of pre-leukemic stem cells (LSCs). Subsequent mutations drive pre-leukemic progenitor cells into fully transformed LSCs. If the initial mutation occurs in a progenitor cell without promoting self-renewal, the pre-malignant cell may be eliminated unless subsequent mutations occur to develop them into LSCs. Green arrows indicate normal hematopoietic development and red arrows indicate leukemic development.

1.4. Leukemic Bone Marrow Niche

Even though the localization of LSCs within the BM niche requires further studies, it is evident that the microenvironment contributes to supporting LSCs in terms of their formation, engraftment, or chemotherapy resistance[32]. LSCs can reprogram MSCs to create a microenvironment in their favor. This reprogramming could be through transferring mitochondria to provide extra energy for tumor cells, protecting tumor cells from chemotherapy through an increase in Notch and Wnt signaling or inhibition of apoptosis[33,34]. Alteration in the BM vascular niche in leukemia with an increase in the VEGF promotes angiogenesis and continued blood supply for leukemia cells[35,36]. Studies also have shown that AML progression increases vascular permeability by inducing high nitric oxide (NO) production[37]. Increased vascular permeability contributes to the maintenance of hypoxic conditions in leukemia-affected areas. Osteolineage cells support leukemia cells survival and proliferation by activation of Notch signaling pathways that promote NF-kB. NF-kB is an inflammatory protein complex that plays a crucial role in LSCs maintenance[38]. Adipocyte cells in the BM can be activated by leukemia cells to lipolyze their triglyceride and generate free fatty acids. Tumor cells uptake fatty acids to continue their proliferation and survival[39]. The sympathetic nervous system (SNS) as another component of the BM niche contributes to leukemic progression. B2-adrenergic is sympathetic signaling pathway playing role in the BM niche regulation and hematopoiesis. Studies have shown that adrenergic blockade or sympathetic neuropathy leads to expansion of AML through a severely altered BM niche[40]. LSCs by releasing proinflammatory cytokines, such as Il-1 promote secretion of growth factors such as CXCL-12 or CSF by surrounding ECs and stromal cells. This results in unlimited cell growth and proliferation of leukemic cells[41]. Cytokines and adhesion receptors such as CXCR4, VLA-4, CD44, and E-selectin are also critical regulatory components for localization of LSCs in the BM. High expression of these molecules facilitate homing and retention of leukemic cells in the niche as well as their resistance to the chemotherapy[42](**Fig. 1.4**).

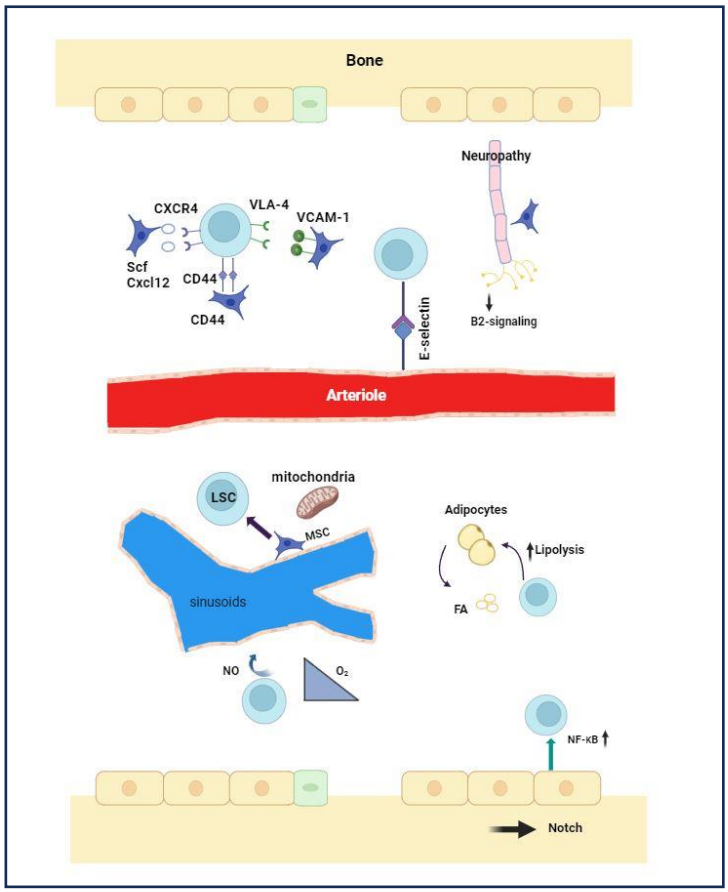

Figure 1.4. Remodeling of the Healthy Stem Cell Niche into a Leukemic Niche. The BM niche plays a pivotal role in supporting LSCs through various mechanisms, including reprogramming MSCs, or altering the vascular niche to promote angiogenesis. Additionally, interactions with osteolineage cells, adipocytes, and the SNS contribute to LSC survival and proliferation. Proinflammatory cytokines released by LSCs further enhance niche remodeling, facilitating unlimited cell growth and resistance to chemotherapy through regulatory molecules like CXCR4, CD44, and VLA-4.

1.5. Acute Myeloid Leukemia (AML)

AML is an aggressive BM related disorder that initiates with malignant transformation of myeloid lineage precursors. The disease is characterized by uncontrolled proliferation, abnormal self-renewal, and an inability to differentiate into fully functional mature myeloid blood cells[30,43]. In general, AML is classified into two groups: De novo AML (dn- AML) that occurs due to the accumulation of mutation during leukemogenesis without any preceding hematologic conditions and Secondary leukemia (s-AML) that can be subdivided into two categories of myelodysplasia-related changes (AML-MRC) and therapy-related AML (t-AML). AML-MRC is characterized by leukemia arising from a previous myelodysplastic syndrome (MDS) or myeloproliferative neoplasm (MPN),

whereas t-AML develops as a complication of prior cytotoxic conditioning therapy[44]. Studies have shown that there is a distinct mutational signature for dn-AML versus s-AML. **Fig. 1.5** Illustrates some representative mutational variations in dn-AML and s-AML[45]. The FLT3 receptor is commonly overexpressed on the majority of blasts in AML. Mutations such as FLT3 internal tandem duplications (FLT3-ITD) are linked with the high rate of relapse and poor overall survival outcomes in many AML patience[46].

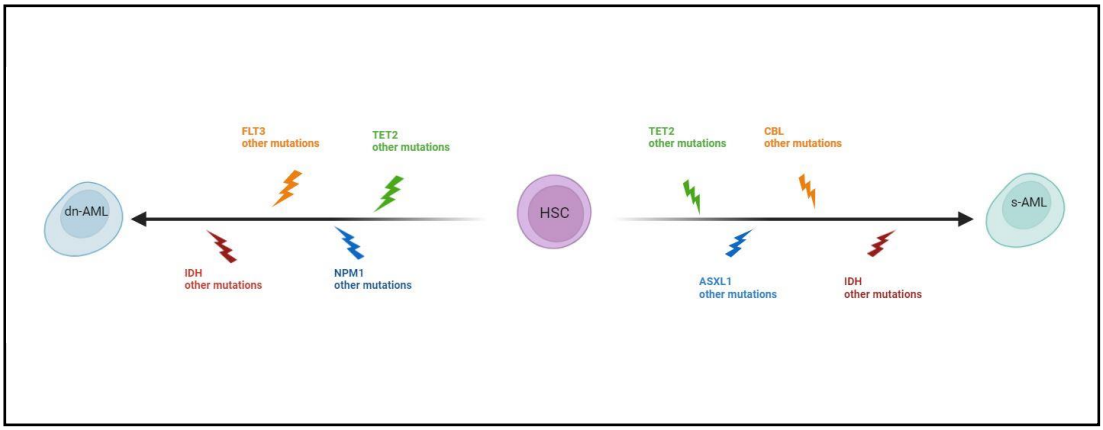

Figure 1.5. Mutational Variations in dn-AML and s-AML. A HSC undergoes a sequence of mutations, initially affecting genes highlighted in green. Subsequent mutations, illustrated in blue, orange, and red, result in the development of either secondary AML (sAML) or de novo AML (dn-AML) disease.

Regardless of its type, AML is the most common acute leukemia in adults and the second most frequent acute leukemia in children[47]. According to the 2022 clinical report from CIBMTR, AML has the highest rate of allogeneic hematopoietic stem cell transplantation (HCT) (about %50) in USA among other malignant and non-malignant diseases. Even though a majority of AML patients initially respond well to chemotherapy, long-term outcomes are still unfavorable due to the disease relapse causing low overall survival (OS) rate of 40-50% for individuals under the age of 60[48,49]. In older patients who are not able to tolerate intensive chemotherapy, survival rate remains low. In the U.S, in patients aged 70–74 and 75–79, five-year OS is as low as 7.4% and 3.3%, respectively[50]. Even though OS in patients who are receiving preparative regimens is low, in the absence of treatment, acute leukemias often result in BM failure and death within a few months. This necessitates an immediate and aggressive but tolerable therapeutic treatment for patients suffering from AML disease.

1.6. AML Cytotoxic Conditioning Strategies

HCT represents a potentially curative treatment option for various hematopoietic diseases, both malignant and non-malignant. In cases of malignant conditions, HCT involves the administration of preparative conditioning regimens to achieve two primary goals: to

provide effective host immunoablation that minimizes the graft rejection, and to lower the tumor burden[51]. In general, initial regimens are based on dose intensity leading to the development of two main categories of conditioning regimens: Myeloablative conditioning (MAC) and reduced intensity conditioning (RIC). Traditionally, MAC regimen was regarded as the standard intensity for patients requiring HCT. However, due to the inherent toxicity of this cytotoxic conditioning, it was considered suitable only for younger patients. Consequently, a less toxic and more tolerable preparative regime known as RIC and nonmyeloablative conditioning (NMA) were developed for older and less physically fit patients[52,53]. In general, what distinguishes RIC regimens from MAC is that they typically involve a reduction in the dose of alkylating agents or total body irradiation (TBI) by >30%[51].

Myeloablative Conditioning (MAC):

TBI-Based Regimens. Patients with hematologic malignancies who receive HCT often undergo high-dose TBI as a component of the conditioning regimen. The majority of these regimens combine fractionated TBI with doses ranging from 12 to 16 Gy, in combination with various chemotherapeutic agents, mainly cyclophosamide[54,55]. In general, while higher doses of TBI have the potential to decrease the risk of relapse, they have been associated with elevated, and sometimes life-threatening, occurrences such as gastrointestinal, hepatic, and pulmonary toxicities, as well as an increased risk of secondary malignancies[51].

High-Dose Chemotherapy-Based Regimens. In order to mitigate the short- and long-term toxicities linked to high-dose TBI and to target the tumors that are not accessible through external radiation, such as those deep within the body or scattered throughout multiple organs, systemic chemotherapy has emerged as a preferred alternative. Chemotherapy-based regimens primarily rely on alkylating agents due to their favorable toxicity profile, and their effectiveness against non-dividing tumor cells[51]. Busulfan is an alkylating agent with myeloablative properties that functions by inhibiting DNA replication through DNA crosslinking[56]. Busulfan exhibits particular sensitivity towards cells in the G0 resting phase of the cell cycle[57]. This drug is employed as a preparative agent before HCT due to its cytotoxic effects on the recipient's HSCs. In addition, it demonstrates efficacy in a range of malignancies such as CML, AML, ALL, lymphomas, and multiple myeloma[51]. However, busulfan cannot be used as a sole conditioning agent for HCT due to some associated limitations such as low toxicity towards mature lymphocytes and its variation in plasma levels when it is administered orally in patients. Therefore, regimens comprising high dose busulfan and other chemotherapy agents mainly cyclophosphamide and fludarabine were established and became a common choice for patients in need of HCT[54,58]. Cyclophosphamide is another alkylating agent, chemically related to nitrogen mustard, promotes cell death by binding to DNA and inhibiting DNA replication[59]. While high doses of cyclophosphamide have direct tumoricidal effects and induce immunosuppression, low dose of this compound has been found to promote the immune

stimulation by decreasing the number of T regulatory cells (T_{reg} cells)[60]. To reduce the occurrence of regimen-related toxicity and transplant-related mortality (TRM), fludarabine, an effective immunosuppressive purine analog, could be used instead of cyclophosphamide in both myeloablative and non-myeloablative conditioning regimens[61,62].

Reduced Intensity Conditioning (RIC)/ Nonmyeloablative Conditioning (NMA):

RIC was developed when some clinical observations revealed that patients who experience graft-versus-host disease (GVHD) following allogeneic HCT benefit from improved relapse-free survival. This recognition highlighted that HCT not only can rescue patients from the hematologic toxicity of high-dose conditioning, but also can contribute to the cure of malignant diseases through immunologic graft-versus-tumor (GVT) effects[63]. These findings prompted the development of RIC and NMA regimens, making allogeneic HCT a treatment option for older and medically weak patients who previously had not received high-dose conditioning. RIC primarily relies on the GVT effect more than cytotoxic effect for its effectiveness[64]. Studies that have compared MAC and RIC in patients with AML or MDS have indicated that RIC is linked to a higher risk of relapse but a reduced rate of TRM. As a result, this leads to comparable OS, even though patients are typically older and less physically fit on average[65,66]. Therefore, considering the patient's condition, an effective treatment involves a protocol that results in the least toxicity and most optimal therapeutic results.

Regardless of the regimen’s intensity, there are two treatment phases for AML: Remission induction therapy and post remission therapy. During the remission induction therapy, a combination of cytotoxic regimens is applied to eliminate leukemia cells from the blood and BM. Due to the high rate of relapse in AML, post remission therapy, as the second phase of treatment, is essential to target the resistant leukemia cells causing MRD. MRD refers to the persistence of leukemic cells post-treatment at levels below morphologic detection. In clinical trials, MRD serves as a crucial biomarker in AML for prognostic, monitoring, and efficacy-response to the therapy plan[67,68]. The 7+3 treatment plan is a common intensive induction chemotherapy regimen used for AML since the first time that was proposed in 1973[69]. In 7+3 protocol, "7" refers to a continuous infusion of cytarabine (Ara-C) for seven days, and the "3" refers to a three-day injection of an anthracycline drug usually daunorubicin or idarubicin. However, over the past few years, progressive understanding of the AML has been leading to the protocol modification and introducing several novel agents such as Venetoclax or FLT3 inhibitors, that result in a better response in patients[70,71].

1.7. Impact of Cytotoxic Conditioning on the BM Niche

Conditioning of the BM before HCT is crucial for primarily two purposes: eliminating the tumor cells and promoting the successful engraftment of donor cells. While standard conditioning regimens, usually involving chemotherapy and/or radiotherapy, have demonstrated efficacy in depleting the BM, they are also linked to significant stress induction to the BM niche and a high incidence of treatment-related mortality. Given that both host and donor HSCs require support of the BM microenvironment to regulate their function, alteration to the stem cell niche could impact the clinical outcomes after therapy in cancer patients[72].

BM Niche Cells and their Alterations after Cytotoxic Conditioning

Endothelial Cells (ECs). ECs are a group of cells lining the inner layer of the blood vessels and promoting smooth blood flow or facilitating exchange of nutrients and waste products. Depending on their specific location and differential gene expression, ECs can be categorized as arteriolar endothelial cells (AECs) or sinusoid endothelial cells (SECs)[73]. ECs play an important role in regulating HSCs in the normal niche and hematopoietic recovery after HCT. Studies have shown that in mice, irradiation or chemotherapy induce alteration to vascular system such as damage to the SECs and therefore plasma leakage, disruption of columnar capillaries in the metaphysis, and dilation of sinusoidal capillaries in the diaphysis[74–76]. Reciprocal relation between ECs and HSCs promotes recovery of ECs after HCT overtime and efficient engraftment of transplanted Hematopoietic stem and progenitor cells (HSPCs) following SECs recovery. ECs contribute to the transplanted HSC engraftment by activation of signaling factors such as VEGFR2, Tie2, Jagged-1, and Jagged-2[28,74,75,77]

Mesenchymal Stromal Cells (MSCs). MSCs as another key component of the BM regulate homeostasis, mainly HSC maintenance, by secreting crucial factors such as CXCL12, angiopoietin, and SCF. In the majority of cytotoxic conditioning studies, MSCs have been found resistant to the stress suggesting that this cell type is not entirely eradicated by myeloablative conditioning[78]. While MSCs may endure to some extent conditioning, they do accumulate damage. In this regard, *in vitro* irradiation of human MSCs has been shown to accumulate DNA double-strand breaks, change their gene expression, or skew their differentiation towards mainly adipocytes[79,80].

Osteolineage Cells. Osteolineage cells are a group of bone-forming cells that release various crucial factors for the HSCs maintenance including CXCL12, SCF, angiopoietin, and osteopontin (OPN)[73,81]. Even though the number of osteoblasts has been reported to be closely correlated with the number of HSCs, more recently, there is an ongoing debate about the extent of osteolineage cells role in the regulation of HSCs[29,82] . This could be due to the fact that minority of HSCs are in direct contact with BM osteoblasts and most of them are localized in proximate to BM blood vessels[83]. In general, osteolineage cells have demonstrated the regulation of more committed hematopoietic progenitor cells in mice[27,73]. Damage induced by osteolineage cells due to conditioning results in bone-related

complications including bone loss, osteopenia, osteoporosis, and avascular necrosis of bone[84]. *In vitro* chemotherapeutic treatment of both murine and human osteoblasts has been shown to result in reduced production of CXCL12 and a diminished capacity to support immature B progenitor cells[85,86]. Similarly, irradiation induces various functional defects in osteoblasts, such as reduced production of extracellular matrix components or impaired proliferation[87].

Nerve Fibers. BM nerves play a crucial role in regulating the proliferation, differentiation, and HSPCs migration between BM and extramedullary sites[72]. The interaction between the SNS and HSCs is partially mediated through niche cells such as stromal cells[88]. Neurotoxic chemotherapy and irradiation conditionings lead to transient or persistent sympathetic neuropathy and therefore hematopoietic dysfunction[89]. In humans, many cancer survivors experience radiation-induced neuropathy[90].

Understanding the cytotoxic therapy effect on BM niche is crucial since conditioning regimens have revealed contributions to the survival and chemoresistance of tumor cells leading to leukemia relapse. As mentioned before, t-AML is a late complication of cytotoxic therapy leading to secondary AML disease in patients who have received chemotherapy or irradiation.

To optimize therapeutic outcomes while minimizing the risk of adverse effects following conditioning regimens, considering a patient-centered approach is essential in designing cancer treatment plans. Individualized treatment plans are particularly crucial in age-related cancers, such as AML. As previously discussed, AML is more prevalent in individuals older than 65 who are often less fit for standard MAC regimens, necessitating adjustments to the conditioning intensity based on their tolerance.

In this regard in my project, the primary goal is to investigate the impact of recipient age and chemotherapy dosage intensity on changes within the BM following conditioning (Chapter 2). Subsequently, we aim to create an AML mouse model to explore how or whether alterations in the BM niche following cytotoxic therapy or AML progression contribute to AML relapse after treatment (Chapter 3).

CHAPTER 2

Age and Dose Dependent Changes to the Bone and Bone Marrow Microenvironment after Cytotoxic Conditioning with Busulfan.

Brief Summary

In this chapter, employing 2-photon (2P) intravital microscopy, I explored the changes occurring within the bone and BM microenvironment following cytotoxic conditioning, focusing on hematopoietic recovery. Specifically, I investigated the impact of chemotherapy dosage (high intensity and low intensity) and recipient animal age (young and adult) on these dynamics.

Key Findings:

- **Hematopoietic Recovery:** The recovery of hematopoiesis was found to be dependent on both dosage and recipient age. Young mice exhibited a higher accumulation of donor cells compared to adult mice, and HI chemotherapy resulted in greater donor cell engraftment compared to LI chemotherapy.
- **Vascular Functionality:** Despite hematopoietic recovery, alterations in the integrity of calvaria BM blood vessels persisted in both young and adult mice even at day 42 post HCT. This suggests a sustained impact of cytotoxic conditioning on the vascular microenvironment.
- **Vascular Morphology:** Assessment of vascular remodeling parameters, including blood vessel diameter, frequency, and density, revealed a partial recovery in young mice by day 42 post-HCT. However, these changes remained abnormal in older mice, indicating an age-dependent impairment in vascular recovery following cytotoxic treatment.
- **Bone Remodeling:** Both young and adult mice exhibited significant bone remodeling by day 42 post-HCT, compared to earlier time points. Additionally, young mice demonstrated a faster bone turnover response compared to adult mice, indicating age-related differences in bone recovery dynamics.

Age and Dose Dependent Changes to the Bone and Bone Marrow Microenvironment after Cytotoxic Conditioning with Busulfan

Nastaran Abbasizadeh[1,2,3], Christian S. Burns[1,2,3], Ruth Verrinder[1,2], Farhad Ghazali[1], Negar Seyedhassantehrani[1,2,3], Joel A. Spencer[1,2,3,4]*

[1]*Department of Bioengineering, School of Engineering,* [2]*Center for Cellular and Biomolecular Machines,* [3]Quantitative and Systems Biology Graduate Program, [4]*Health Sciences Research Institute, University of California, Merced, Merced, CA, United States.*

*Correspondence: joel.spencer@ucmerced.edu

ABSTRACT

Preparative regimens before HCT damage the BM microenvironment, potentially leading to secondary morbidity and even mortality. The precise effects of cytotoxic preconditioning on bone and BM remodeling, regeneration, and subsequent hematopoietic recovery over time remain unclear. Moreover, the influence of recipient age and cytotoxic dose have not been fully described. In this study, we longitudinally investigated bone and BM remodeling after busulfan treatment with low intensity (LI) and high intensity (HI) regimens as a function of animal age. As expected, higher donor chimerism was observed in young mice in both LI and HI regimens compared to adult mice. Noticeably in adult mice, significant engraftment was only observed in the HI group. The integrity of the blood-BM barrier in calvaria BM blood vessels was lost after busulfan treatment in the young mice and remained altered even 6 weeks after HCT. In adult mice, the severity of vascular leakage appeared to be dose-dependent, being more pronounced in HI compared to LI recipients. Interestingly, no noticeable change in blood flow velocity was observed following busulfan treatment. *Ex vivo* imaging of the long bones revealed a reduction in the frequency and an increase in the diameter and density of the blood vessels shortly after treatment, a phenomenon that largely recovered in young mice but persisted in older mice after 6 weeks. Furthermore, analysis of bone remodeling indicated a significant alteration in bone turnover at 6 weeks compared to earlier timepoints in both young and adult mice. Overall, our results reveal new aspects of bone and BM remodeling, as well as hematopoietic recovery, that is dependent on the cytotoxic dose and recipient age.

INTRODUCTION

HCT is a common therapeutic approach for hematologic malignancies such as leukemia, multiple myeloma, lymphoma and non-malignant diseases[91–95]. Successful donor cell engraftment after HCT necessitates cytotoxic preconditioning[93,96]. Historically, MAC has been considered a standard preconditioning regimen for patients in need of HCT[97]. The inherent toxicity and non-relapse mortality associated with MAC, however, limits its use to a select group of patients[97,98]. To address these limitations, a more tolerable preparative regimen, known as RIC, was developed for less fit patients[97,99,100]. Clinical studies indicate that RIC has a lower cumulative incidence of chronic GVHD but similar OS compared to MAC, positioning it as a potential alternative treatment[94]. Insufficient conditioning, however, can lead to early disease relapse after transplantation due to the lack of graft vs. malignancy effect from mixed chimerism[101,102]. Therefore, it is important to fine tune the intensity of RIC to provide the most effective clinical outcomes after HCT.

Cytotoxic preconditioning is known to disrupt the hematopoietic and non-hematopoietic compartments of the bone and BM microenvironments regardless of the preparative regimen used[76,103–105]. After treatment, BM vasculature can undergo significant changes such as the dilation and fusion of sinusoidal vessels and a temporary decrease in vessel frequency[106–108]. Disruption in both osteoblast and osteoclast activities result in increased rates of bone resorption[103,109]. Furthermore, MSCs after exposure to low irradiation have been found to exhibit a shift in their differentiation capacity towards less adipocytes and more osteogenic cells[79].

In addition to conditioning regimens, the aging process is also known to disrupt the functionality of the BM niche. Age-related changes such as a notable decrease in osteoprogenitors, a decline in the number of the metaphyseal blood vessels, and alterations in the differentiation and proliferation of mesenchymal stromal cells, negatively impact hematopoiesis[110–114]. Furthermore, elevated levels of intracellular reactive oxygen species (ROS), accumulation of the DNA damage, upregulation of pro-inflammatory cytokines such as IL-6, NF-κB, C-reactive protein or dysregulated DNA methylation patterns at the genes contributing to the lymphoid and myeloid balancing are the other alterations that HSCs experience during aging[115–120]. Consequently, the host response to the preparative regimen is contingent on both the intensity of cytotoxic treatment and age of the recipient.

In this study, we used two doses of 1,4-Butanediol dimethanesulfonate (busulfan) called Low Intensity (LI) and High Intensity (HI) to condition the BM niche in both young and adult mice before HCT. Busulfan, a DNA alkylating drug, is commonly used in combination with cyclophosphamide to treat leukemia[121–123]. Various doses of busulfan have been previously used in myeloablative or non-myeloablative preconditioning[124–126]. Our research reveals significant alterations to the BM microenvironment after busulfan treatment that are dependent on both age and dose.

MATERIAL AND METHOD

Animals

Male C57BL/6J, C57BL/6 CD45.1 (B6.SJL-Ptprca Pepcb/BoyJ) and C57BL/6-Tg(UBC-GFP)30Scha/J (UBC-GFP) transgenic mice were purchased from Jackson laboratory. Mice were bred and housed in the DARS at UC Merced. The animal study received approval from the Institutional Animal Care and Use Committee (IACUC) at the University of California, Merced.

Busulfan Treatment and Whole BM Cell Transplantation

We used 4-6 week (young) and 16-20 week (adult) old male C57BL/6 CD45.1 and C57BL/6J mice as recipients. To investigate the effect of variable RIC dosage, mice received either 40 mg/kg (LI) or 80 mg/kg (HI) dose of busulfan (Cayman Chemicals Company; 14843) via intraperitoneal injection (IP). Busulfan solution was prepared immediately before injection as previously described[127]. Briefly, busulfan crystals were dissolved in Dimethyl sulfoxide (DMSO) (Sigma Aldrich; 472301) and Ca+/Mg+ free Phosphate buffer solution (PBS) (gibco; 2003901) was added to the solution to make a final drug concentration of 1mg/ml in 10% DMSO. The working solution was filtered through a 0.22 µm syringe filter (Fisherbrand; R7PA99681) and was administered to mice in separate doses of 20 mg/kg per day on two (LI) and four (HI) consecutive days.

One day following busulfan conditioning, 8-12 week UBC-GFP transgenic donor mice were euthanized by CO_2 inhalation and cervical dislocation. Long bones were collected, cleaned, and crushed in Fluorescence-Activated Cell Sorting (FACS) buffer. The cell mixture was filtered through a 40 µm filter into a 50 ml falcon tube and spun at 1500 rpm for 5 minutes at 4°C. The supernatant was aspirated, and the pellet was resuspended in Ammonium-Chloride-Potassium (ACK) lysis buffer to remove erythrocytes. The reaction was stopped after 1 minute incubation by adding FACS buffer and cells were washed by centrifuging at 2000 rpm for 3 minutes at 4°C. Cells were resuspended in PBS and a cell count was performed using a hemocytometer and Trypan Blue (gibco, 15250-061) staining. Finally, a suspension of 1×10^6 cells/ml was administered by retroorbital injection.

Sample Collection: BM and Peripheral Blood (PB)

To collect PB, mice were kept under a heat lamp for a few minutes to increase blood circulation. The mice were transferred to a restrainer and a small incision was made over the ventral tail vein using a scalpel blade. Blood was collected (no more than 10 drops) and stored in blood collection tubes spray coated with Dipotassium ethylenediaminetetraacetic acid (K2EDTA) (BD Microtainer; 365974). Heparinized blood was added to 9 ml diH_2O for RBC lysis and immediately after resuspension, 1 ml 10x PBS was added to the solution to prevent white blood cells lysis. Cells were spun at 2000 rpm for 5 minutes at 4°C. The supernatant was removed, and the pellet was resuspended in 9 ml diH_2O and 1 ml 10x PBS to remove the remaining RBC. Cells were spun at 2000 rpm for 3 minutes at 4°C and 100 µl of the sample was aliquoted into 96 V-bottom wells for FACS staining. Cells were washed with 100 µl of FACS buffer and centrifuged at 2000 rpm for 3 minutes at 4°C. The supernatant was removed and cells were stained with 50 µl of staining cocktail containing

APC/Cy7 CD45.2 (1:100, Biolegend;109824) and PerCP/Cy5 CD45.1 (1:100, Biolegend;110728) in the dark on ice. After 15 minutes incubation, cells were washed with FACS buffer, spun, and resuspended in 200 µl FACS buffer for flow cytometry chimerism.

To collect the BM, mice were euthanized on day 42 post-transplantation and the same procedure as the whole BM transplantation described previously was performed to collect cells. Cells were then resuspended in PBS and a suspension of 1×10^6 cells/ml was collected for staining. After 15 minutes incubation with APC/Cy7 CD45.2 (1:100) and PerCP/Cy5 CD45.1 (1:100) cells were washed with FACS buffer, spun and resuspended in 200 µl FACS for flow cytometry chimerism[128].

Two Photon *In Vivo* and *Ex Vivo* Imaging

In vivo calvaria and *ex vivo* femur imaging was performed with a custom-built two-photon intravital microscope (BLIQ Photonics). A 25x fluid immersion objective (Olympus; XLPLN25XWMP2, NA = 1.05) was used for all images, with an approximate field of view (FOV) of 317 µm by 159 µm. During live imaging, two tunable femtosecond lasers, MaiTai (Spectra Physics; MaiTai eHP DS) and Insight (Spectra Physics; Insight X3), were tuned to 800 nm and 950 nm to observe 70 kDa Rhodamine-B Dextran (ThermoFisher, D1841) and Green fluorescent protein (GFP) cells signals, respectively. For *ex vivo* imaging, the MaiTai and Insight lasers were initially tuned to 950/1220 nm to excite GFP, Alexafluor 647 conjugated vascular antibodies, and Second Harmonic Generation (SHG), respectively. The long bones were imaged a second time at 800 nm to excite Calcein and Alizarin. Videos were recorded at 30 frames per second and images were generated by averaging 30 frames.

For *in vivo* visualization of the calvaria BM, anesthesia was induced via initial inhalation of 3-4% isoflurane with 100% O_2 at 1 L/min that was reduced to 1.5% as maintenance. The skull was secured in a custom head mount that was equipped with a heating pad to maintain the animal body temperature during the procedure. After shaving top of the head, a small incision was made along the sagittal and lambda suture of the skull to expose the calvarium as described before[129].

For *ex vivo* imaging of the long bone, mice were injected retro-orbitally with Alexafluor 647 conjugated vascular antibodies (CD31; 102516, Biolegend, Sca-1; 108118, Biolegend, VE-Cadherin; 138006, Biolegend) 30 minutes before intracardiac perfusion. To study bone remodeling, Calcein (30 mg/kg, Sigma; SLCF7304) and Alizarin (20mg/kg, Sigma; SHBL6801) were administered 48 hour and 30 minutes before imaging to track bone turnover based on the ratio of dye 1 (Calcein; marks the old bone front) to dye 2 (Alizarin; marks the new bone front). Mice were perfused with 1x PBS to wash out the blood followed by 4% paraformaldehyde (PFA, Fischer Chemical; 1638384) to internally fix the tissue. Subsequently, femurs were harvested and fixed in 4% PFA for 30 minutes, at 4°C. The bones were then washed with 1X PBS, immersed in 30% sucrose (Sigma; SLCC8492) for 1 hour, frozen in optimal cutting temperature (OCT, Fisher Scientific; 4585) compound and kept at – 80°C. Samples were shaved using a cryostat (LEICA CM1860) equipped with a high-profile blade (Leica; 3802121) to expose the BM region.

Image Quantification

We used Fiji (ImageJ 1.53t) for image processing including quantification of vessel permeability, leakage, morphological changes to the blood vessel, evaluating bone turnover rate, and quantifying GFP+ donor cells engraftment in the recipient BM. Custom scripts in MATLAB (2020a) were used to calculate BM blood flow velocity[130] . In order to study changes to the vascular system in the calvaria BM, 70 kDa Rhodamine-B Dextran was injected retro-orbitally during *in vivo* imaging. The blood vessel permeability was measured during the first 30 seconds post dye injection and was quantified based on the change in fluorescence intensity outside of blood vessels as a function of time as described before[128,131,132]. Vascular leakage was measured through z stack images (2 μm z step) taken 10 minutes after dye administration as described before and was calculated based on the ratio between the fluorescent intensity in the perivascular space to the fluorescent intensity in the adjacent vascular lumen[128]. Note that vessel permeability reflects the rate at which small molecules exit blood vessels and fill the surrounding perivascular space, whereas leakage is the ratio of fluorescent dye in the perivascular space and vascular lumen after reaching equilibrium. Blood flow velocity was calculated by recording 30 second videos of blood flow in the BM calvaria and then utilizing Line Scanning Particle Image Velocimetry (LSPIV) implemented in a custom MATLAB script to calculate blood flow velocity as previously described[130,133].

To measure vascular density, blood vessel images were color thresholder in Fiji (ImageJ 1.53t). The resulting binary image was despeckled, the binary fill hole function was applied, and a Python (3.7.6) script was used to calculate the ratio of the total blood vessel volume to total BM volume. We defined vessel density as the total space of the BM occupied by blood vessels. To study bone remodeling, the double-staining approach was performed by using Calcein (dye1) and Alizarin (dye2). The ratio of dye1 / dye2 was calculated by measuring the total Calcein pixel area to the total Alizarin pixel area in each FOV. Based on the dye ratio, fractions of the cavity type (D-type; > 0.75, M-type; 0.25-0.75, R-type; < 0.25) were quantified as described previously[15]. Max intensity projections (MIP) of the long bone were taken and the number of GFP+ cells in the BM on day 2 post-transplantation was manually counted. Representative samples of BM leakage and long bone images were generated by taking MIP of BM regions and contrast/enhancement adjustment was applied for display purposes.

Statistical Analysis

In our study, at least n = 3 mice per group was used for imaging and flow cytometry chimerism analysis using G*Power. Graphs and statistical analyses were generated using GraphPad Prism 9.0. ordinary one-way ANOVA to test differences between study groups. A normality test was performed to assess the normal distribution of the data. A p-value less than 0.05 was considered to be statistically significant (*$p < 0.05$, **$p < 0.01$, ***$p < 0.001$; ****$p < 0.0001$).

RESULTS

Dose and Age Dependent Hematopoietic Recovery Following Busulfan Conditioning and HCT. To longitudinally investigate changes to the BM microenvironment as a function of animal age and chemotherapy dose, we created a HCT model incorporating busulfan preconditioning with low and high intensity in young (4-6 weeks old) and adult (16-20 weeks old) mice (**Fig. 2.1a**). After preconditioning, we transplanted whole BM cells from GFP+ donor mice (Ubiquitin-GFP mice) and evaluated bone and BM microenvironment as well as hematopoietic recovery on days 2, 5, and 42 post-transplantations (**Fig. 2.1b**). Consistent with previous literature, BM images on day 42 post-transplantation revealed a higher accumulation of GFP+ donor cells in busulfan conditioned young mice, particularly in the HI group, compared to controls (**Fig. 2.1c, d**)[134,135]. In the adult group, only mice that received HI conditioning revealed effective hematopoietic engraftment 42 days after transplantation (**Fig. 2.1e, f**). Comparison of flow cytometry donor chimerism on day 42 in BM and PB was consistent with the BM imaging (**Fig. 2.1g, h**). In addition to dosage, hematopoietic recovery was dependent on the recipient's age, particularly in HI mice (**Fig. 2.1g, h**). Early homing of hematopoietic donor cells was evaluated by manual counting of GFP+ cells in both the long bones and calvaria on day 2 post-transplantation. No statistically significant difference was observed between young and adult mice suggesting that hematopoietic engraftment is more age dependent than early homing (**Fig. 2.1i, j**).

A)

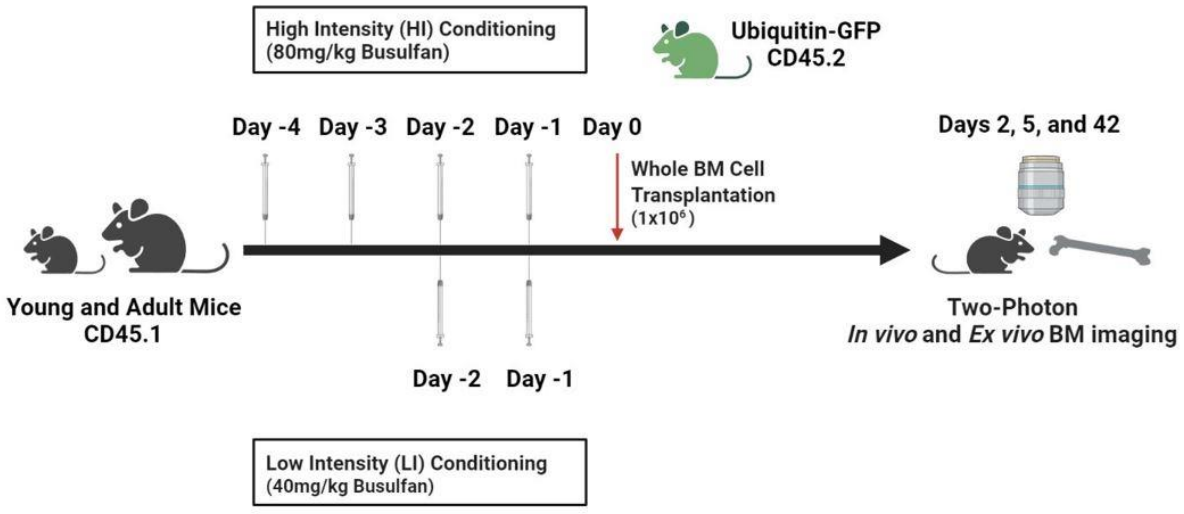

B)

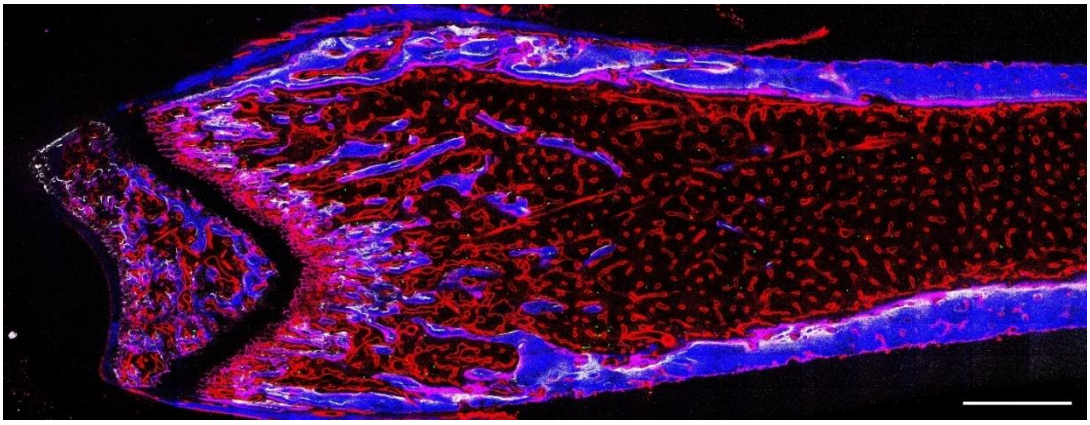

C)

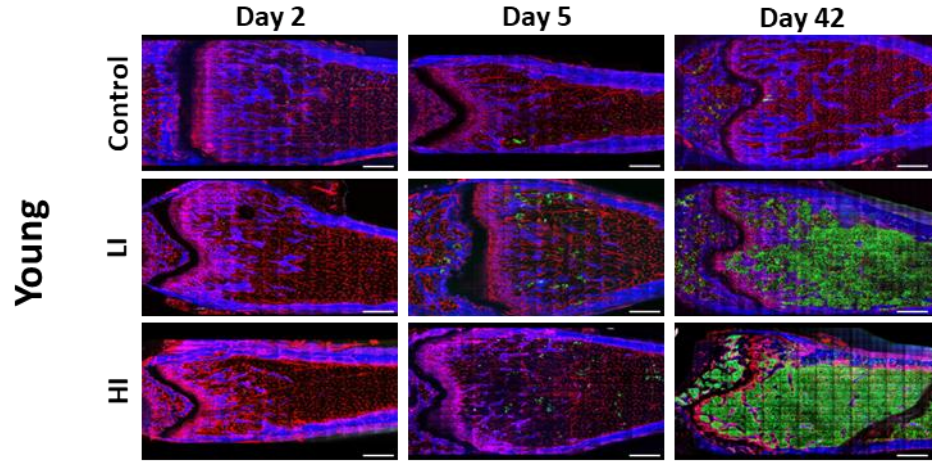
Day 2
Day 5
Day 42
Control
LI
HI
Young

D)

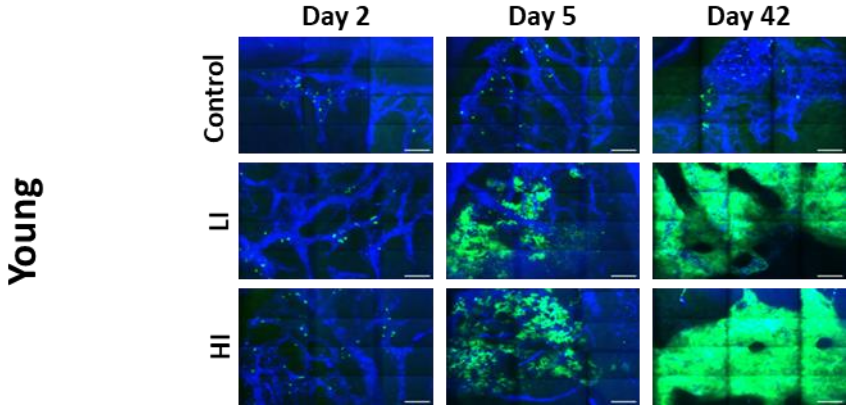
Day 2
Day 5
Day 42
Control
LI
HI
Young

E)

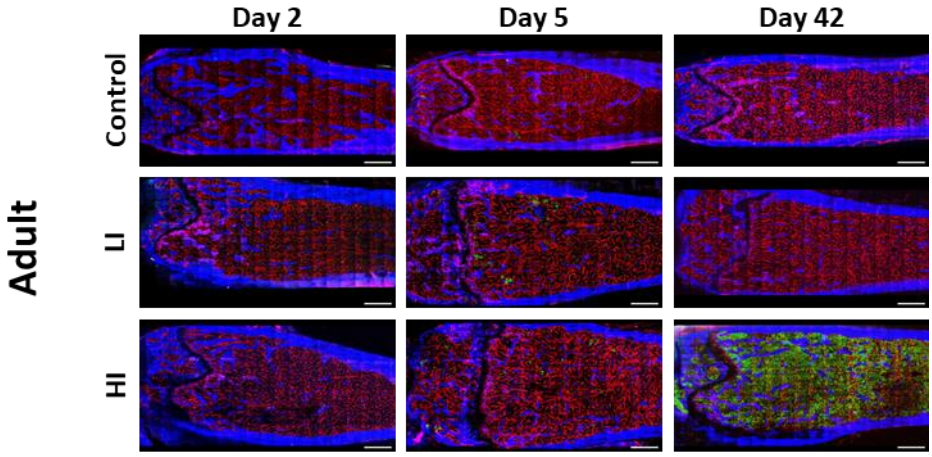
Day 2
Day 5
Day 42
Adult
Control
LI
HI

F)

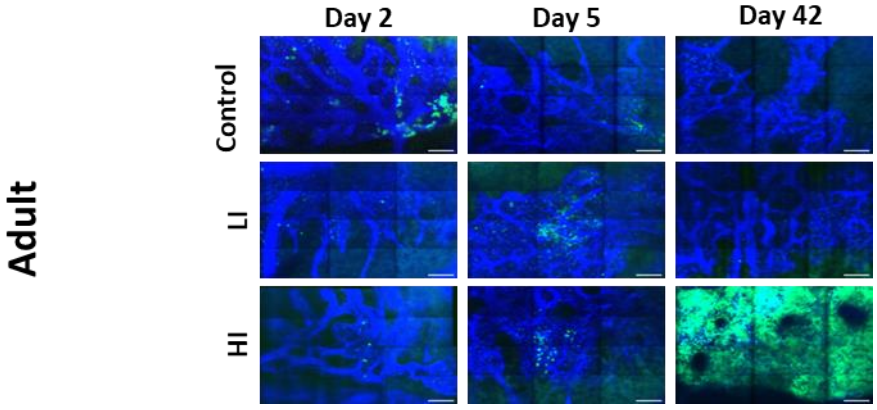
Day 2
Day 5
Day 42
Adult
Control
LI
HI

G)

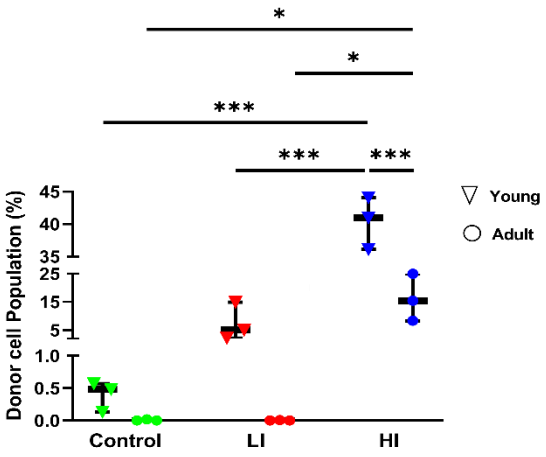
*
*
***
***
***
Donor cell Population (%)
45
40
35
25
15
5
1.0
0.5
0.0
Control
LI
HI
Young
Adult

H)

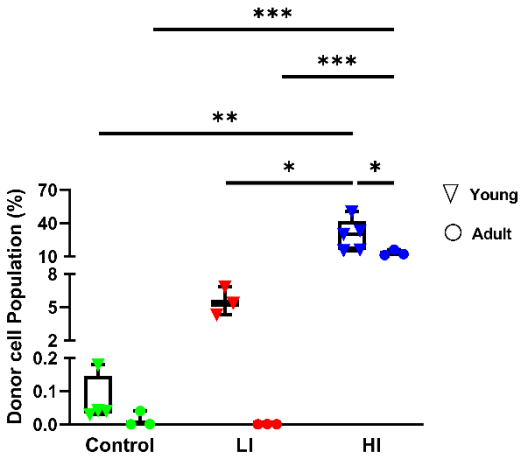
***
***
**
*
*
Donor cell Population (%)
70
40
10
8
5
2
0.2
0.1
0.0
Control
LI
HI
Young
Adult

I) J)

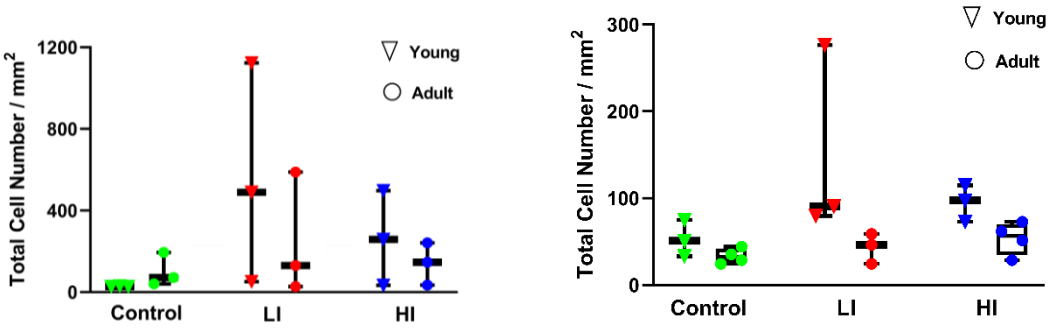

Figure 2.1. LI and HI Regimens Induce Dose-Dependent Hematopoietic Recovery in Young and Adult Mice. A) Schematic of the experiment. Low and high doses of busulfan were administered to young (4-6 weeks) and adult (16-20 weeks) mice on two (LI) and four (HI) consecutive days. Whole BM cells from UBC-GFP transgenic mice were injected into recipients 1 day after busulfan conditioning. Imaging was performed on days 2, 5, and 42 post-transplantation; **B)** Representative long bone image after transplantation; Red: blood vessel, Blue: Bone (SHG), Green: GFP+ cells, Purple (Alizarin), White (Calcein); **C, D)** Representative longitudinal images of the HSC recovery in long bone **(C)** and calvarium **(D)** of control and LI/HI conditioned young mice; **E, F)** Representative longitudinal images of the HSC recovery in long bone **(E)** and calvarium **(F)** of control and LI/HI conditioned adult mice; **G, H)** Quantification of donor (GFP+) cells in control, and LI/HI conditioned mice 42 days post-transplantation in BM **(G)** and PB **(H)**; **I, J)** Donor cell homing 2 days post-transplantation in the long bone **(I)** and calvaria **(J)** BM of young and adult mice. long bones scale bar: 500 µm; calvarium scale bar: 100 µm. *$p < 0.05$, **$p < 0.01$,***$p < 0.001$; ****$p < 0.0001$.

Dose and Age Dependent Alteration in the Vascular Morphology and Functionality Following Busulfan Conditioning and HCT. To evaluate the morphology of the BM vascular system after busulfan conditioning and HCT, we quantified the blood vessels diameter, frequency, and density. In young mice at early timepoints (days 2 and 5) after treatment, blood vessel diameter was markedly increased while the vessel frequency was decreased compared to the controls ($p < 0.0001$), but they largely rescued by 42 after transplantation (**Fig. 2.2a-c**). Furthermore, at early days post-treatment, the vessel density was substantially enhanced in LI ($p < 0.0001$ on days 2 and 5) and HI ($p < 0.0001$ on day 2 and $p < 0.01$ on day 5) but was comparable to controls by day 42 (**Fig. 2.2a, d**). Unlike young mice, vascular diameter (LI; $p < 0.0001$ and HI; $p < 0.001$; **Fig. 2.2e, f**) and frequency ($p < 0.001$; **Fig. 2.2e, g**) remained abnormal after 42 days in busulfan treated adult mice, suggesting an age-dependent delay in BM regeneration. Additionally, vessel density remained consistent across all study groups at all timepoints (**Fig. 2.2e, h**) due to a compensatory effect involving increased vascular diameter and reduced frequency.

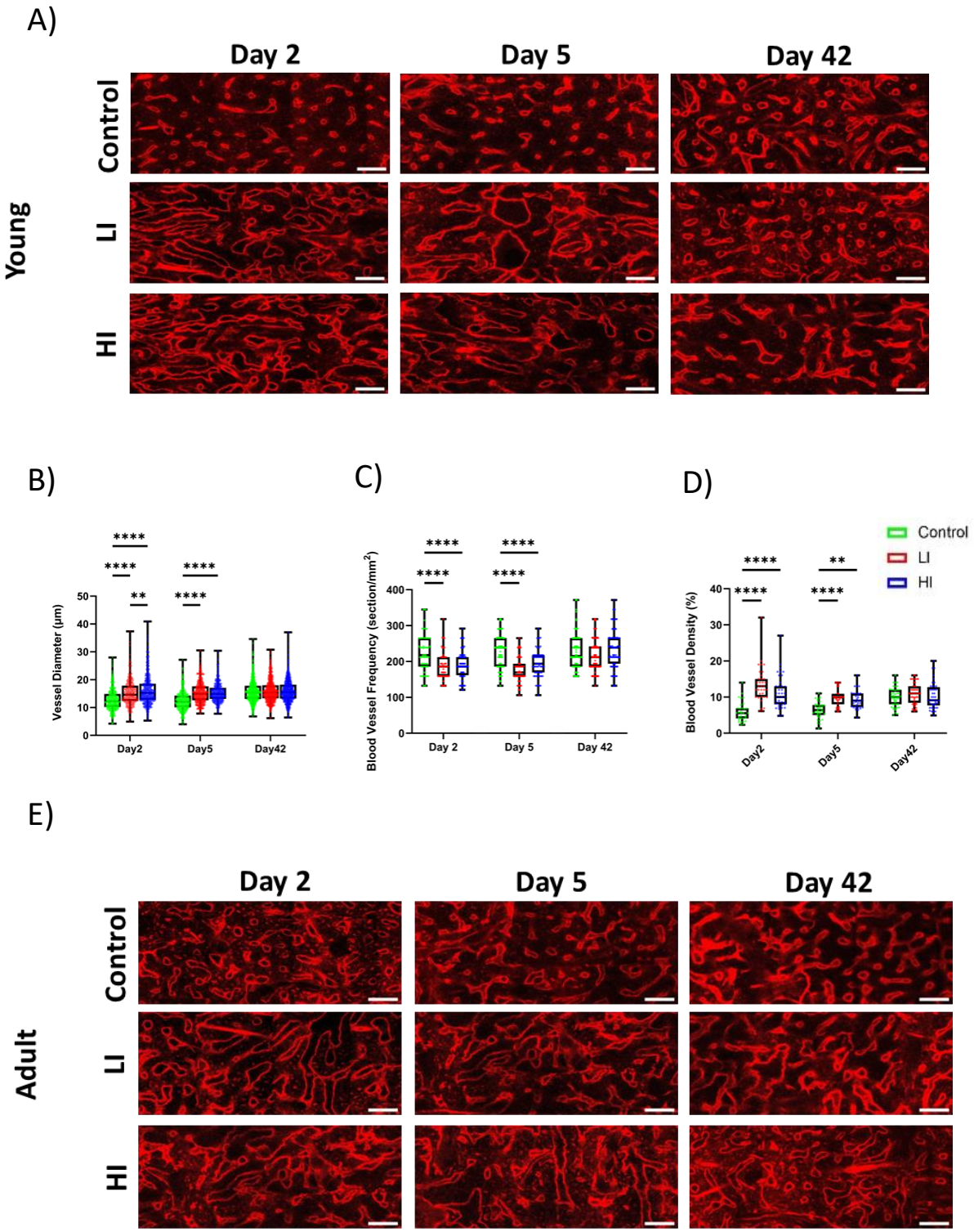
A)
Day 2
Day 5
Day 42
Control
LI
HI
Young
B)
Vessel Diameter (µm)
Day2
Day5
Day42
C)
Blood Vessel Frequency (section/mm²)
Day 2
Day 5
Day 42
D)
Control
LI
HI
Blood Vessel Density (%)
Day2
Day5
Day42
E)
Day 2
Day 5
Day 42
Control
LI
HI
Adult

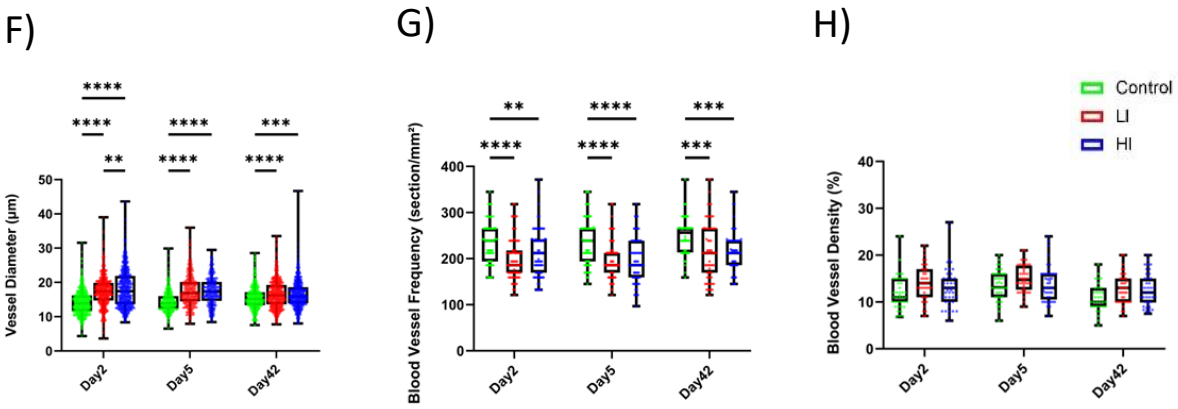

Figure 2.2. LI and HI Regimens Induce Morphological Alterations in BM Blood Vessels in Young and Adult Mice. **(A)** Representative images of the long bone BM blood vessel in control and LI/HI conditioned young mice over time; Red: blood vessel; **B-D)** Quantification of the vascular Diameter **(B)** Frequency **(C)** and Density **(D)** in control and LI/HI conditioned young mice over time. **E)** Representative images of the long bone BM blood vessel in control and LI/HI conditioned adult mice over time; **F-H)** Quantification of the vascular Diameter **(F)** Frequency **(G)** and Density **(H)** in control and LI/HI conditioned adult mice over time. scale bar: 50 µm; **p < 0.01, ***p < 0.001; ****p < 0.0001.

Furthermore, we evaluated the functionality of the BM vascular system through the blood vessel permeability, leakage, and blood flow velocity in calvaria BM after intravenous injection of Rhodamines-B Dextran (70kDa). In young mice, there was a significant increase in vascular leakage which remained until day 42 post HCT in LI and HI conditioned groups ($p < 0.0001$) compared to the control (**Fig. 2.3a, b**). In adult mice, long-lasting leakage caused by ECs disruption appeared to be dose-dependent and more significant in HI compared to the control and LI ($p < 0.0001$; **Fig. 2.3c, d**). The effect of busulfan dosage in vascular permeability of the young mice emerged at early timepoint (day2) where HI showed more permeability compared to LI ($p < 0.01$) and control ($p < 0.0001$). On day 5 post-transplantation, however, both LI and HI groups exhibited equal level of permeability compared to the control ($p < 0.0001$; **Fig. 2.3e**). In the adult group, busulfan conditioning caused high permeability only in HI group on day 2 post-transplantation ($p < 0.001$; **Fig. 2.3f**). Regardless of the animal age, permeability rebounded to the normal levels by day 42 (**Fig. 2.3e, f**). Blood flow velocity in busulfan conditioned mice remained consistent with control irrespective of the busulfan dose or age of the recipient (**Fig. 2.3g, h**).

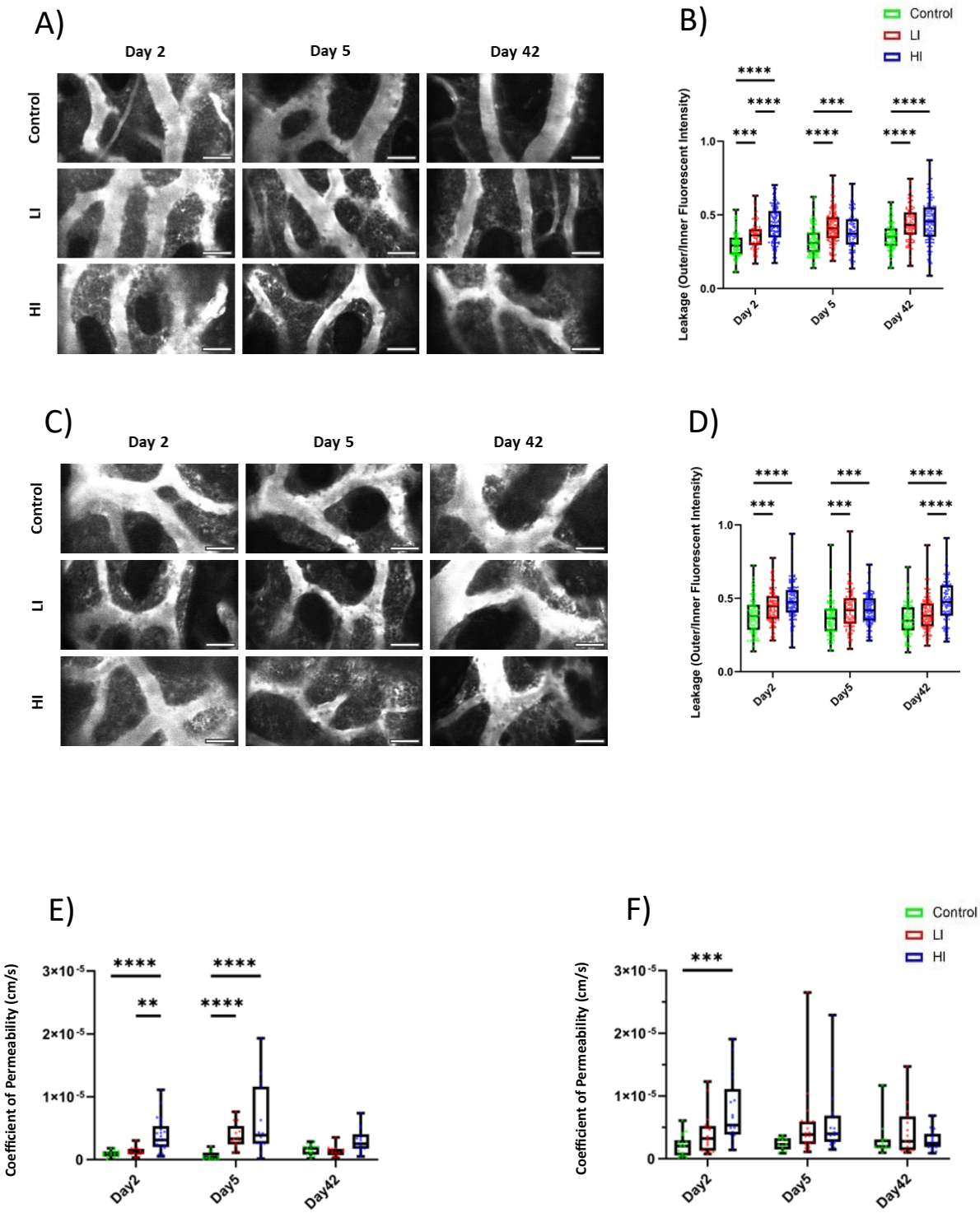
A)
Day 2
Day 5
Day 42
Control
LI
HI
B)
Control
LI
HI
Leakage (Outer/Inner Fluorescent Intensity)
Day 2
Day 5
Day 42
C)
Day 2
Day 5
Day 42
Control
LI
HI
D)
Leakage (Outer/Inner Fluorescent Intensity)
Day2
Day5
Day42
E)
Coefficient of Permeability (cm/s)
Day2
Day5
Day42
F)
Control
LI
HI
Coefficient of Permeability (cm/s)
Day2
Day5
Day42

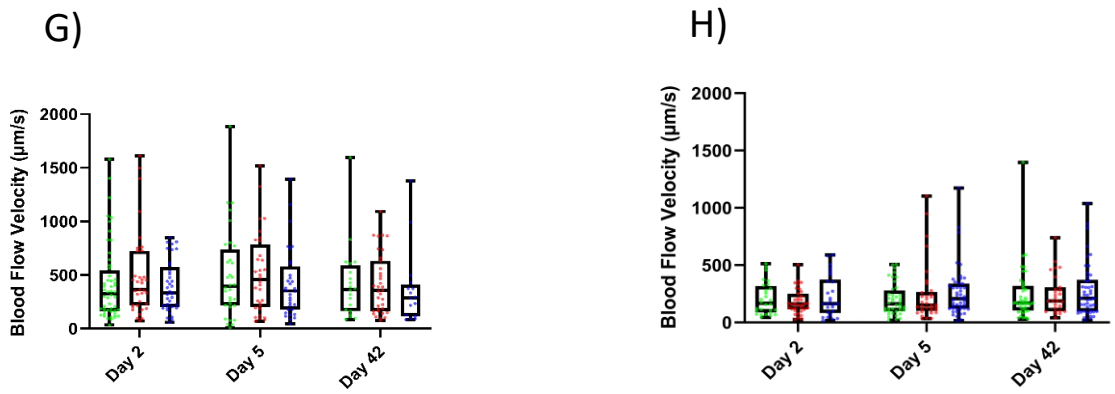

Figure 2.3. LI and HI Regimens Induce Disruption in BM Blood Vessel Barrier in Young and Adult Mice. A-B) Representative images **(A)** and Quantification of calvaria BM blood vessel leakage **(B)** in control and LI/HI conditioned young mice; White: blood vessel (Rhodamine B Dextran, 70 kDa); **C-D)** Representative images **(C)** and Quantification of calvaria BM blood vessel leakage **(D)** in control and LI/HI conditioned adult mice; **E-F)** Quantification of calvaria BM blood vessel permeability in Young **(E)** and Adult **(F)** mice; **G-H)** Quantification of calvaria BM blood flow in Young **(G)** and Adult **(H)** mice. scale bar: 50 µm; *p < 0.05, **p < 0.01,***p < 0.001; ****p < 0.0001.

Dose and Age Dependent Bone Remodeling Following Busulfan Conditioning and HCT. Recognizing that bone is not just a static provider of the BM compartment but actively interacts with the hematopoietic system, we speculated that busulfan administration may induce bone remodeling. To this end, we followed the protocol described in our previous paper from 2020, where we administrated Calcein (Dye 1) and Alizarin (Dye2) , two calcium-binding dyes, 48 hour and 30 minutes before imaging, respectively, to investigate the bone resorption-deposition profile based on the ratio of the two dyes[15] (**Fig. 2.4a**). In young mice, dose dependent reduction in the dye1/dye2 ratio along the endosteum of the long bone cavity appeared after 5 days in LI ($p < 0.05$) and HI ($p < 0.01$) mice and significantly increased by day 42 post-treatment in both groups ($p < 0.0001$) compared to the controls (**Fig. 2.4b, c**). However, in adult mice a slower bone turnover response was observed and dye1/dye2 ratio reduction was exhibited on day 42 only in the HI group ($p < 0.0001$; **Fig. 2.4d, e**). To further investigate the bone remodeling, we defined the long bone cavity as Deposition type (D-type; dye1/dye2 > 75%), Mixed type (M-type; dye1/dye2 25- 75%), and Resorption type (R-type; dye1/dye2 < 25%) based on the ratio of the two dyes as described before [15] (**Fig. 2.4a**). Classification results showed that increase in the R-type fractions is the key factor for the decrease in the dye1/dye2 ratio after busulfan conditioning (**Fig. 2.4f, g**).

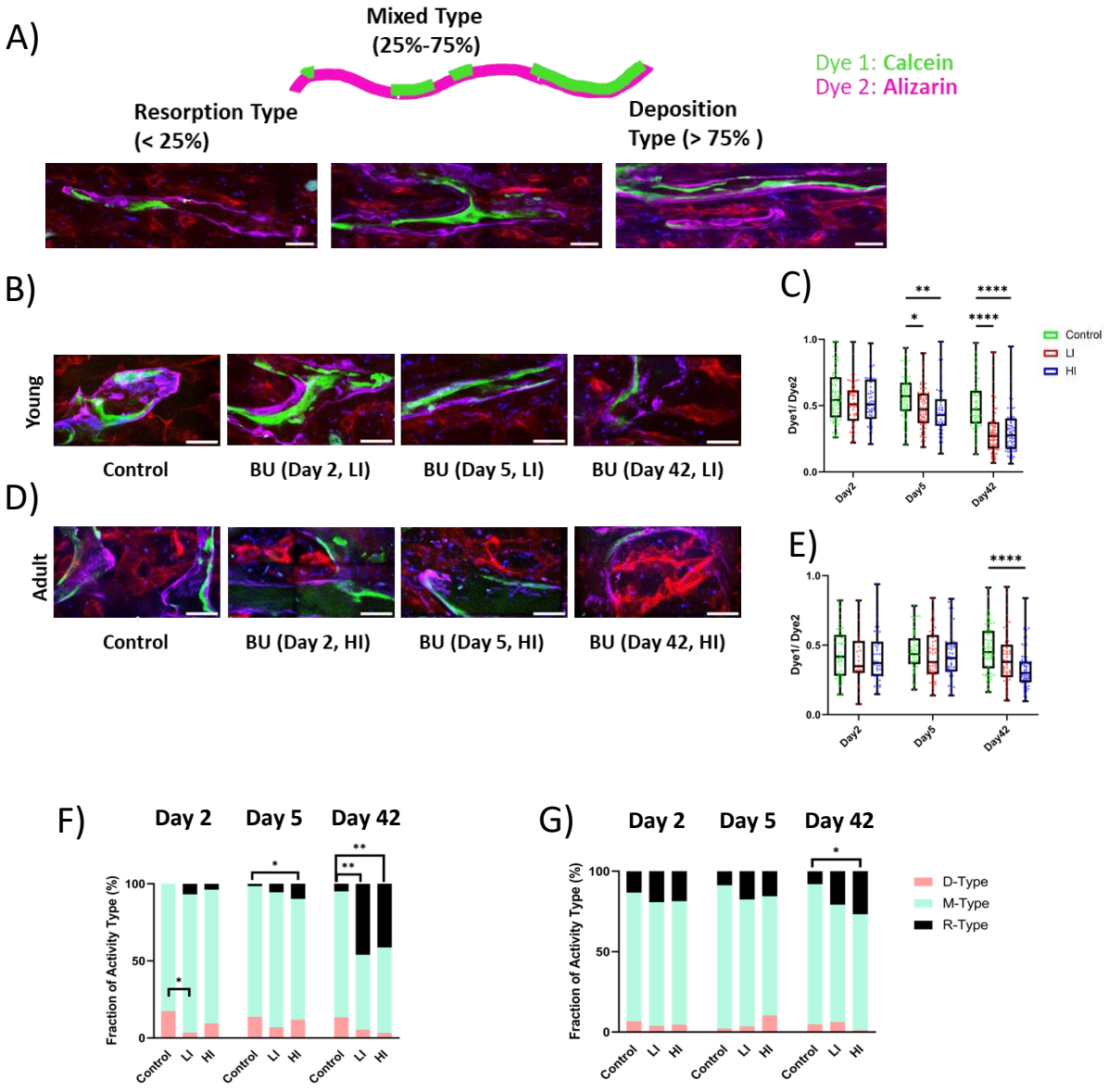

Figure 2.4. LI and HI Regimens Induce Bone Remodeling in Young and Adult Mice. A) Schematic representation of the double calcium staining illustrating D-, M- and R-type cavities; Green (dye1: Calcein), Purple (dye2: Alizarin); scale bar: 50 µm; **B-C)** Representative images **(B)** and quantification **(C)** of dye1/dye2 ratio in young long bone cavity; scale bar: 50 µm; **D-E)** Representative images **(D)** and Quantification **(E)** of dye1/dye2 ratio in adult long bone cavity; scale bar: 50 µm; **F-G)** Quantification of fractions D-, M- and R-type cavities in young **(F)** and adult **(G)** long bone cavity. *p < 0.05, **p < 0.01, ****p < 0.0001.

DISCUSSION

In this project, we investigated the longitudinal impact of busulfan conditioning on the BM niche in the context of HCT, with a focus on how the intensity of conditioning regimens and animal age influence this dynamic process. It is known that the intensity of conditioning and the recipient age can affect the donor cell engraftment after HCT[134,136–138], but less is known about the direct impact these factors have on the BM microenvironment. In our experiments, a more intense chemotherapy dose improved long-term engraftment in both young and adult mice. This effect is more prominent in adult mice where high engraftment was observed in HI mice but very few cells survived in the BM of LI and controls on day 42. High intensity regimens are known to more effectively eradicate recipient hematopoietic cells compared to low intensity regimens, providing an open BM microenvironment for donor cell engraftment[139,140]. In addition, chemotherapy treatment leads to an efficient hematopoietic recovery through stimulating the secretion of GM-CSF, a crucial factor for the proliferation of donor cells[141]. We also observed an overall better engraftment in young groups compared to the corresponding adult groups as expected. Interestingly, long bone image analysis revealed similar early homing kinetics between groups regardless of chemotherapy dose or age, even though long-term engraftment was higher in young mice compared to adults. This discrepancy is associated with the age-dependent alterations in the BM that make the BM less ideal for transplanted HSCs to engraft and repopulate such as the downregulation of stromal cell-derived chemokines (e.g. SDF-1), reduction of arterioles and their HSC regulatory cells (e.g. arteriolar NG2+, and PDGFβ+ cells) in endosteal regions, and increased generation of ROS[110,112,142–146].

Given the critical role that the BM niche plays in supporting hematopoiesis, we subsequently examined busulfan-induced changes to different microenvironmental compartments of the BM. Consistent with other findings, we observed increased blood vessel leakage and permeability as well as changes in the blood vessel morphology, size, and number at early days after cytotoxic treatment[74,75,104,106,108]. In addition, our experiments unexpectedly show that despite significant hematopoietic reconstitution, the blood vessels remain leaky on day 42 post-HCT suggesting that full recovery of the blood-bone marrow barrier requires more than 6 weeks or may never fully recover. Furthermore, morphological changes to the blood vessel network rebounded in young mice by day 42 yet remained altered in adult mice, likely due to decreased or delayed regenerative potential of aged BM. A decline in the number and function of MSCs, adipocyte accumulation, reduced angiogenesis, and increased secretion of inflammatory molecules are known age-associated factors that disrupt the BM microenvironment and contribute to delayed regeneration after cytotoxic damage[111,147,147–150].

Unlike the fast response of the vascular system to chemotherapy that begins as early as day 2, impacts to bone turnover rates appear delayed, particularly in aged mice, and become increasingly pronounced over time. Similarly, localized irradiation has been found to reduce the ratio of osteoblasts area to bone surface area (OB/BS) while increasing the ratio of osteoclast area to bone surface area (OC/BS) after two weeks post-exposure and persisting for a minimum of 12 weeks[103]. Furthermore, the application of double bone

labeling (Calcein/Alizarin) in femurs of mice subjected to Doxorubicin chemotherapy has revealed a decrease in the bone formation rate per bone surface (BFR/BS) and a reduction in the mineral apposition rate (MAR)[151]. This dynamic change in bone turnover is attributed to increased osteoclast activity and decreased osteoblast activity following conditioning[151,152].

The successful engraftment on day 42 despite observed persistent alteration in some components of BM such as vascular leakage or bone turnover is due to the distinct kinetics and mechanisms involved in recovery processes. While bone recovery is a complex and tightly regulated process that involves the coordinated activity of osteoclasts and osteoblasts, the hematopoietic reconstitution may not necessarily align with the bone restoration in terms of timing and dynamics. In this regard, clinical studies have revealed that bone loss does not compromise hematopoietic recovery and patients undergoing HCT show successful BM repopulation despite significant bone density loss within 6 months post-treatment[153]. While it has been evident that HSCs interact with various components in the BM microenvironment, additional research is needed to pinpoint the precise roles and the full extent of influence that each of these components exerts on hematopoietic recovery following transplantation.

Altogether, our findings highlight the distinctive influence of recipient age and chemotherapy dosage on the BM niche remodeling and donor cells repopulation in a comprehensive manner. This insight could potentially contribute fundamental knowledge to clinical oncology, particularly in understanding dose-response relationships for cytotoxic therapy in cancer patients of varying ages.

ETHICS STATEMENT

The authors declare no competing interests.

AUTHOR CONTRIBUTIONS

NA and JS contributed to experimental design, data collection, analysis, and manuscript writing. CB, RV, FG, and NT were involved in data collection and analysis.

FUNDING

This work was funded by the UC CRCC and through support of the NSF-CREST: Center for Cellular and Biomolecular Machines at the University of California, Merced (NSF-HRD-1547848 and NSF-HRD-2112675).

ACKNOWLEDGMENTS

We thank Dr. David Gravano from the SCIF and the staff of the DARS at UC Merced for their expertise in animal care and technical support.

Unpublished Findings

In this project, one of our goals was to quantitatively measure changes in oxygen tension within the BM alongside other associated alterations following cytotoxic conditioning. As part of this collaborative work, during my Ph.D. degree, I was able to complete the technical design of *in vitro* pO_2 calibration required for two-photon phosphorescence lifetime microscopy (2PLM). Beyond *in vitro* calibration within a chamber, I played a part in preparing the *in vivo* pO_2 calibration setup in a live mice. This section outlines my contributions to configuring the detection arm of our custom-built microscope for oxygen sensing, involving both *in vivo* and *in vitro* pO_2 calibration. In this regard, I contributed to write a chapter titled "*Two Photon Phosphorescence Lifetime Microscopy (2PLM)*":

Abbasizadeh, N., & Spencer, J. A. (2021). Two-Photon Phosphorescence Lifetime Microscopy. In Optical Imaging in Human Disease and Biological Research (pp. 63-82). Springer, Singapore. DOI: 10.1007/978-981-15-7627-0_4

Measurement of pO_2 in BM Tissue

BACKGROUND

Oxygen serves as a fundamental element in the BM microenvironment and is essential for many cellular activities such as self-renewal, survival, cell cycle quiescence, and multi-lineage differentiation[154–156]. Despite the highly vascularized structure of the BM, quantitative and non-quantitative oxygen tension measurements have revealed that compared to other organs, BM is a hypoxic tissue[157–159]. A non-invasive assessment of BM pO2 through 2PLM demonstrated that intravascular pO_2 in murine BM ranged from 11.7 to 31.7 mmHg, with a mean of 20.4 mmH and extravascular pO_2 ranged from range of 4.8 to 21.1 mmHg, with a mean of 13.3 mmHg[157]. Due to the crucial role of oxygen in various physiological and pathological conditions, numerous strategies have emerged over the years for quantitatively or semi-quantitatively measuring oxygen levels in blood and tissues. These approaches include techniques such as electron paramagnetic resonance (EPR), nitroimidazole (e.g., pimonidazole) adduct staining, and microelectrodes[160–162]. However, instrumental and probe administration restrictions for human subjects (in EPR), single timepoint measurement due to the destructive biopsy (in Nitroimidazoles) as well as oxygen consumption and potential tissue damage (in microelectrodes) are some of the limitations associated with these techniques limiting their applications[163–165]. Optical techniques, exemplified by phosphorescence lifetime quenching microscopy, however, offer a rapid, non-invasive means of quantitatively sensing oxygen in living biological samples without causing oxygen consumption. This method proves to be an optimal alternative to the aforementioned techniques[165]. Additionally, phosphorescence lifetime quenching measurements is independent of luminophore concentration, a crucial feature

when measuring oxygen tension in tissues and cells with heterogeneous distributions of probes or at different depths[166].

The mechanism of pO_2 quantification upon phosphorescence lifetime is based on quenching of phosphorescence probes with the surrounding O_2 molecules after simultaneous absorption of two photons. According to the Joblonski diagram **(Fig. 2.5)**, when a molecule is excited with one or two photons, it can release the energy in the form of fluorescent or phosphorescent. However, sometimes absorption of the energy by some neighboring molecules such as oxygen, can cause phosphorescence quenching resulting in a decrease in light intensity and lifetime[167,168]. Hence, as oxygen concentration increases, the phosphorescence lifetime decreases. Prior to conducting *in vivo* quantification, it is necessary to create a calibration curve that demonstrates the relationship between phosphorescence lifetime and various concentrations of oxygen. Generating such a calibration curve is essential for measuring the partial pressure of oxygen (pO2) in live animals based on phosphorescence lifetime measurements.

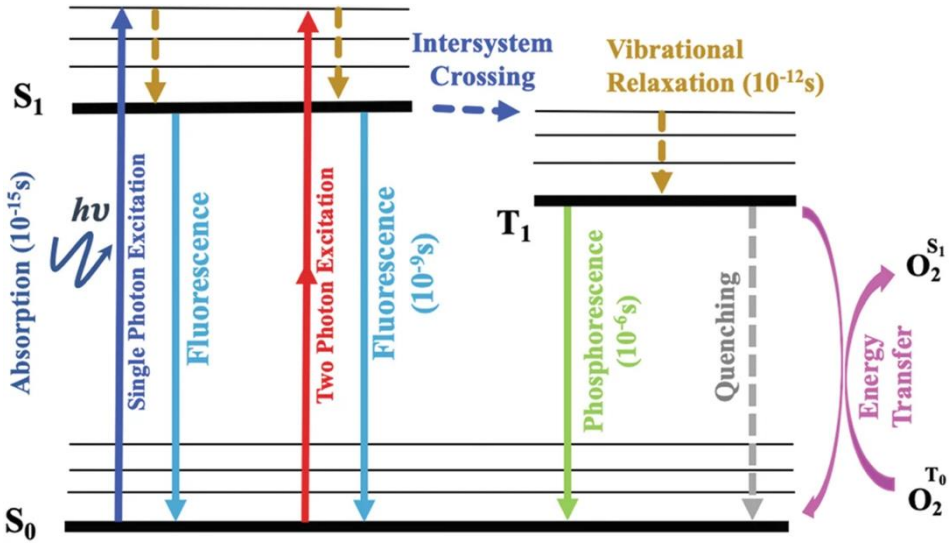

Figure 2.5. Jablonski Energy Diagram. Single-photon and two-photon excitation are shown as blue (UV-Visible wavelengths) and red (NIR wavelengths) arrows, respectively. Quenching of the triplet state (T1) by bimolecular oxygen (O_2 T0) results in the production of singlet oxygen (O_2 S1) and the regeneration of the ground state phosphor (S0) (*Abbasizadeh, N., 2021*).

METHOD

In Vitro pO_2 Calibration Inside the Chamber.

In order to conduct the *in vitro* pO_2 calibration, a phosphorescence probe which is sensitive to the oxygen molecule will be dissolved inside the chamber. Then while a gradient of the

nitrogen molecule is being bubbled to gradually decrease the oxygen concentration, at the same time the pO_2 and the probe phosphorescence lifetime will be recorded using an oxygen electrode and 2PLM system respectively to plot the calibration curve. Phosphorescence lifetime measurements are typically obtained in the time domain. This involves creating an excitation gate by passing the laser through the electro-optic modulator (EOM) generating tens to hundreds of individual laser pulses. As depicted in both AutoCAD and the actual configuration of the *in vitro* calibration setup **(Fig. 2.6)**, to segregate the oxygen detection pathway from the imaging pathway, a mirror (number 2) was positioned to redirect the laser path toward the calibration system.

Following its travel through various optical components such as dichroic mirrors, telescopes, the pupil, and band-pass filters, the light is focused by the objective lens onto the phosphorescence molecule within the cuvette. The cuvette functions as the *in vitro* calibration chamber, where the dissolved oxygen probe is exposed to N2 gas. After molecule excitation, the emission light retraces its path through the objective to the photomultiplier tube (PMT) to detect phosphorescence signals from the sample.

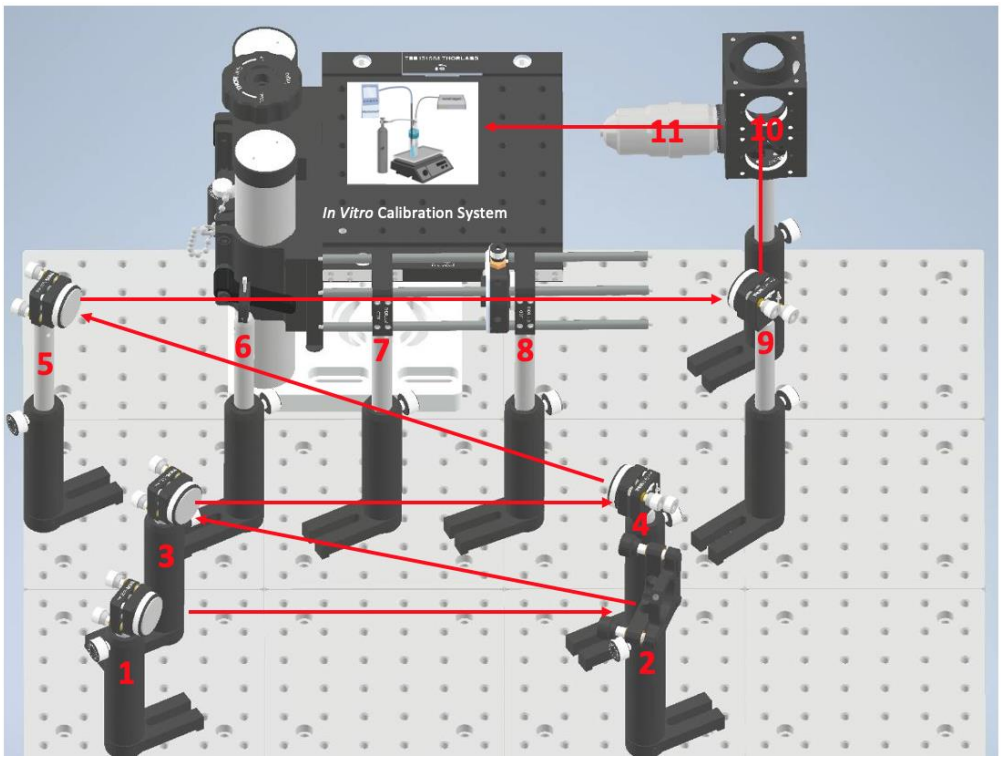

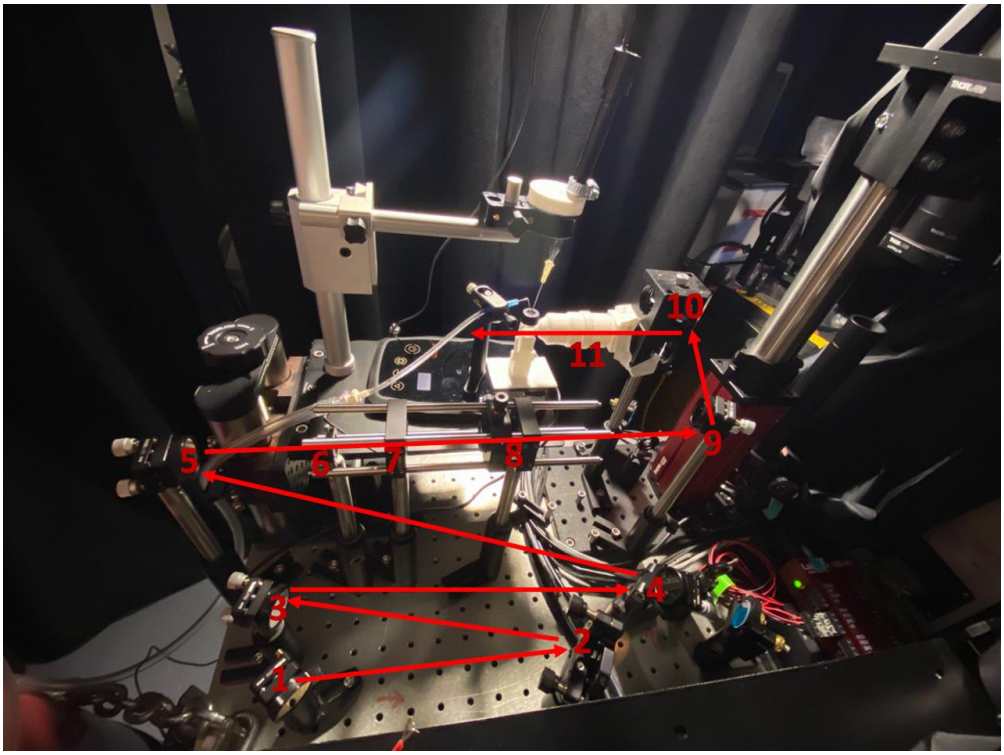

Figure 2.6. Schematic (Top) and Optical Configuration (Bottom) of *In Vitro* pO_2 Calibration.

In general, in our system the calibration chamber incorporates three ports to insert the oxygen electrode (Unisense; OX-500), N_2 gas tubing, and thermometer (Digi-Sense). The oxygen electrode is used to quantify the pO_2 (Port 1) while different concentrations of oxygen are being induced through gas port (port 2). The thermometer (port 3) monitors the temperature during the calibration since according to the Stern–Volmer formula, change in the temperature affects the pO_2 value. In Stern–Volmer equation:

$$I_0/I = \tau_0=\tau = 1 + Kq \times \tau_0 \times [Q] ,$$

I_0 and τ_0 are the intensity and lifetime of phosphorescence emission in the absence of quencher, I and τ are the intensity and lifetime at a specific concentration of quencher [Q], and Kq is the quenching constant. In this formula, the quenching constant is tightly dependent on temperature, exhibiting a fundamentally linear relationship between these two parameters. This highlights the importance of maintaining precise temperature control close to the animal body (37°C). To address the issue of temperature drop resulting from bubbling N_2 gas during calibration, my lab mate, Mario Muniz, devised a heating element integrated with a regulator. The regulator effectively restores the temperature to the defined value by continuously monitoring the temperature inputs recorded by the thermometer.

The functionality of the thermoregulator was verified by the graph in **Fig. 2.7**. In absence of the regulator, a decrease in oxygen concentration leads to a temperature drop from 36°C to below 20°C while in the presence of regulator, temperature fluctuations are mitigated to less than 2°C, and they change around 35°C, confirming the efficacy of the thermoregulatory system.

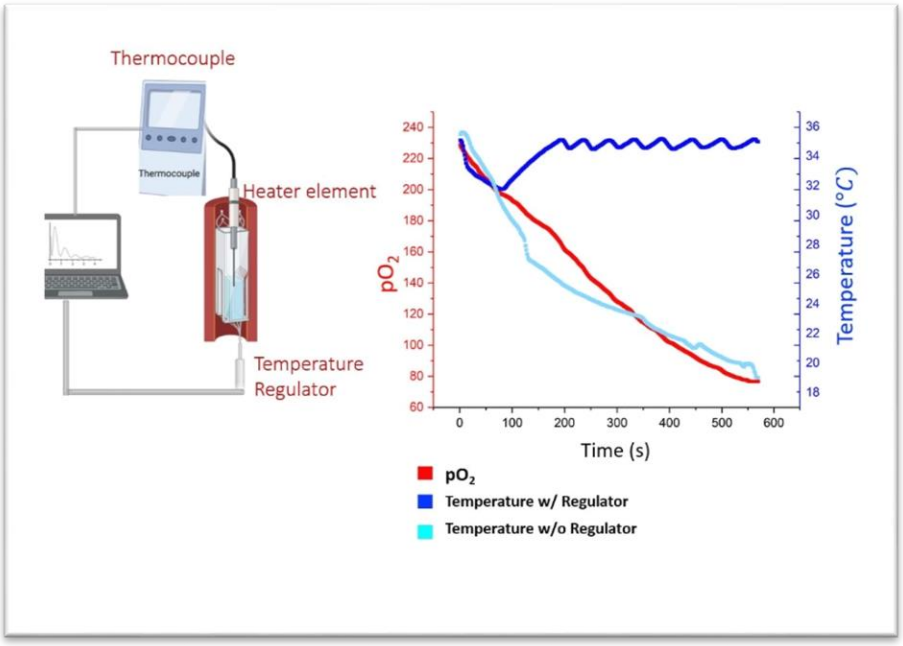

Figure 2.7. Function of Thermoregulator in Controlling the Temperature During N_2 Gas Bubbling.

In Vivo pO_2 Calibration Inside Live Mice Blood Vessels

Accurate calibration has a crucial role in precise oxygen quantification through phosphorescence lifetime measurement. Currently, all oxygen sensing calibrations are performed within the *in vitro* chambers, as discussed in the previous section. While this approach is advantageous for detecting a broad range of oxygen concentrations, it cannot perfectly represent the conditions in the physiological conditions within the mouse body. To address this limitation, our laboratory seeks to conduct calibrations inside live animals for the first time to assess whether *in vitro* calibration curve is identical to the *in vivo* plot. To achieve this aim, a probe will be injected into mice, and an oxygen electrode will be carefully inserted horizontally into an artery or vein. By systematically altering the oxygen concentration in the inhaled gas, we will quantify pO_2 and lifetime using the oxygen electrode and 2PLM system, respectively, to construct the calibration graph **(Fig. 2.8a)**. The selection of the vessel for calibration was guided by two primary considerations: minimally invasive surgery to maintain the mice in their normal physiological conditions and the preference for a location relatively distant from the heart to mitigate the impact of

heartbeat motions on the measurements. Our initial attempts with the femoral vessel appeared challenging due to the very small size of the vessel, making it difficult to insert the oxygen electrode **(Fig. 2.8b)** (Unisense; OX-100). We later transitioned to the tail vein as it has a larger vessel, requires low invasive surgery, and is more distant from the heart **(Fig. 2.8c)**.

Given the fragility of the oxygen electrode, preliminary practice involved using glass pipettes with the same outer diameter. As depicted in **Fig. 2.8d**, a successful imaging of the pipette tip, (where the oxygen electrode is supposed to be placed in the real experiment) was achieved. To enhance the stability and precision of the electrode's movement toward the tail, the oxygen electrode was mounted to a 3D-printed holder integrated with a micromanipulator featuring XYZ fine adjustment at the micron scale.

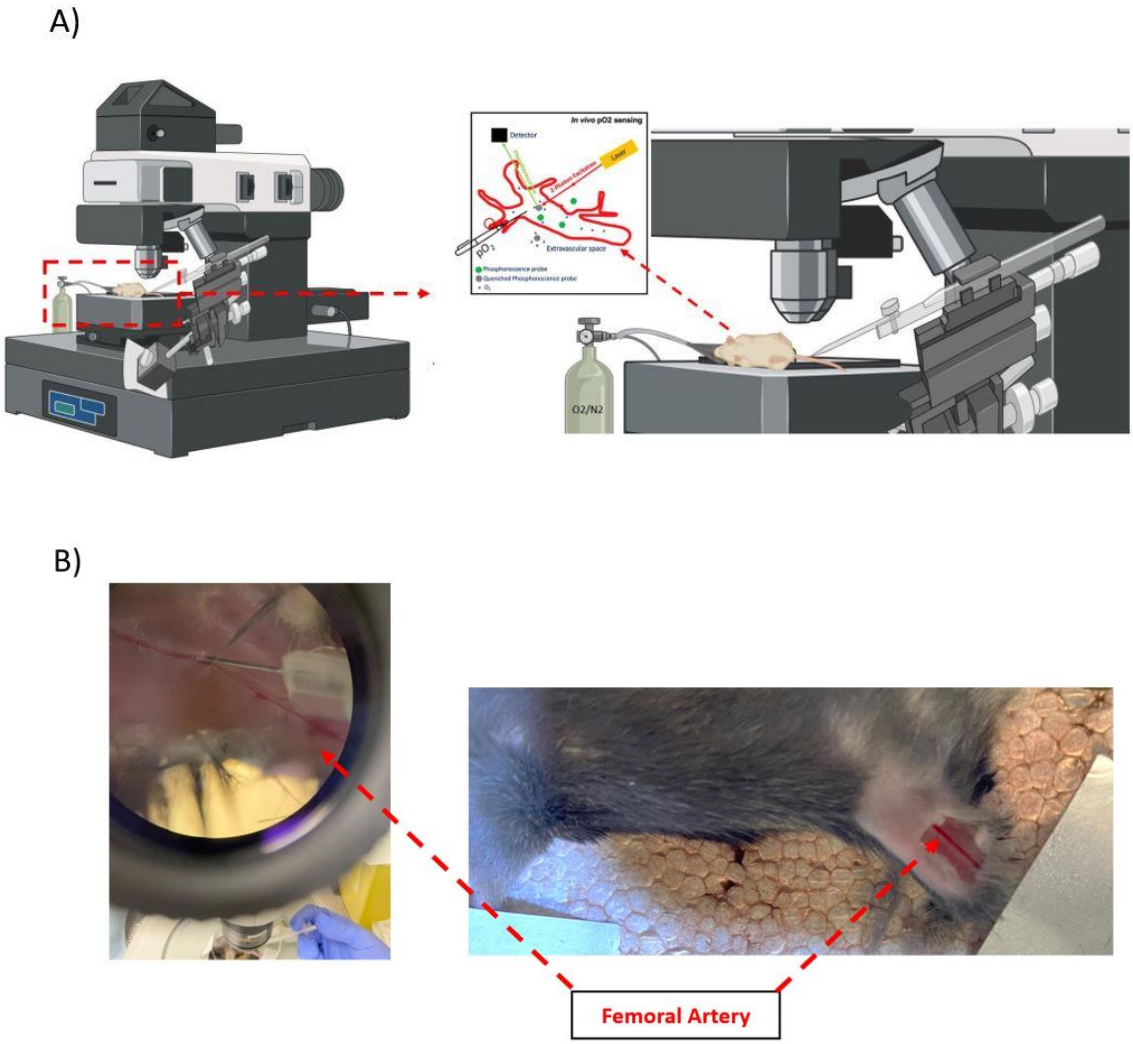

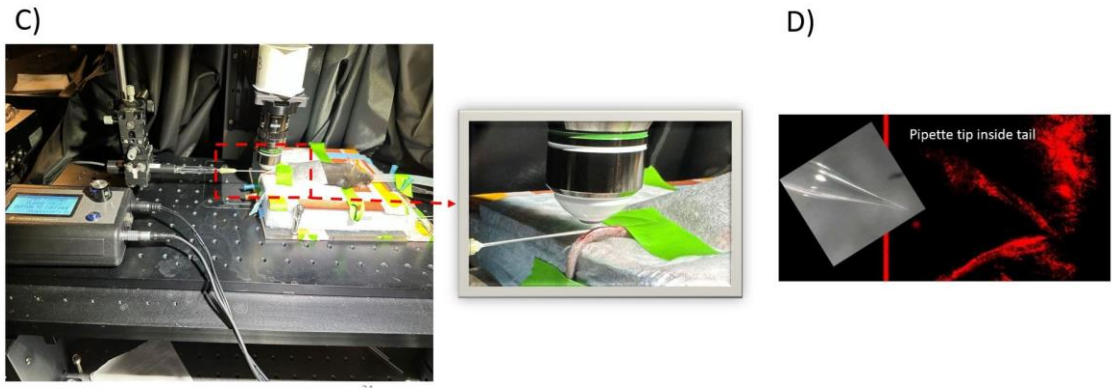

Figure 2.8. *In Vivo* pO_2 Calibration Set up. (A) Schematic of *in vivo* pO_2 calibration; **(B)** Femoral artery in adult mouse; **(C)** Technical design of oxygen probe insertion into mouse tail vein; **(D)** Representative image of glassy pipette inside tail under objective.

Taken all together, the technical configuration for *in vivo* and *in vitro* pO_2 calibrations has been established. The subsequent phase in our laboratory involves validating the functionality of the 2PLM system and executing the calibration within the designed setup. It will be of interest to evaluate its function on both *in vitro* and *in vivo* studies.

CHAPTER 3

Investigation of the BM Microenvironment Around AML Tumor Cells Before and After Cytotoxic Conditioning.

Brief Summary

In this chapter, we utilized intravital 2P microscopy and flow cytometry techniques to investigate the BM niche in an AML mouse model both before and after cytotoxic conditioning with a combination of Bu/Cy. Our primary objective was to evaluate the elements of the bone marrow microenvironment that support tumor resistance following chemotherapy.

Key Findings:

- **Effect of AML Progression on the BM**: We employed BM imaging techniques in both long bones and the calvarium, along with flow cytometry analysis of chimerism in both BM and peripheral blood (PB) to classify the progression of AML. Additionally, we assessed vascular alterations, including changes in blood flow velocity, vascular leakage, and blood vessel diameter to obtain a better understanding of the BM niche changes upon different stages of the AML. We classified AML disease into three stages of early, middle, and late and found AML progression alters the BM mainly between middle and late stage.

- **Distribution of Tumor Cells**: We examined the distribution of AML cells across different stages of the disease, providing insights into their localization within the BM microenvironment. Our analysis showed that distribution of tumor cells changes across the disease.

- **Identification of Effective Chemotherapy Protocol**: We found that single therapy with busulfan fails to effectively halt the progression of AML tumors whereas combination therapy with busulfan/cyclophosamide exhibits therapeutic outcomes.

- **Characterization of Vascular Niche**: We conducted assessment of the functional and structural characteristics of the vascular niche surrounding resistant tumor cells. This included evaluating the vascular leakage, blood flow velocity and morphology of the vascular network. Overall, our images showed that the BM niche surrounding residual AML cells facilitates chemotherapy resistance.

Investigation of the BM Microenvironment around AML Tumor Cells Before and After Cytotoxic Conditioning.

Nastaran Abbasizadeh[1,2,3], Orlando Hernandez[1], Marlene Marquez Villanueva[1], Robert Dudkin[1], Christian Burns[1,2,3], Joel A. Spencer[1,2,3,4]*

[1]*Department of Bioengineering, School of Engineering,* [2]*Center for Cellular and Biomolecular Machines,* [3]Quantitative and Systems Biology Graduate Program, [4]*Health Sciences Research Institute, University of California, Merced, Merced, CA, United States.*

*Correspondence: joel.spencer@ucmerced.edu

ABSTRACT

AML patients frequently experience relapse following remission due to the resistance of some leukemia cells to chemotherapy. Characterization of the BM niche around surviving AML cells provides a precise understanding of the factors mediating the disease recurrence. In this study, using intravital 2P microscopy, we evaluated BM microenvironment adjacent to the resistant tumor cells after Busulfan/Cyclophosamide (Bu/Cy) conditioning. To identify the optimal timepoint at which the disease burden reaches a suitable level for the initiation of treatment, we classified the AML progression into early, middle, and late stages. Based on the PB and BM flow cytometry chimerism, calvaria and long bone images, and vascular analysis across different stages, a timepoint between early and middle stages was selected for chemotherapy treatment. Analysis indicated that residual AML cells after Bu/Cy therapy intend to home within the endosteum, primarily at metaphysis, where tumor cells are protected from chemotherapy-induced apoptosis. BM tissue appeared to exhibit distinct responses in the calvarium and long bone with more surviving tumors cells in the long bone. Blood vessel network was severely impaired in regions with residual AML cells compared to the other BM areas. Vascular analysis in calvaria BM adjacent to the tumor cells showed higher blood vessel leakage and comparable flow velocity compared to the other regions. Overall, this study offers insights into the BM niche surrounding residual tumor cells by characterizing the AML BM microenvironment throughout disease progression and optimizing treatment plans.

INTRODUCTION

AML is classified as a hematological malignancy arising from genetic mutations within myeloid hematopoietic progenitors[169–171]. These mutations lead to an obstruction in the maturation process and uncontrolled proliferation of leukemic blasts within the bone BM[37]. Standard intensive chemotherapy regimens play a fundamental role in achieving complete remission (CR) in AML. The CR rates range from 60-85% for adults under 60 years and 40-60% for individuals aged 60 years or older[172,173]. However, despite CR following treatment, relapses are often observed in 60% (young) to 80% (elderly) of patients[172].

The BM microenvironment, where leukemic cells originate and proliferate serves as a protective niche for AML cells, allowing them to evade the effects of chemotherapy[37]. There is increasing evidence to support a crosstalk between leukemic cells and the BM niche components[40,174–176]. BM microenvironment anatomically contains endosteal and vascular niches[171,177]. The vascular niches, primarily composed of sinusoidal ECs and pericytes, have been documented to facilitate the growth of AML and contribute to chemoresistance. CXCL12 and angiopeitin-1 expression by vascular niche facilitate the retention of AML cells within the vascular niche, promoting their growth[178–180]. VEGF, a key factor in angiogenesis, provides AML cells with better access to nutrients and oxygen[181]. In addition, various chemokines and cytokines produced within the vascular niche play a role in promoting AML cell survival and chemoresistance[182]. Endosteal niche, as another BM component, could promote tumor cell adhesion, migration, and survival by providing physical support and signals such as OPN or CXCL12[183,184]. Taken together, it is critical to characterize the stem cell niche around tumor cells with the aim of understanding and targeting the factors facilitating drug resistance.

In order to provide therapies with effective outcomes for AML patients, it is crucial to characterize the behavior of leukemic cells in BM such as how they proliferate, outcompete normal hematopoiesis, and ultimately establish an environment supporting chemotherapy resistant. The introduction and advancement of intravital 2P microscopy have enabled the direct, high-resolution, and dynamic imaging of the calvarium BM[15,185–187]. In this study, using 2P microscopy, we aim to evaluate the BM niche alterations in an AML mouse model before and after chemotherapy treatment with Bu/Cy. Bu/Cy combination has long been considered as a common MAC regimen for allogeneic hematopoietic cell transplantation (alloHCT) in both nonmalignant diseases and myeloid malignancies[61,188,189]. Targeting associated factors within the BM niche may offer potential strategies for disrupting AML growth and enhancing the efficacy of treatments.

We revealed (1) progression of AML disease in the BM across three phases of early, middle, and late stages; (2) morphological and functional alteration in the BM vascular system; (2) Preferential localization of tumor cell across AML progression; and (4) BM niche around residual AML cells after BU/CY combination therapy.

MATERIAL AND METHOD

Animals

Female C57BL/6J, C57BL/6 CD45.1 (B6.SJL-Ptprca Pepcb/BoyJ), Gt(ROSA)26Sortm4 (ACTB-tdTomato,-EGFP)Luo/J (mTmG), and C57BL/6-Tg(UBC-GFP)30Scha/J transgenic adult mice (8-12 weeks) were purchased from Jackson laboratory. Mice were bred and housed in the DARS at UC Merced. The animal study received approval from the IACUC at the University of California, Merced.

Cell Lines and Culture Condition

Cells were cultured at 37°C with 5% CO_2 in a humidified atmosphere. Murine AML cell lines (C1498-EGFP; Imanis Life Science) were maintained in RPMI-1640 medium (ThermoFisher; A1049101) supplemented with 10% fetal bovine serum (FBS) and 1% Penicillin/Streptomycin (Fisher scientific; 15140122). The cells were subcultured to maintain a density between 3 x 10^5 and 2 x 10^6 cells/mL as recommended by the company.

Murine AML

The AML mouse model was generated by tail vein injection of C1498-EGFP cells into sub-lethally (4.5 Gy) irradiated C57BL/6J and C57BL/6 CD45.1 mice. AML cells were centrifuged at 350 x g for 5 minutes, washed with 5 ml of cold PBS, and a suspension of 1.0×10^6 cells in PBS was prepared for injection[190].

Chemotherapy Treatments and Whole BM Cell Transplantation

To conduct the chemotherapy treatment, AML mice received 80 mg/kg of BU (Cayman Chemicals Company; 14843) and 100 mg/kg of CY (Millipore Sigma; C0768-1G) via IP injection. BU and CY solutions were prepared immediately before injection. Briefly, busulfan crystals were dissolved in DMSO (Sigma Aldrich; 472301) and Ca+/Mg+ free PBS (gibco; 2003901) was added to the solution to make a final drug concentration of 1mg/ml in 10% DMSO. The working solution was filtered through a 0.22 µm syringe filter (Fisherbrand; R7PA99681) and was administered to mice in separate doses of 20 mg/kg/day for 4 consecutive days[127]. The same protocol was applied to prepare CY dissolved in 0.01% DMSO. CY was administered to mice in separate doses of 50 mg/kg/day for 2 consecutive days.

One day following BU/CY conditioning, 8-12 week membrane-Tomato/membrane-Green (mTmG) transgenic donor mice were euthanized by CO_2 inhalation and cervical dislocation. Long bones were harvested, cleaned, and crushed in FACS buffer. The resulting cell mixture was filtered through a 40 µm filter into a 50 ml falcon tube and centrifuged at 1500 rpm for 5 minutes at 4°C. After removing the supernatant, the pellet was resuspended in ACK lysis buffer to eliminate erythrocytes. The reaction was halted after a 1-minute incubation by adding FACS buffer, and cells were washed by centrifugation at 2000 rpm for 3 minutes at 4°C. Subsequently, cells were resuspended in

PBS, and a cell count was conducted using a hemocytometer and Trypan Blue staining (Gibco, 15250-061). Finally, a suspension of 1×10^6 cells/ml was administered via retroorbital injection.

Flow Cytometry

To monitor the engraftment and expansion of tumor cells, PB chimerism was assessed after tumor transplantation. To collect PB, mice were exposed to a heat lamp to enhance blood circulation. Subsequently, the mice were restrained, and a small incision was made over the ventral tail vein using a scalpel blade. Blood samples (no more than 10 drops) were collected into blood collection tubes coated with K2EDTA (BD Microtainer; 365974). Heparinized blood was diluted with 9 ml of diH2O for RBC lysis, followed by the immediate addition of 1 ml of 10x PBS to prevent lysis of white blood cells. The cells were then centrifuged at 2000 rpm for 5 minutes at 4°C. After removing the supernatant, the pellet was resuspended in 9 ml of diH2O and 1 ml of 10x PBS to further remove remaining RBCs. Following another centrifugation step at 2000 rpm for 3 minutes at 4°C, 100 µl of the sample was aliquoted into 96 V-bottom wells for FACS staining. The cells were washed with 100 µl of FACS buffer and centrifuged at 2000 rpm for 3 minutes at 4°C. The supernatant was removed, and the cells were resuspended in 200 µl of FACS buffer for flow cytometry analysis of chimerism.

To study immune cell distribution on day 42 post UBC-GFP transplantation, PerCP-Cy5.5 CD19 (1:100), APC-CY7 CD11b (1:100), PE/Cy7 Gr-1 (1:100) and APC CD3 (1:100) were used.

For BM chimerism, tumor-transplanted mice were euthanized by CO_2 inhalation, and the same procedure as described previously for whole BM transplantation was followed to collect cells. The collected cells were resuspended in PBS, and a suspension of 1×10^6 cells/ml was prepared for staining. After a 15-minute incubation with APC/Cy7 CD45.2 (1:100), the cells were washed with FACS buffer, centrifuged, and resuspended in 200 µl of FACS buffer for flow cytometry analysis of chimerism[191]. To study the tumor distribution in long bone, epiphysis and metaphysis were separated from the growth plate region before they were crushed for the flow cytometry.

Graft-Versus-Host Disease (GVHD) Evaluation

To evaluate GVHD, PB from control, BU, and BU/CY treated groups were collected and the same protocol as PB chimerism was followed to prepare the cells for staining. Cells were then incubated with PE-CY7-A CD4 (1:100) and PerCP-cy5.5 CD25 (1:100) for 15 min, washed with FACS buffer, centrifuged, and resuspended in 200 µl of FACS buffer for flow cytometry analysis of T_{reg} population. In addition, animals were scored for five GVHD clinical parameters of weight loss, posture, activity, fur and skin on a scale from 0 to 2 resulting in a total score that ranges from 0 to 10. Regarding the weight loss < 10, >10% to <25%, and > 25% were scored 0, 1, and 2 respectively. Mice were regularly examined every 3 day for 42 days.

Two Photon *In Vivo* and *Ex Vivo* Imaging

In vivo calvaria and *ex vivo* femur imaging was performed with a custom-built two-photon intravital microscope (BLIQ Photonics). A 25x fluid immersion objective (Olympus; XLPLN25XWMP2, NA = 1.05) was used for all images, with an approximate FOV of 317 µm by 159 µm. During live imaging, two tunable femtosecond lasers, MaiTai (Spectra Physics; MaiTai eHP DS) and Insight (Spectra Physics; Insight X3), were tuned to 800 nm and 950 nm to observe 70 kDa Rhodamine-B Dextran (ThermoFisher, D1841) and GFP+ tumor cells signals, respectively. For *ex vivo* imaging of long bones, the MaiTai and Insight lasers were tuned to 950/1220 nm to excite GFP, Alexafluor 647 conjugated vascular antibodies, and SHG, respectively. Wavelengths of 990/1220 nm were used to excite GFP, tdTomato, Alexafluor 647 conjugated vascular antibodies, and SHG in AML mice after mTmG transplantation.

For *in vivo* visualization of the calvaria BM, anesthesia was induced via initial inhalation of 3-4% isoflurane with 100% O_2 at 1 L/min that was reduced to 1.5% as maintenance. The skull was secured in a custom head mount that was equipped with a heating pad to maintain the animal body temperature during the procedure. After shaving top of the head, a small incision was made along the sagittal and lambda suture of the skull to expose the calvarium as described before[129].

For *ex vivo* imaging of the long bone, mice were injected retro-orbitally with Alexafluor 647 conjugated vascular antibodies (CD31; 102516, Biolegend, Sca-1; 108118, Biolegend, VE-Cadherin; 138006, Biolegend) 30 minutes before intracardiac perfusion. Mice were perfused with 1x PBS to wash out the blood followed by 4% PFA (Fischer Chemical; 1638384) to internally fix the tissue. Subsequently, femurs were harvested and fixed in 4% PFA for 30 minutes, at 4°C. The bones were then washed with 1X PBS, immersed in 30% sucrose (Sigma; SLCC8492) for 1 hour, frozen in OCT (Fisher Scientific; 4585) compound and kept at – 80°C. Samples were shaved using a cryostat (LEICA CM1860) equipped with a high-profile blade (Leica; 3802121) to expose the BM region.

Image Quantification

We utilized Fiji (ImageJ 1.53t) for image processing, which included quantifying vessel leakage, assessing morphological changes to blood vessels, and measuring tumor cell size. Custom scripts in MATLAB (2020a) were employed to calculate BM blood flow velocity. To investigate changes in the vascular system within the calvaria BM, we administered 70 kDa Rhodamine-B Dextran retro-orbitally during *in vivo* imaging. Vascular leakage was measured using z-stack images (2 µm z step) captured 10 minutes after dye administration, as previously described. Leakage was quantified based on the ratio between the fluorescent intensity in the perivascular space and the fluorescent intensity in the adjacent vascular lumen. Blood flow velocity was determined by recording 30-second videos of blood flow in the BM calvaria and then applying LSPIV using a custom MATLAB script, as described in previous studies[130].

RESULTS

AML Progression Alters Vascular Morphology and Function. To establish an AML mouse model, 10^6 tumor cells were injected into the sublethally irradiated mice. Irradiation helps suppress the immune system of the mice, allowing better engraftment and growth of the tumor cells in the mouse model. Successful engraftment of AML cells was assessed through PB chimerism on day 14 post injection. Considering the challenging nature of tail vein injections in B6 mice with dark skin, tumor cells were initially administered via the retro-orbital cavity. Despite successful engraftment of tumor cells in the BM, some animals exhibited tumor growth within the eye cavity, leading to tumor bulk formation and, in some instances, eventual blindness post-injection **(Fig. 3.1a)**. Consequently, the protocol was modified to utilize tail vein injections with slight adjustments in which a catheter was employed to connect the needle to the syringe. Based on the capillary rule, whereby blood flows back into the catheter upon successful needle insertion into the vessel, we could ensure the technical success of the injection process **(Fig. 3.1b)**. Consistent with other literature, the Kaplan-Meier curve for the C1498 AML cell line revealed a similar survival rate in tumor-injected mice[192–194]. All recipient mice died within 23–39 days with a median survival of 29 days **(Fig. 3.1c)**. To initiate cytotoxic conditioning, it is essential to determine a time point where the disease burden is relatively low so that individual patches of AML cells in the BM could be detected after treatment. Therefore, based on PB and BM chimerism alongside long bone *ex vivo* imaging, AML disease progression was categorized into three stages **(Fig. 3.1d, e)**. This categorization allows for a more precise understanding of the disease burden before the administration of chemotherapy. These stages consist of an early stage characterized by a seemingly random distribution of single cells throughout the BM tissue, a middle stage where tumors begin forming clusters, and a late stage marked by high tumor infiltration in the BM **(Fig. 3e)**. PB and BM chimeric graphs indicated that as the disease progresses to the late stage, they diverge significantly, suggesting that PB chimerism no longer effectively represents the extent of tumor infiltration in the BM **(Fig. 3.1d)**. While PB chimerism may not precisely reflect the level of tumor infiltration in the BM during the middle and late stages, the gradual increase in tumor population observed in the PB across different stages can still offer valuable insights into the AML stage. AML-induced alterations within the blood vessel system across AML progression revealed a significant increase in vascular leakage and decrease in blood flow velocity at a specific juncture between the intermediate and advanced stages of the disease **(Fig. 3.1f, g)**. Furthermore, vascular diameter examination revealed larger vessels in the late stage compared to other stages or the control group **(Fig. 3.1h)**.

A)

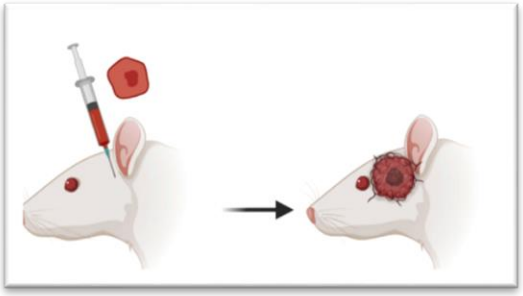

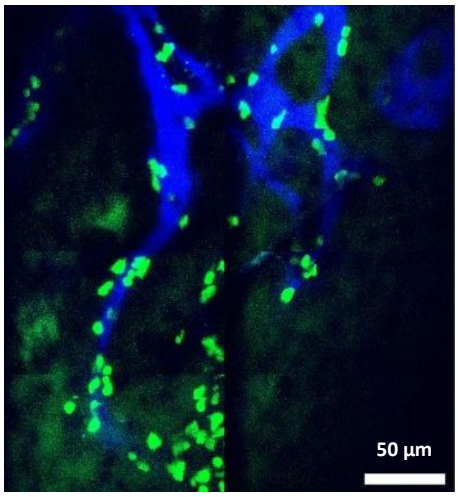
50 µm

B)

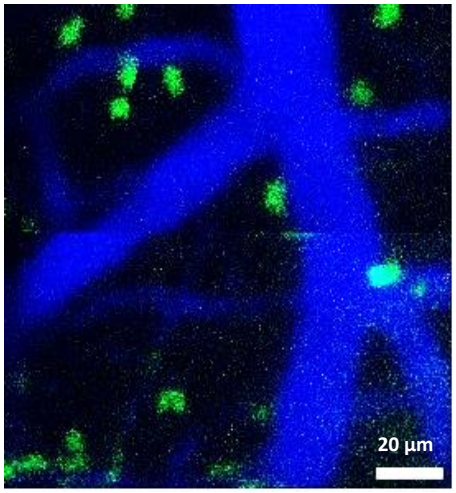
20 µm

C)

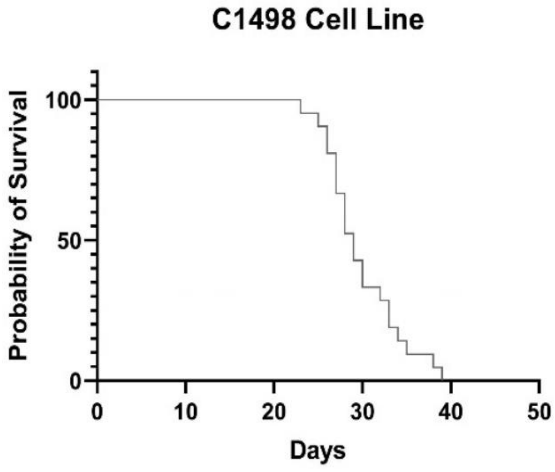
C1498 Cell Line
Probability of Survival
100
50
0
0
10
20
30
40
50
Days

D)

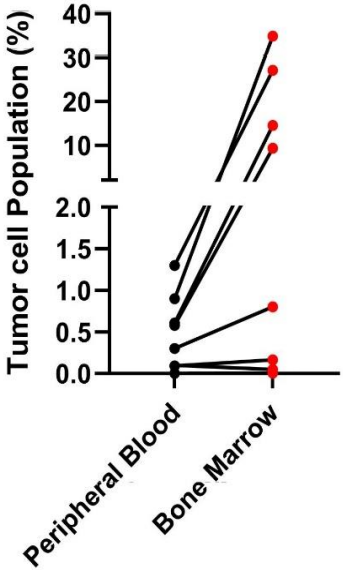
Tumor cell Population (%)
40
30
20
10
2.0
1.5
1.0
0.5
0.0
Peripheral Blood
Bone Marrow

E)

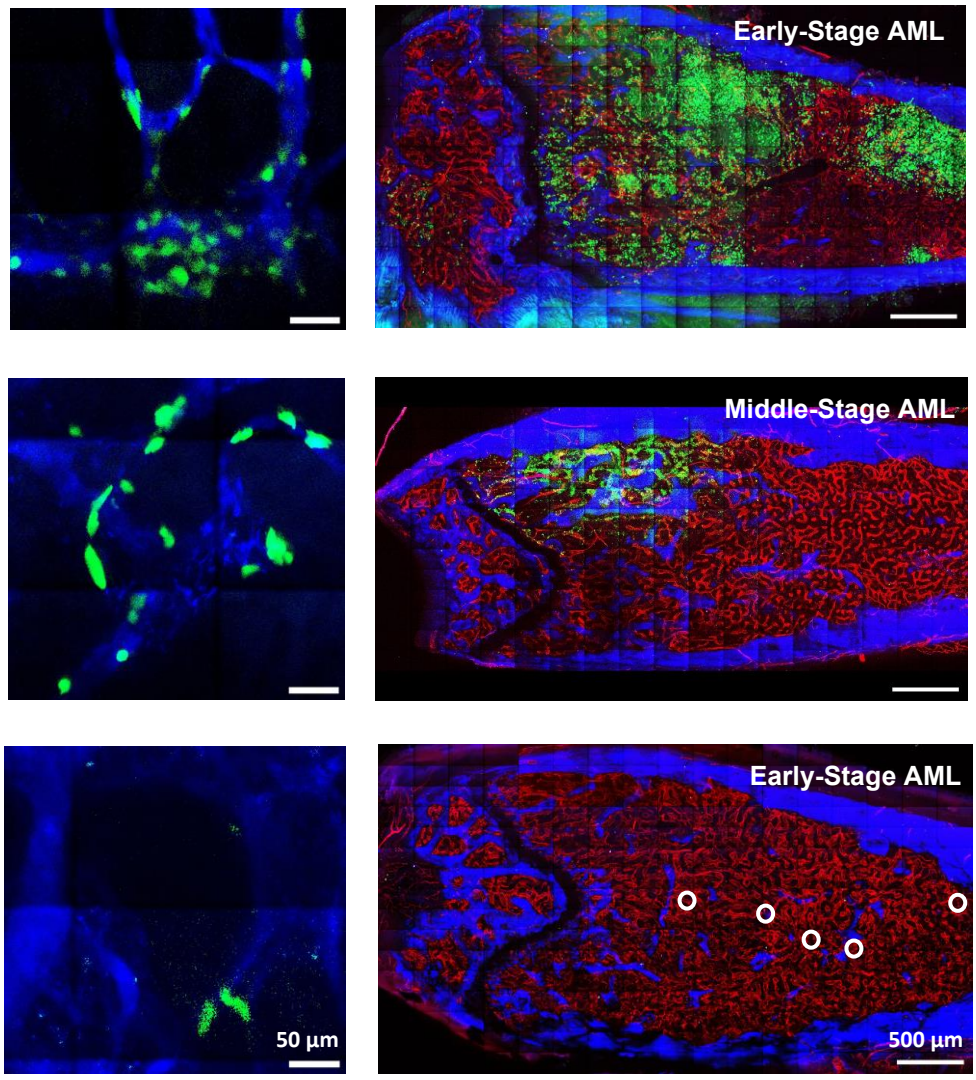

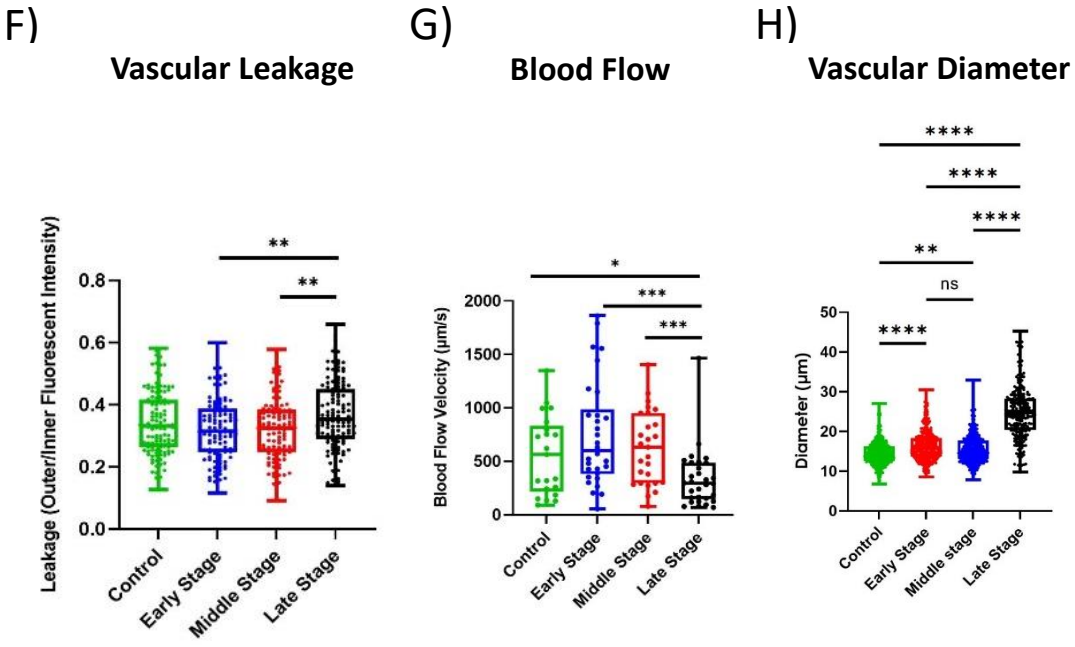

Figure 3.1. AML Progression Alters Vascular Morphology and Function. A) Schematic of retro-orbital injection (left) and representative image (right) of tumor cells in BM after transplantation; Blue: Blood vessel, Green: AML e-GFP+ tumor cells; **B)** Schematic of modified Tail vein injection (left) and representative image (right) of tumor cells in BM after transplantation; **C)** Kaplan–Meier plot showing survival of C1498 AML-injected mice; **D)** Flow cytometry quantification of tumor cell chimerism in PB and BM across AML progression; **E)** Representative images of the tumor-transplanted BM (left: Calvarium, right: long bone) across different stages; Calvarium: Blue: Blood vessel; Green: AML tumor cells; Long bone; Red: blood vessel, Blue: Bone (SHG), Green: AML e-GFP+ cells; White circles represent single tumor cells; **F-H)** Quantification of calvaria BM vascular leakage **(F)**, blood flow velocity **(G)**, and long bone BM vascular diameter **(H)** in control (sublethal irradiation only) and AML-transplanted mice across different stages; *p < 0.05, **p < 0.01,***p < 0.001; ****p < 0.0001.

The AML Cells Distribution in the Long Bone BM Changes across Disease Progression. Assessment of long bone BM across various AML stages has uncovered a distinct preference for tumor cell distribution in the metaphysis and potentially the diaphysis compared to the epiphysis **(Fig. 3.1e)**. To ensure that tumor distribution is not preferential to one side of the body, we imaged long bones of both the right and left femurs **(Fig. 3.2a)**. After observing consistent distribution patterns in both legs, BM chimerism analysis was conducted on AML mice to validate the observations. In contrast to the BM images, chimerism results from epiphyseal and metaphyseal BM indicated no statistically significant difference between the two regions **(Fig. 3.2b, c)**. However, since samples were collected from different stages of AML **(Fig. 3.d)**, to further assess the tumor homing, they were specifically examined at each distinct stage. Chimerism analysis revealed a higher metaphysis-to-epiphysis tumor cell ratio at the early stage, which approaches the same level of AML infiltration as the disease progresses to the advanced stage **(Fig. 3.2d, e)**. AML stages were defined based on PB chimerism results in **Fig 3.1.**

A)

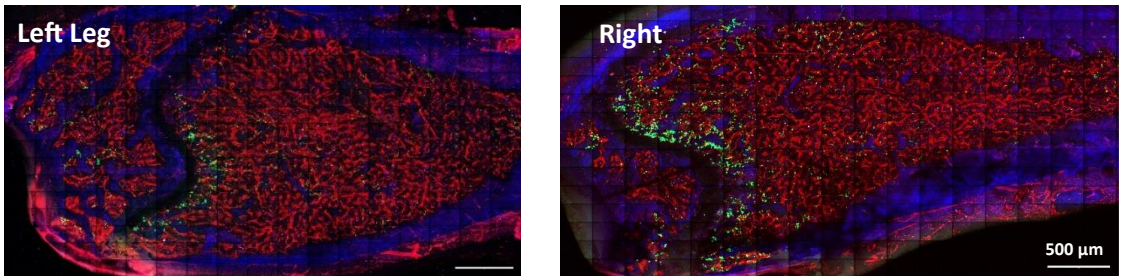
Left Leg
Right
500 µm

B)

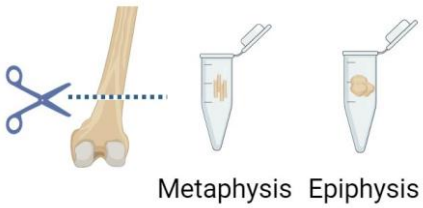
Metaphysis
Epiphysis

C)

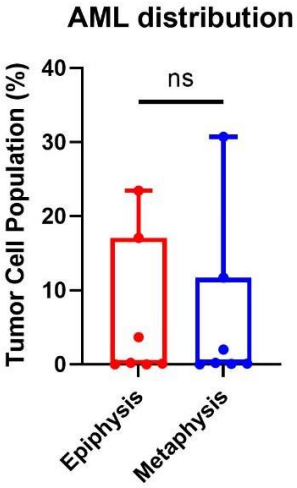
AML distribution
Tumor Cell Population (%)
40
30
20
10
0
ns
Epiphysis
Metaphysis

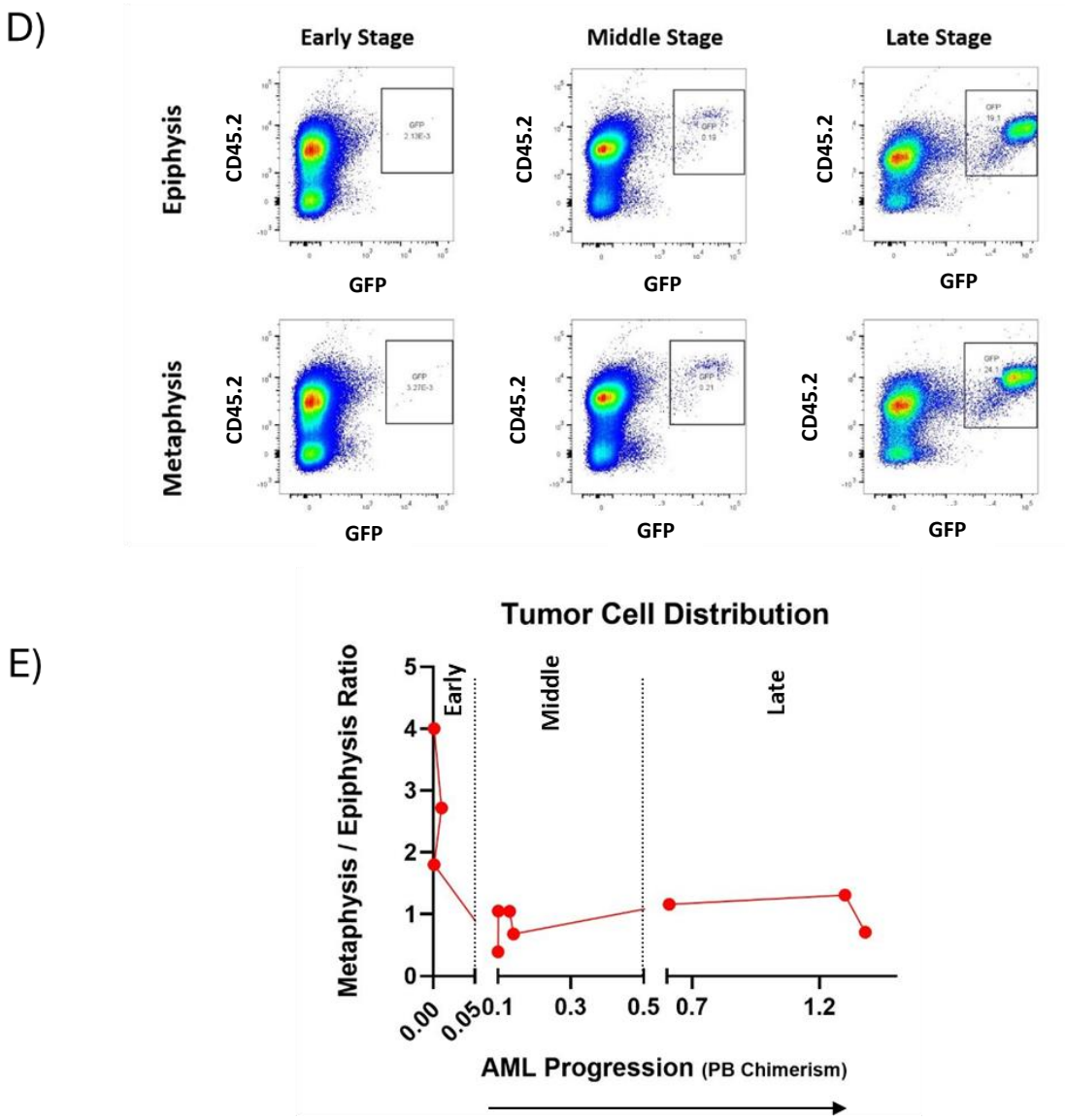

Figure 3.2. The AML Cells Distribution in the Long Bone BM Changes across Disease Progression. A) Representative images of the tumor-transplanted BM in the left and right femurs; Red: blood vessel, Blue: Bone (SHG), Green: AML e-GFP+ cells; **B-C)** Schematic **(B)** and Flow cytometry chimerism **(C)** of epiphyseal and metaphyseal BM in AML-transplanted mice; **D)** Representative flow cytometry chimerism plots of epiphyseal and metaphyseal BM across different stages of AML; **E)** Metaphysis-to-epiphysis tumor cell ratio across early, middle, and late stages of AML separated by dash line.

Modelling Cytotoxic Conditioning in AML Mice; Determining a Suitable Chemotherapy Protocol. Due to the aggressive growth of C1498 cells, particularly when it progresses to the late stage **(Fig. 3.1e-h)**, a timepoint between the early and middle stages was chosen to initiate chemotherapy and HCT. Initially, to apply our findings regarding the effect of BU on the BM niche (chapter 2) to the AML mouse model, conditioning was

administered through single therapy with BU. However, this protocol did not lead to an effective therapeutic outcome and in some instances, even worsened the AML progression **(Fig. 3.3a)**. Prompted by our initial observations, cyclophosphamide (CY), a chemotherapy agent used clinically to treat AML patients, was incorporated into the treatment plan. To assess BU and BU/CY therapeutical function, donor cell engraftment (GFP+ cells), immune cell distribution during recovery (day 42 post transplantation) and T_{reg} population that can indicate GVHD were analyzed through flow cytometry in wild-type B6 mice. More donor cell engraftment after transplantation of UBC-GFP donor cells was observed in wild-type BU/CY treated mice compared to BU alone supporting better therapeutic potential of BU/CY **(Fig. 3.3b, c)**. Additionally, analysis of the T_{reg} population and GVHD score over time showed similar levels to the control, suggesting appropriate dosage and type of chemotherapy agent chosen to treat the AML mouse model **(Fig. 3.3d)**. As mentioned previously, animals were scored for five GVHD clinical parameters on a scale from 0 to 2 to assess the severity of GVHD symptoms. Each score corresponds to a level of sickness, with higher scores indicating more severe GVHD **(Fig. 3.3e)**. In our study, since all the groups appeared healthy without any visible symptoms, they all received a score of 0 during 42 days of study time (Data not shown). After cytotoxic conditioning and HCT, the goal is to restore the recipient's immune system with donor-derived cells. Monitoring the distribution of immune cell population helps assess the success of immune reconstitution. Our data showed that cell lineage distribution of BU/CY conditioned mice was comparable to that of BU treated in both BM and PB suggesting suitable chemotherapy protocols **(Fig. 3.3f, g).**

A)

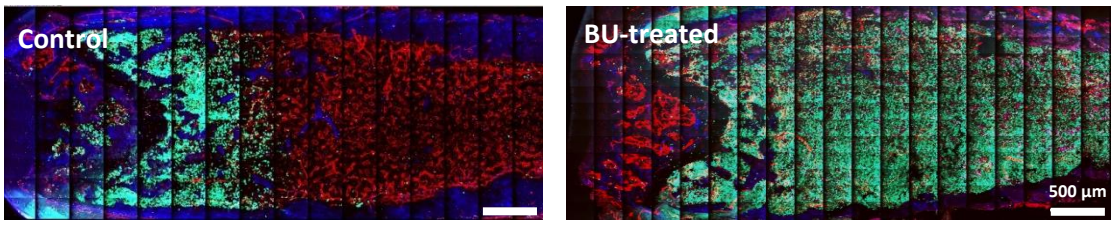

B)

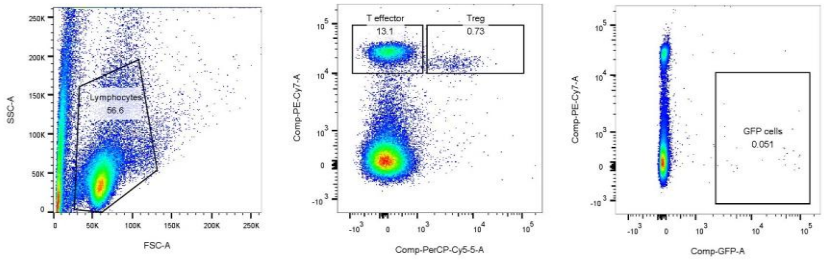

Donor Cells **Treg Population**

C)

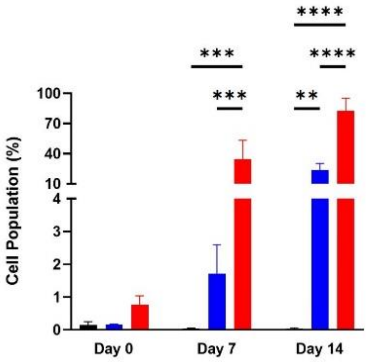

D)

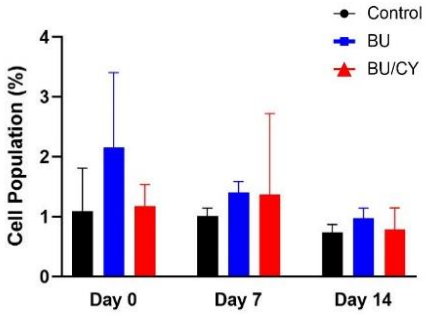

E)

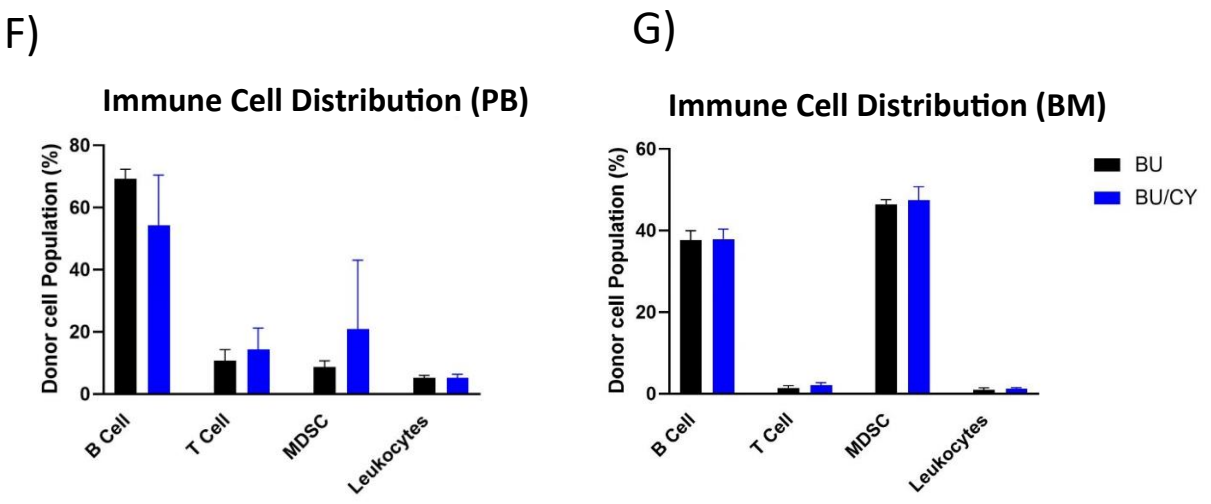

Figure 3.3. Comparison of BU Versus BU/CY Combination Efficacy as the Potential Chemotherapy Drugs for AML. A) Representative images of the long bone BM in control and BU treated mice; Red: blood vessel, Blue: Bone (SHG), Green: AML e-GFP+ cells; **B-D)** Representative PB flow cytometry plots **(B)** and quantification of Donor cell (GFP+) **(C)** and T_{reg} **(D)** populations in control, BU, and BU/CY overtime; **E)** Representative images of the normal (left) and potentially GVHD (posture) impacted (right) animals; **F, G)** Immune cell distribution on day 42 post-HCT in BU or BU/CY conditioning in PB **(F)** and BM **(G)**; n=3, error bar: SD, *p < 0.05, **p < 0.01,***p < 0.001; ****p < 0.0001.

The BM Niche Surrounding Residual AML Cells Facilitates Chemotherapy Resistance. Given our observations indicating the limited efficacy of busulfan and after conducting assessments to evaluate the therapy's efficacy of BU/CY combination, we opted to employ the new protocol to condition AML transplanted animals. Timepoints between early to middle stage of disease were selected to initiate the chemotherapy treatment. Following BU/CY combination therapy, mice were transplanted with whole BM cells from mTmG transgenic mice. The BM microenvironment was evaluated on day 2 post-transplantation through 2P intravital microscopy and flow cytometry chimerism to evaluate the tumor cell population **(Fig. 3.4a)**. Comparable chimeric results before and after conditioning indicated that BU/CY therapy slows down AML progression **(Fig. 3.4b)**. Residual tumor cells preferentially localized to the endosteal niche, primarily in the metaphysis **(Fig. 3.4c)**. Calvarium BM exhibited fewer residual AML populations after treatment compared to the BM in the long bone **(Fig. 3.4d, e)**. The blood vessel network around surviving AML cells appeared to be severely morphologically disrupted compared to other regions of the BM showing no or very few residual tumor cells **(Fig. 3.4f)**. Vascular analysis adjacent to resistant tumor cells showed higher vascular leakage but comparable blood flow velocity compared to other regions of the calvarial BM **(Fig. 3.4g, h)**. This suggests that while the blood vessel network in the long bone is significantly disrupted, the integrity of ECs in the majority of calvarium areas has been preserved. Consistent with other literatures, cell size analysis demonstrated larger resistant tumor cells compared to normal tumor cells[195] **(Fig. 3.4i)**.

A)

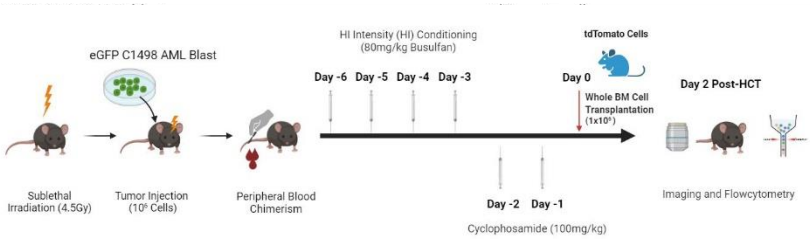
eGFP C1498 AML Blast
HI Intensity (HI) Conditioning
(80mg/kg Busulfan)
Day -6 Day -5 Day -4 Day -3
tdTomato Cells
Day 0
Whole BM Cell
Transplantation
(1x10⁶)
Day 2 Post-HCT
Sublethal
Irradiation (4.5Gy)
Tumor Injection
(10⁶ Cells)
Peripheral Blood
Chimerism
Day -2 Day -1
Cyclophosamide (100mg/kg)
Imaging and Flowcytometry

B)

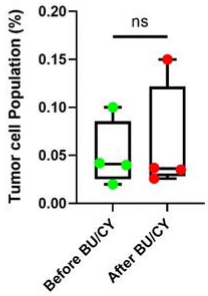
ns
Tumor cell Population (%)
0.20
0.15
0.10
0.05
0.00
Before BU/CY
After BU/CY

C)

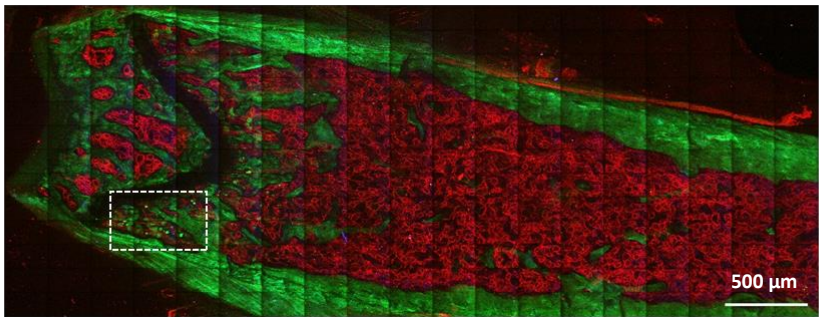
500 µm

D)

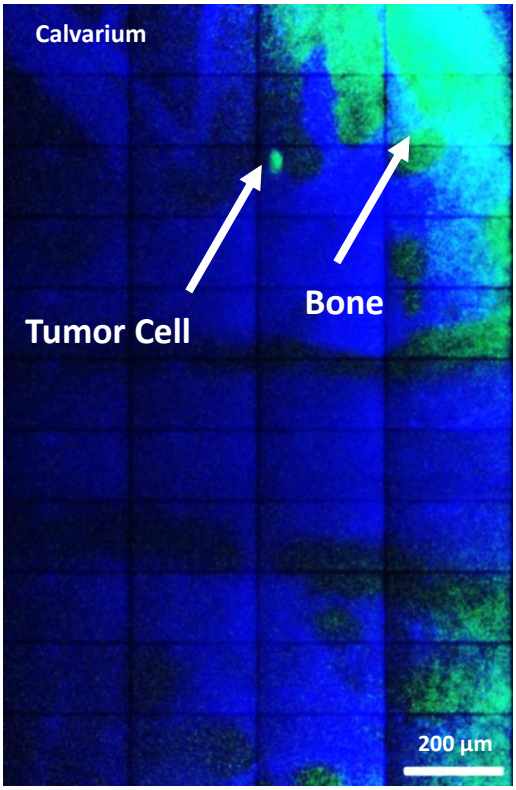
Calvarium
Tumor Cell
Bone
200 µm

E)

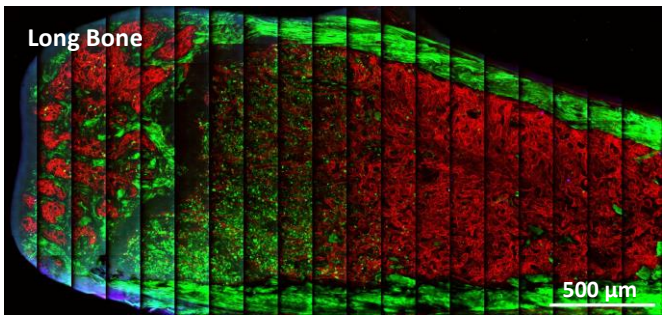
Long Bone
500 µm

F)

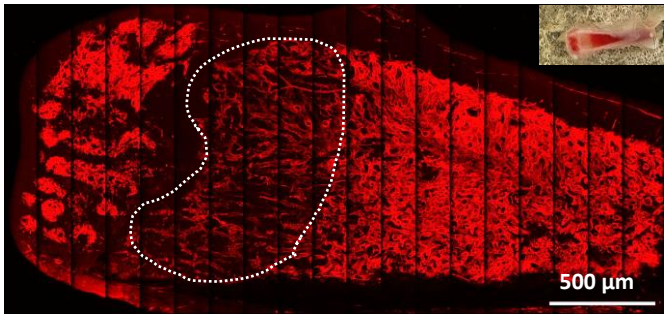
500 µm

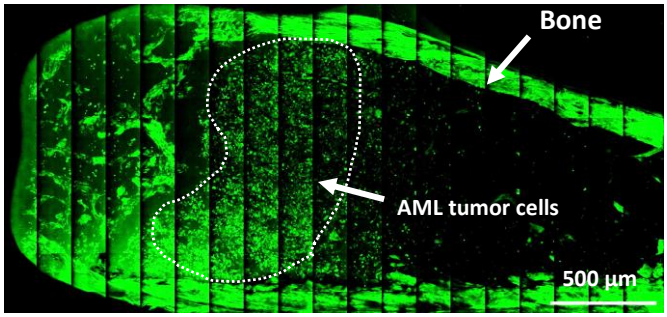
Bone
AML tumor cells
500 µm

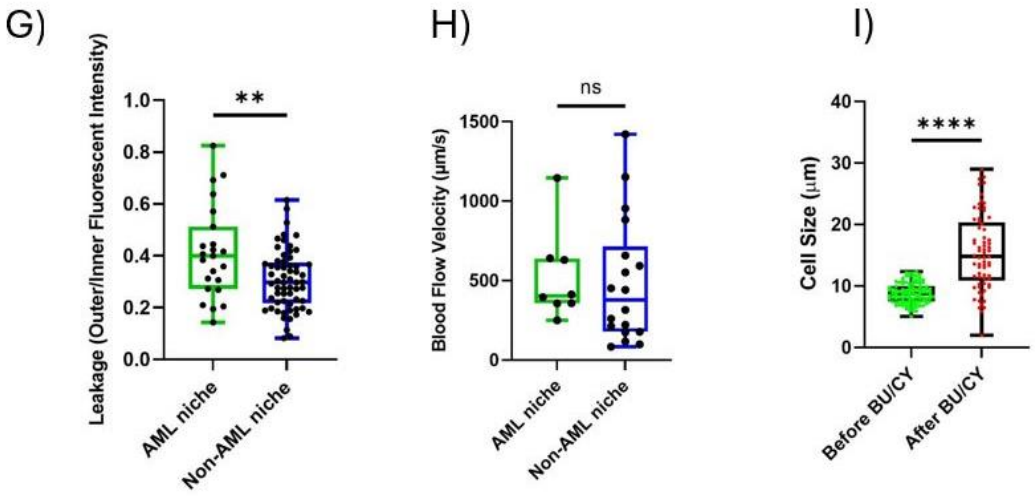

Figure 3.4. The BM Niche Surrounding Residual AML Cells Facilitates Chemotherapy Resistance. A) Schematic of chemotherapy treatment in AML-transplanted mouse model; **B)** Quantification of tumor cells in PB before and after BU/CY treatment; **C)** Representative image of the residual AML cells localization within long bone BM after BU/CY treatment; **D, E)** Representative images of the calvarial **(D)** and long bone BM **(E)** after BU/CY treatment; **F)** Representative image of the vascular network around residual AML cells (Top; Red channel representing vascular network, Bottom; Green channel representing tumors cells) **G, H)** Quantification of calvaria BM vascular leakage **(G)** and blood flow **(H)** at BM niche surrounding resistant tumor cells; **I)** Quantification of the cell size of the primary and residual AML cells; Long bones; Red: blood vessel, Green: Bone (SHG) and AML e-GFP +cells; Calvarium; Blue: blood vessel, Green: Bone (SHG) and AML e-GFP+ cells; $^{**}p < 0.01$, $^{****}p < 0.0001$.

DISCUSSION

In this report, using 2P intravital microscopy we demonstrated how AML disease progresses in the BM and gradually reshapes the stem cell niche, particularly vascular system, across different stages of the disease. In our study, we used peripheral blood AML population to categorize the progression of the disease. We conducted BM chimerism analysis to evaluate the disease progression in the BM through flow cytometry in addition to the PB chimerism and 2P intravital BM images. Given that AML is a BM-associated cancer, tumor cells preferentially migrate into the BM rather than remaining in the PB supporting higher infiltration of the BM with AML cells compared to the PB in the later stages of disease.

Consistent with other studies, we showed localization of the tumor cells in the endosteum and preferentially metaphysis[196]. This could be due to a variety of factors such as protection from therapy, cell adhesion modules or relatively hypoxia that can promote the survival and self-renewal of leukemia stem cells, resulting in the treatment resistance[42,197]. Expansion of tumor cells in the metaphysis severely disrupts the vascular network in this region while the central BM appears to be less impacted[184]. This leads to the transforming BM niches in favor of leukemia microenvironments and surviving of leukemia cells in this area following chemotherapy conditioning.

To explore the relevance of these findings in a human context, Duarte et al. besides *in vivo* studies, conducted supplementary histological examinations of BM trephine biopsies from AML patients exhibiting over 80% infiltration in endosteal vessels, validating our observations on the reduction vessels in this region[184].

In addition, quiescent characteristics of the endosteum facilitate transferring primary tumor cells to a senesce-like state that has been shown to be induced by chemotherapy treatment[195]. Duy et al. demonstrated an increase in granules and the size of tumor cells in senescent-like residual tumor cells following treatment with the Ara-C chemotherapy agent[195]. The difference in tumor cell size before and after BU/CY chemotherapy was consistent with the findings of that study. Furthermore, Kim et al. elucidated the enlargement of residual cells through endocycling, which occurs when residual tumor cells, following therapy, undergo incomplete cell division by deviating from the conventional cell cycle and advancing through multiple rounds of growth and DNA replication[198].

BM chimerism results indicated higher accumulation of tumor cells in the metaphysis at early stages that turns to the same level while the disease progresses to the late stage. This could be due to the highly metabolically active nature of metaphysis making a favorable microenvironment for proliferative AML cells. Cell-cycle evaluation of HSPCs and HSCs has shown that in epiphysis compared to the metaphysis, more stem cells are in G0 state indicating that epiphyseal HSCs are relatively dormant[199].Difference in the amount of available BM space, vascular system, and supporting factors required for the tumor maintenance are of the other potential factors contributing to the preferential localization of the tumor cells. However, with increased tumor burden, it can invade nearby tissues, including the epiphysis.

Assessment of the calvaria and long bone BM post-conditioning indicates that chemotherapy agents may have varied effects on AML cells based on their localization within the BM. While higher vascular leakage was observed adjacent to the resistant tumor cells, leakage in other regions was comparable to the control, early, and middle stages before treatment (Data not shown). This indicates that unlike the significantly disrupted vessel network in the long bone, the integrity of ECs in most areas of calvarium has remained normal. Itkin et al. showed that endothelial barrier disruption results in a significant reduction in the numbers of BM stem cells and increased ROS[131]. Therefore, besides ineffective delivery of chemotherapy drug to the tumor cells, change in the stem cells population and ROS level could contribute to the more optimized niche for tumor cells decreasing the efficacy of chemotherapy treatment in the long bone BM.

Overall, in line with other studies, our data show that chemo-resistant AML cells are found primarily in the metaphyseal BM where they home during the disease progression[184,196]. Having observed severe disruption of the blood vessels in this region, our findings suggest that promoting vascular recovery in the metaphysis can potentially result in more effective chemotherapy outcomes. Elimination of tumor cells after treatment in the calvaria BM that showed a better vascular integrity compared to the long bone supports our proposal.

CONCLUSION

Based on the findings presented, it is evident that AML progression profoundly impacts vascular morphology and function, influencing the behavior of tumor cells within the BM microenvironment. Categorizing AML progression into early, middle, and late stages enabled a better understanding of disease dynamics before initiating cytotoxic conditioning. Notably, the distribution of tumor cells within the BM exhibited preferences for the metaphysis and potentially the diaphysis especially at early stage, highlighting the importance of spatial considerations in disease characterization. Upon modeling cytotoxic conditioning, it was observed that a combination therapy involving BU/CY demonstrated superior therapeutic potential compared to single-agent BU therapy. This was evidenced by enhanced donor cell engraftment in wild-type mice and comparable PB chimerism before and after BU/CY treatment in AML mouse model. Furthermore, evaluating the BM niche surrounding residual AML cells following BU/CY therapy revealed the preferential localization of tumor cells to the endosteal niche, accompanied by significant alterations in vascular morphology and function. These observations highlight the interplay between the BM microenvironment and AML progression, potentially contributing to chemotherapy resistance and disease relapse.

In conclusion, the comprehensive characterization of AML progression and therapeutic responses in our AML mouse model provides valuable insights into the reciprocal interaction of AML tumor cells and BM microenvironment, stem cell niche surrounding residual AML cells, and potential of combination therapies in improving treatment outcomes.

Unpublished Findings

Ex Vivo Imaging of Cleared AML Long Bone and Thymus

BACKGROUND

In this project, our main goal was to investigate the BM microenvironment in an AML mouse model, both pre- and post-chemotherapy treatment. We aimed to gain understanding of the alterations occurring in the BM niche during AML progression before chemotherapy, and to determine whether changes induced by tumor cells or cytotoxic conditioning contribute to tumor survival. As previously mentioned, our imaging approach involved using a cryostat to remove the cortical layer of the bone, allowing us to image the BM. However, this method has limitations, as it only enables imaging up to a depth of 150-200 μm, which may not adequately represent the entire bone and BM while its thickness exceeds 1 mm. For our AML project, this limitation becomes critical after chemotherapy treatment when residual tumor cells may be present in deeper layers of the BM, beyond the imaging surface plane. In addition, the removal of bone and part of BM during cryosectioning may cause missing some crucial information and disrupt the architectural integrity of the long bone BM. To address these challenges, we sought alternative methods that could make the biological tissues more transparent by changing the refractive index impacting light scattering, penetration depth, and overall image quality during microscopy imaging.

MATERIAL AND METHOD

uDISCO (ultimate 3D imaging of solvent-cleared organs) is a tissue clearing protocol specifically designed to enhance tissue transparency while preserving endogenous fluorophores and fluorescent proteins. To conduct uDISCO clearing, vascular antibodies including CD31, CD144, and Sca-1 conjugated with Alexaflour647 were injected 30 min before intracardiac perfusion. After perfusion, the dissected long bone and thymus were fixed in 4% PFA overnight at 4°C. They were then dehydrated using tert-butanol (Sigma-Aldrich; SHBM5332) at various starting from 30% concentrations followed by 50%, 70%, 90%, and 100%. After dehydration, tissues were transferred into dichloromethane (DCM; Sigma-Aldrich, SHBJ8352) for delipidation. Subsequently, they were immersed in a solution of BABB-D4, composed of a mixture of benzyl alcohol (Sigma-Aldrich; 24122) and benzyl benzoate (Sigma-Aldrich; W213802) in a 1:2 ratio, combined with diphenyl ether (DPE; Alfa Aesar, A15791)) at a 4:1 ratio, and supplemented with 0.4% DL- α -tocopherol (Vitamin E; Alfa Aesar, A17039). Long bone and Thymus were mounted on the slide, and they were kept at 4°C throughout the imaging session.

RESULTS

With the uDISCO technique, we achieved remarkable results, allowing us to image intact long bones to a depth of more than 600 µm (**Fig. 3.5**). This extended imaging depth provided us with a more comprehensive view of the BM microenvironment, particularly after chemotherapy, where deeper visualization is crucial for detecting residual tumor cells that may not be accessible through traditional imaging methods.

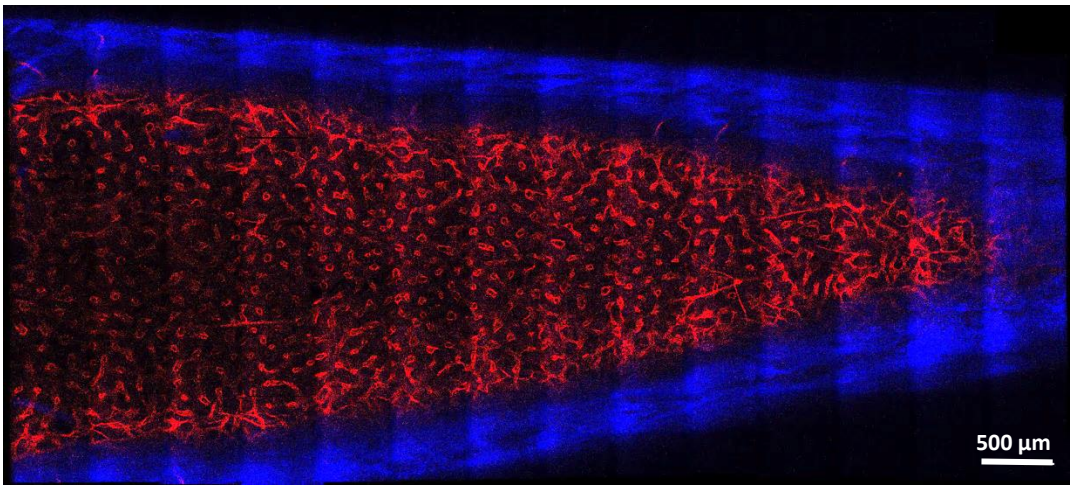

Figure 3.5. Representative Long Bone Imaging After uDISCO Clearing. Red: Blood vessels; Blue: Bone. (Chicana, B., Abbasizadeh. N, 2022).

After conducting a preliminary assessment of the uDISCO protocol on the AML mouse model, we confirmed its compatibility with e-GFP-conjugated tumor cells **(Fig. 3.6)**. This finding suggests that uDISCO could serve as a valuable alternative in situations where cryosectioning of the bone fails to provide the desired information.

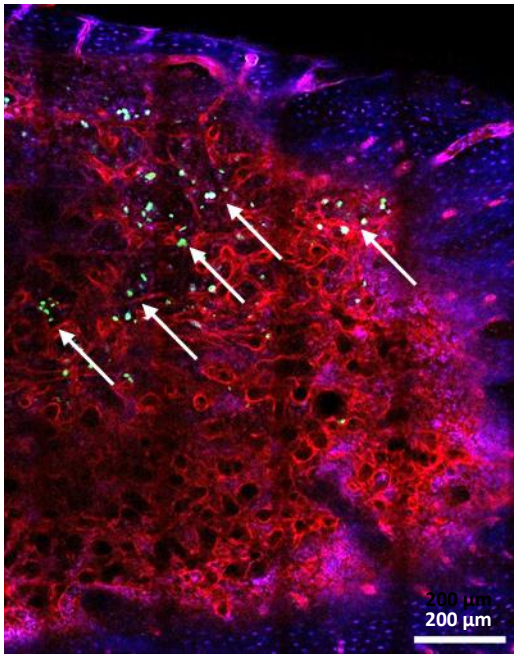

Figure 3.6. Representative Long Bone Imaging with AML GFP+ Tumor Cells After uDISCO Clearing. Red: Blood vessels; Green: e-GFP+ AML tumor cells, Blue: Bone.

Besides long bones, I used this protocol to image the thymus of AML mice **(Fig. 3.7)**. Understanding how AML cells may infiltrate the thymus and influence its morphological and functional characteristics could provide valuable insights into the broader impact of AML on the immune system. Furthermore, it is intriguing to explore whether the AML cells homing in the thymus originate directly from the primary injected tumor cells or if they are a result of expansion in the BM followed by cell trafficking between the BM and thymus. Investigating these aspects could enhance our understanding of AML kinetics and its effects on immune function alongside the BM microenvironment. Considering the association of BM and thymus as two crucial hematopoietic immune tissues, the possibility of AML tumor cells homing to the thymus and their potential interactions with thymic immune cells was of interest to investigate. In our preliminary images, GFP+ AML tumor cells were observed in the thymus, indicating their migration to this tissue in addition to the bone marrow, spleen, ovary, liver, and lungs, which are recognized as primary organs affected by C1498 cell AML disease. Future studies could investigate deeper into understanding the interplay between AML and the thymus, exploring aspects such as the impact of tumor cells on thymus architecture and function, as well as the interactions between AML cells and thymic immune cells.

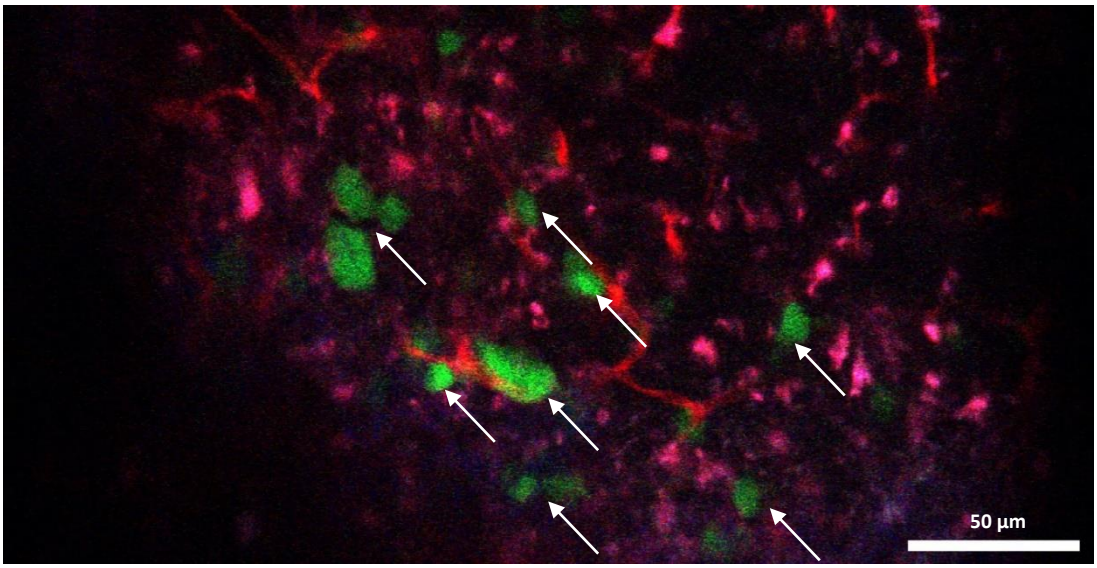

Figure 3.7. *Ex Vivo* Imaging of uDISCO Cleared Thymus in the AML Mouse Model. Red: Blood vessels; Green: GFP+ AML tumor cells indicated with arrow points.

CHAPTER 4

Contribution and Future Direction

Contributions to the Field

In the investigation of BM microenvironment various techniques have been employed, each offering unique insights into cellular and molecular characteristics within the stem cell niche. Traditional methods such as flow cytometry and single-cell RNA sequencing have enabled researchers to get insight into the composition and gene expression profiles of BM cell populations. However, these approaches cannot provide information regarding the dynamic interplay between cells and their microenvironment in real-time. 2P Intravital microscopy offers the distinct advantage of directly visualizing spatial characteristics of the BM niche with high resolution and in live animals. During my project, our custom-built 2P intravital microscopy enabled the exploration of dynamic features within the BM microenvironment, including assessments of vascular leakage, permeability, and blood flow velocity. We were also able to visualize the expansion and behavior of tumor cells in AML models, providing valuable information about their interaction with the BM niche. Furthermore, compared to the single photon microscopy techniques like confocal imaging, 2P microscopy provides higher imaging depth and minimizes photodamage to live animals. This is attributed to the infrared (IR) wavelengths used in this technique which fall within the optical window of biological tissues. This is beneficial to conduct longitudinal studies and dynamic observations in physiological and pathological contexts with minimal perturbation. Exploiting advantages of 2P intravital microscopy, I was able to generate qualitative and quantitative findings in the context of BM microenvironment aiming to:

Investigate Changes to the BM Microenvironment as a Function of Cytotoxic Conditioning Intensity and Recipient Age.

HCT is an essential therapeutic approach for patients suffering from hematologic malignancies or non-malignant diseases. However, Pre-transplant preparative regimens required for HCT can adversely affect the BM microenvironment. The specific impacts of cytotoxic preconditioning on bone and BM niche over time are not yet fully understood. Furthermore, the influence of recipient age and the dosage of cytotoxic agents has not been comprehensively elucidated.

In this dissertation, we reported microenvironmental changes within the BM following LI and HI cytotoxic conditioning, considering the age of the animal model. Our results revealed significant differences in hematopoietic recovery between LI and HI conditioned mice, with greater donor cell engraftment observed in the HI group across both young and adult cohorts. *Ex vivo* imaging of BM in long bones demonstrated accelerated vascular recovery in young mice compared to adults, based on morphological assessments. Furthermore, prolonged disruption in endothelial cell integrity following busulfan conditioning, despite hematopoietic recovery over time, was evident through vascular leakage outcomes. Bone turnover studies indicated prominent alterations in bone architecture by day 42 post-HCT in both young and adult mice.

Evaluate BM Niche Around Resistant Tumor Cells After Cytotoxic Conditioning in AML Mouse Model.

Hematopoiesis relies on interactions between HSCs and the BM microenvironment. However, disruptions to this finely regulated system can lead to malignant transformation, as seen in hematopoietic diseases like AML. A major challenge in AML treatment lies in disease relapse post-cytotoxic therapy, significantly impacting patient outcomes. Previous studies have implicated the disruption of BM niches during therapeutic regimens or disease expansion as a key factors contributing to this phenomenon.

In this study, we established an AML mouse model and demonstrated progression AML disease in the BM and how it gradually will be remodeling the stem cell niche including vascular system, across early, middle, and late stages of the disease. The application of BU/CY showed promising results in slowing down the AML progression. BM niche evaluation around AML cells indicated localization of the tumor cells in the metaphysis, higher leakage, and severe disruption of the blood vessel in regions surrounding tumor cells, differential response of calvaria and long bone BM to the chemotherapy and increase in the size of survived tumor cells compared to the primary AML cells.

In summary, this dissertation, by investigating the influence of chemotherapy dosage and recipient age on treatment response, aimed to improve chemotherapy regimens and offer the foundation for personalized treatment strategies. Understanding the mechanisms underlying AML survival following chemotherapy could inform the development of novel therapeutic approaches to overcome resistance and improve patient prognosis. Through the characterization of the BM niche surrounding residual AML tumor cells using intravital microscopy, this research provided direct observation of factors potentially contributing to disease survival—a significant clinical challenge for AML patients.

Future Direction

Investigation of the Role of Immune Cells in Promoting the Faster Recovery of Vascular Endothelial Cells Following Cytotoxic Conditioning.

Our findings showed that surprisingly, even after 6 weeks post-HCT, vascular ECs remain disrupted, causing leakage. Since blood vessel integrity plays an important role in more efficient hematopoietic recovery, exploring how immune cells, such as regulatory T cells or macrophages, could potentially improve vascular recovery will be of interest to investigate. While much of the focus on regulatory T cells has been on their immunomodulatory functions, emerging evidence suggests that they also contribute to tissue repair or angiogenesis regulation, including in the BM microenvironment[200,201]. Macrophages also play a crucial role in BM vascular recovery following cytotoxic therapy through different mechanisms such as inflammation resolution or promoting angiogenesis. Exploring the function of these or other effective immune cells specifically on the vascular leakage recovery requires further experimentation.

Investigation of the Extent of Vascular and Skeletal Niche Contribution to Hematopoietic Recovery.

Our observations indicated that despite long-lasting changes in some aspects of the vascular system and bone architecture following cytotoxic conditioning, hematopoietic recovery can still occur. Specifically, bone remodeling analysis showed more significant bone resorption on day 42, selected as the hematopoietic recovery timepoint, compared to the early time points (Days 2 and 5). Long-lasting leakage and vascular morphology alteration on day 42 are of other changes raising the question about the extent of BM niche contribution to the hematopoietic reconstitution. Further exploration of factors such as extramedullary hematopoiesis, that refers to the production of blood cells outside the BM would enhance our knowledge of interplay between the BM microenvironment and hematopoietic reconstitution. *Ex vivo* imaging of spleen and liver or flow cytometry chimerism of donor cells in these organs could demonstrate the extent of extramedullary hematopoiesis to the HSC reconstitution despite BM disruption.

Investigation of the Function of Cytotoxic Conditioning Intensity for BU/CY Combination.

In the first phase of my project, we evaluated changes to the BM niche as a function of preparative conditioning intensity using BU treatment. We aimed to use our findings to the second phase in which we apply the most suitable treatment protocol on an AML mouse model. However, since the single therapy plan with BU didn't exhibit effective treatment outcomes, we incorporated cyclophosphamide into the protocol. Therefore, to achieve our

primary goal, the assessment of BM microenvironment following different concentrations of BU/CY will provide better insight into the most optimal treatment plan in terms of the chemotherapy drug dosage for cancer patients with different ages.

Investigation of Differences Between Calvarium and Long Bone BM Supporting their Distinct Response to Chemotherapy Treatment.

In the AML mouse model, BM images showed different responses of the calvaria and long bone BM niches to chemotherapy administration with BU/CY. This difference was contributed to the vascular integrity and the number of residual AML cells. Identifying distinct characterizations of calvaria and long bone BM and exploring contributing factors in the calvarium that facilitate tumor remission could provide a better understanding of conditions that promote an effective chemotherapy response. Z. I. Kolabas et al. recently reported distinct transcriptional signature of cell types in all the bone types including calvarium and femur[202,203]. Given the intricate interaction between leukemic cells and various BM cell types, evaluating the cell lineage populations and their distribution in each BM tissue in an AML model could offer insights into potential mechanisms underlying calvarium and long bone response to the drug. Differences in the vessel types and their density, perivascular niche and signaling molecules are of other elements that could be examined to provide supporting explanation in this regard.

Investigation of Spatial Interaction of AML Tumor Cells and CD8+ T Cells in Thymus Using Two-Photon Intravital Microscopy

Our initial imaging in the AML mouse model revealed a noticeable presence of tumor cells in the uDISCO-cleared thymus. Considering the key role of the thymus in sustaining T-cell immunity, a potential decrease in its functionality might compromise the efficacy of T-cell-targeted immunotherapies in AML. Considering our labeartory expertise in 2P intravital microscopy and thymus study as one of our primary research focus, investigating the hemodynamics and vascular system of the thymus through *in vivo* and *ex vivo* imaging in an AML mouse model could expand our understanding of how leukemic tumor cells impact the thymus, alongside the BM, as two integral components of the immune system.

Moreover, previous studies have demonstrated that T cells, especially cytotoxic CD8+ T cells, can recognize leukemia-specific antigens displayed on the surface of AML cells, leading to their destruction[204]. However, due to reciprocal interaction, AML cells can also impede the function of CD8+ T cells through various mechanisms[205]. Therefore, investigating the alteration in the CD8+ T cells population and their spatial distribution relative to the AML cells in the thymus could further validate the communication between tumor cells and CD8+ T cells.

Investigation of BM Oxygenation in Wild-Type and AML Mouse Models Using 2PLM. As mentioned in Chapter 2, compared to other oxygen sensing techniques, 2PLM system offers high spatial and temporal resolution for pO_2 quantification. Throughout my research, I contributed to the technical design and execution of the groundwork for pO_2 calibration. Following our findings on changes to the BM niche upon cytotoxic conditioning, measurement of the BM oxygenation over time and in response to the dosage and age variables is of interest to study. This will enhance our understanding of how different conditioning regimens impact BM oxygen levels. Moreover, measuring pO2 in proximity to residual AML cells post-treatment is critical, as it influences tumor cell survival and resistance mechanisms. Considering established setups for *in vivo* and *in vitro* pO_2 calibration, oxygen sensing via 2PLM could be defined as a promising follow-up project.

Investigation of BM Niche in more Human Relevant AML Mouse Model. While the B6 mouse model with sublethal irradiation and injection of the C1498 AML cell line can provide valuable insights into certain aspects of AML, other mouse models may be more relevant to human AML due to differences in genetic background, immune system, and disease progression. Genetically engineered mouse models such as those with mutations in genes relevant to AML (like FLT3-ITD) can better mimic specific genetic alterations found in human AML and provide insights into disease pathogenesis and therapeutic responses. Patient-Derived Xenograft (PDX) models that involve the transplantation of primary human AML cells or patient-derived leukemic stem cells into mice are of other alternative mouse models to evaluate the BM niche before and after BU/CY conditioning.

Summary

The recovery of hematopoietic and immune systems following cytotoxic cancer therapies has been evident as a significant clinical challenge for many patients. Understanding how the bone marrow niche alters after cytotoxic conditioning is crucial for overcoming this challenge and could offer valuable insights for the development of more effective treatments. This dissertation reveals changes to the mouse bone marrow microenvironment following chemotherapy treatment in a comprehensive manner. Using two-photon intravital microscopy and flow cytometry technique we investigated how high and low intensity conditioning of busulfan affects hematopoietic reconstitution and remodeling of the bone and BM vascular network. In addition, we reported the function of recipient age in the BM response after preparative regimens. In the following, we applied busulfan/ cyclophosamide chemotherapy combination, as clinically relevant regime for hematologic malignancies, in an AML mouse model. Using our findings in the first phase of my project, we aimed to understand how or whether bone marrow niche alterations after conditioning or AML progression contribute to the survival and ultimately relapse of the primary disease. This study provides the foundation for better understanding of BM microenvironment after chemotherapy in wild-type and AML mouse models.

REFERENCES

1. Fröbel, J. *et al.* The Hematopoietic Bone Marrow Niche Ecosystem. *Front. Cell Dev. Biol.* **9**, 705410 (2021).

2. Seita, J. & Weissman, I. L. Hematopoietic stem cell: self-renewal versus differentiation. *WIREs Syst. Biol. Med.* **2**, 640–653 (2010).

3. Méndez-Ferrer, S. *et al.* Bone marrow niches in haematological malignancies. *Nat. Rev. Cancer* **20**, 285–298 (2020).

4. Lucas, D. Structural organization of the bone marrow and its role in hematopoiesis. *Curr. Opin. Hematol.* **28**, 36–42 (2021).

5. Kopp, H.-G., Avecilla, S. T., Hooper, A. T. & Rafii, S. The Bone Marrow Vascular Niche: Home of HSC Differentiation and Mobilization. *Physiology* **20**, 349–356 (2005).

6. Clarke, B. Normal Bone Anatomy and Physiology. *Clin. J. Am. Soc. Nephrol.* **3**, S131–S139 (2008).

7. Galán-Díez, M. & Kousteni, S. The Osteoblastic Niche in Hematopoiesis and Hematological Myeloid Malignancies. *Curr. Mol. Biol. Rep.* **3**, 53–62 (2017).

8. Beerman, I., Luis, T. C., Singbrant, S., Lo Celso, C. & Méndez-Ferrer, S. The evolving view of the hematopoietic stem cell niche. *Exp. Hematol.* **50**, 22–26 (2017).

9. Yoshihara, H. *et al.* Thrombopoietin/MPL Signaling Regulates Hematopoietic Stem Cell Quiescence and Interaction with the Osteoblastic Niche. *Cell Stem Cell* **1**, 685–697 (2007).

10. Zhao, M. *et al.* N-Cadherin-Expressing Bone and Marrow Stromal Progenitor Cells Maintain Reserve Hematopoietic Stem Cells. *Cell Rep.* **26**, 652-669.e6 (2019).

11. Pittenger, M. F. *et al.* Multilineage Potential of Adult Human Mesenchymal Stem Cells. *Science* **284**, 143–147 (1999).

12. Batsali, A. K. *et al.* The Role of Bone Marrow Mesenchymal Stem Cell Derived Extracellular Vesicles (MSC-EVs) in Normal and Abnormal Hematopoiesis and Their Therapeutic Potential. *J. Clin. Med.* **9**, 856 (2020).

13. Roboz, G. J. & Guzman, M. Acute myeloid leukemia stem cells: seek and destroy. *Expert Rev. Hematol.* **2**, 663–672 (2009).

14. Morikawa, T. & Takubo, K. Hypoxia regulates the hematopoietic stem cell niche. *Pflüg. Arch. - Eur. J. Physiol.* **468**, 13–22 (2016).

15. Christodoulou, C. *et al.* Live-animal imaging of native haematopoietic stem and progenitor cells. *Nature* **578**, 278–283 (2020).

16. Spencer, J. A. *et al.* Direct measurement of local oxygen concentration in the bone marrow of live animals. *Nature* **508**, 269–273 (2014).

17. Danet, G. H., Pan, Y., Luongo, J. L., Bonnet, D. A. & Simon, M. C. Expansion of human SCID-repopulating cells under hypoxic conditions. *J. Clin. Invest.* **112**, 126–135 (2003).

18. Liu, Y., Cox, S. R., Morita, T. & Kourembanas, S. Hypoxia Regulates Vascular Endothelial Growth Factor Gene Expression in Endothelial Cells: Identification of a 5′ Enhancer. *Circ. Res.* **77**, 638–643 (1995).

19. Ebert, B. L., Firth, J. D. & Ratcliffe, P. J. Hypoxia and Mitochondrial Inhibitors Regulate Expression of Glucose Transporter-1 via Distinct Cis-acting Sequences. *J. Biol. Chem.* **270**, 29083–29089 (1995).

20. Weissman, I. L., Anderson, D. J. & Gage, F. Stem and Progenitor Cells: Origins, Phenotypes, Lineage Commitments, and Transdifferentiations. *Annu. Rev. Cell Dev. Biol.* **17**, 387–403 (2001).

21. Cheng, H., Zheng, Z. & Cheng, T. New paradigms on hematopoietic stem cell differentiation. *Protein Cell* **11**, 34–44 (2020).

22. Adolfsson, J. *et al.* Identification of Flt3+ Lympho-Myeloid Stem Cells Lacking Erythro-Megakaryocytic Potential. *Cell* **121**, 295–306 (2005).

23. Akashi, K., Traver, D., Miyamoto, T. & Weissman, I. L. A clonogenic common myeloid progenitor that gives rise to all myeloid lineages. *Nature* **404**, 193–197 (2000).

24. Kondo, M., Weissman, I. L. & Akashi, K. Identification of Clonogenic Common Lymphoid Progenitors in Mouse Bone Marrow. *Cell* **91**, 661–672 (1997).

25. Zhu, J. *et al.* Osteoblasts support B-lymphocyte commitment and differentiation from hematopoietic stem cells. *Blood* **109**, 3706–3712 (2007).

26. Visnjic, D. *et al.* Hematopoiesis is severely altered in mice with an induced osteoblast deficiency. *Blood* **103**, 3258–3264 (2004).

27. Ding, L. & Morrison, S. J. Haematopoietic stem cells and early lymphoid progenitors occupy distinct bone marrow niches. *Nature* **495**, 231–235 (2013).

28. Poulos, M. G. *et al.* Endothelial Jagged-1 Is Necessary for Homeostatic and Regenerative Hematopoiesis. *Cell Rep.* **4**, 1022–1034 (2013).

29. Calvi, L. M. *et al.* Osteoblastic cells regulate the haematopoietic stem cell niche. *Nature* **425**, 841–846 (2003).

30. Brown, C. M. S., Larsen, S. R., Iland, H. J., Joshua, D. E. & Gibson, J. Leukaemias into the 21st century: part 1: the acute leukaemias. *Intern. Med. J.* **42**, 1179–1186 (2012).

31. Newell, L. F. & Cook, R. J. Advances in acute myeloid leukemia. *BMJ* n2026 (2021) doi:10.1136/bmj.n2026.

32. Marchand, T. & Pinho, S. Leukemic Stem Cells: From Leukemic Niche Biology to Treatment Opportunities. *Front. Immunol.* **12**, 775128 (2021).

33. Marlein, C. R. *et al.* NADPH oxidase-2 derived superoxide drives mitochondrial transfer from bone marrow stromal cells to leukemic blasts. *Blood* **130**, 1649–1660 (2017).

34. Moschoi, R. *et al.* Protective mitochondrial transfer from bone marrow stromal cells to acute myeloid leukemic cells during chemotherapy. *Blood* **128**, 253–264 (2016).

35. Chand, R., Chandra, H., Chandra, S. & Verma, S. K. Role of Microvessel Density and Vascular Endothelial Growth Factor in Angiogenesis of Hematological Malignancies. *Bone Marrow Res.* **2016**, 1–4 (2016).

36. Kampen, K. R., Ter Elst, A. & De Bont, E. S. J. M. Vascular endothelial growth factor signaling in acute myeloid leukemia. *Cell. Mol. Life Sci.* **70**, 1307–1317 (2013).

37. Passaro, D. *et al.* Increased Vascular Permeability in the Bone Marrow Microenvironment Contributes to Disease Progression and Drug Response in Acute Myeloid Leukemia. *Cancer Cell* **32**, 324-341.e6 (2017).

38. Li, J. *et al.* Sensitizing leukemia stem cells to NF-κB inhibitor treatment *in vivo* by inactivation of both TNF and IL-1 signaling. *Oncotarget* **8**, 8420–8435 (2017).

39. Shafat, M. S. *et al.* Leukemic blasts program bone marrow adipocytes to generate a protumoral microenvironment. *Blood* **129**, 1320–1332 (2017).

40. Hanoun, M. *et al.* Acute Myelogenous Leukemia-Induced Sympathetic Neuropathy Promotes Malignancy in an Altered Hematopoietic Stem Cell Niche. *Cell Stem Cell* **15**, 365–375 (2014).

41. Griffin, J. *et al.* Secretion of interleukin-1 by acute myeloblastic leukemia cells in vitro induces endothelial cells to secrete colony stimulating factors. *Blood* **70**, 1218–1221 (1987).

42. Becker, P. S. Dependence of Acute Myeloid Leukemia on Adhesion within the Bone Marrow Microenvironment. *Sci. World J.* **2012**, 1–4 (2012).

43. De Kouchkovsky, I. & Abdul-Hay, M. 'Acute myeloid leukemia: a comprehensive review and 2016 update'. *Blood Cancer J.* **6**, e441–e441 (2016).

44. Higgins, A. & Shah, M. V. Genetic and Genomic Landscape of Secondary and Therapy-Related Acute Myeloid Leukemia. *Genes* **11**, 749 (2020).

45. Goel, H. *et al.* Molecular and genomic landscapes in secondary & therapy related acute myeloid leukemia.

46. Kennedy, V. E. & Smith, C. C. FLT3 Mutations in Acute Myeloid Leukemia: Key Concepts and Emerging Controversies. *Front. Oncol.* **10**, 612880 (2020).

47. Sakamoto, K. M. *et al.* Targeting novel signaling pathways for resistant acute myeloid leukemia. *Mol. Genet. Metab.* **114**, 397–402 (2015).

48. Burnett, A., Wetzler, M. & Löwenberg, B. Therapeutic Advances in Acute Myeloid Leukemia. *J. Clin. Oncol.* **29**, 487–494 (2011).

49. Ganzel, C. *et al.* Very poor long-term survival in past and more recent studies for relapsed AML patients: The ECOG-ACRIN experience. *Am. J. Hematol.* **93**, 1074–1081 (2018).

50. Shallis, R. M., Wang, R., Davidoff, A., Ma, X. & Zeidan, A. M. Epidemiology of acute myeloid leukemia: Recent progress and enduring challenges. *Blood Rev.* **36**, 70–87 (2019).

51. Gyurkocza, B. & Sandmaier, B. M. Conditioning regimens for hematopoietic cell transplantation: one size does not fit all. *Blood* **124**, 344–353 (2014).

52. Crawley, C. Outcomes of reduced-intensity transplantation for chronic myeloid leukemia: an analysis of prognostic factors from the Chronic Leukemia Working Party of the EBMT. *Blood* **106**, 2969–2976 (2005).

53. Warlick, E. *et al.* Reduced intensity conditioning is superior to nonmyeloablative conditioning for older chronic myelogenous leukemia patients undergoing hematopoietic cell transplant during the tyrosine kinase inhibitor era. *Blood* **119**, 4083–4090 (2012).

54. Thomas, E. D. *et al.* Marrow transplantation for acute nonlymphoblastic leukemia in first remission using fractionated or single-dose irradiation. *Int. J. Radiat. Oncol.* **8**, 817–821 (1982).

55. Petersen, F. B. *et al.* Marrow transplantation following escalating doses of fractionated total body irradiation and cyclophosphamide—a phase I trial. *Int. J. Radiat. Oncol.* **23**, 1027–1032 (1992).

56. Hoy, S. M. & Lyseng-Williamson, K. A. Intravenous Busulfan: In the Conditioning Treatment of Pediatric Patients Prior to Hematopoietic Stem Cell Transplantation. *Pediatr. Drugs* **9**, 271–278 (2007).

57. Chen, X., Liang, M. & Wang, D. Progress on the study of the mechanism of busulfan cytotoxicity. *Cytotechnology* **70**, 497–502 (2018).

58. Bornhäuser, M. *et al.* Conditioning with fludarabine and targeted busulfan for transplantation of allogeneic hematopoietic stem cells. *Blood* **102**, 820–826 (2003).

59. Zitvogel, L., Apetoh, L., Ghiringhelli, F. & Kroemer, G. Immunological aspects of cancer chemotherapy. *Nat. Rev. Immunol.* **8**, 59–73 (2008).

60. Lutsiak, M. E. C. *et al.* Inhibition of CD4ƨ25ƨ T regulatory cell function implicated in enhanced immune response by low-dose cyclophosphamide. **105**, (2005).

61. Andersson, B. S. *et al.* Once Daily i.v. Busulfan and Fludarabine (i.v. Bu-Flu) Compares Favorably with i.v. Busulfan and Cyclophosphamide (i.v. BuCy2) as Pretransplant Conditioning Therapy in AML/MDS. *Biol. Blood Marrow Transplant.* **14**, 672–684 (2008).

62. Lee, J. H. *et al.* Fludarabine-based myeloablative regimen as pretransplant conditioning therapy in adult acute leukemia/myelodysplastic syndrome: comparison with oral or intravenous busulfan with cyclophosphamide. *Korean J. Hematol.* **45**, 102 (2010).

63. Sullivan, K. *et al.* Influence of acute and chronic graft-versus-host disease on relapse and survival after bone marrow transplantation from HLA-identical siblings as treatment of acute and chronic leukemia [published erratum appears in Blood 1989 Aug 15;74(3):1180]. *Blood* **73**, 1720–1728 (1989).

64. Scott, B. L. *et al.* Myeloablative Versus Reduced-Intensity Hematopoietic Cell Transplantation for Acute Myeloid Leukemia and Myelodysplastic Syndromes. *J. Clin. Oncol.* **35**, 1154–1161 (2017).

65. Luger, S. M. *et al.* Similar outcomes using myeloablative vs reduced-intensity allogeneic transplant preparative regimens for AML or MDS. *Bone Marrow Transplant.* **47**, 203–211 (2012).

66. Flynn, C. M. *et al.* Reduced intensity compared with high dose conditioning for allotransplantation in acute myeloid leukemia and myelodysplastic syndrome: A comparative clinical analysis. *Am. J. Hematol.* **82**, 867–872 (2007).

67. Bartram, J., Patel, B. & Fielding, A. K. Monitoring MRD in ALL: Methodologies, technical aspects and optimal time points for measurement. *Semin. Hematol.* **57**, 142–148 (2020).

68. Heuser, M. *et al.* 2021 Update on MRD in acute myeloid leukemia: a consensus document from the European LeukemiaNet MRD Working Party. *Blood* **138**, 2753–2767 (2021).

69. Yates, J. W. et al. Cytosine arabinoside (NSC-63878) and daunorubicin (NSC-83142) therapy in acute nonlymphocytic leukemia. Cancer chemotherapy reports, 57(4), 485-488 (1973).

70. Yilmaz, M. *et al.* Hypomethylating agent and venetoclax with FLT3 inhibitor "triplet" therapy in older/unfit patients with FLT3 mutated AML. *Blood Cancer J.* **12**, 77 (2022).

71. Raghuveer Singh Mali *et al.* Venetoclax combines synergistically with FLT3 inhibition to effectively target leukemic cells in FLT3-ITD+ acute myeloid leukemia models. *Haematologica* **106**, 1034–1046 (2020).

72. Peci, F. *et al.* The cellular composition and function of the bone marrow niche after allogeneic hematopoietic cell transplantation. *Bone Marrow Transplant.* **57**, 1357–1364 (2022).

73. Pinho, S. & Frenette, P. S. Haematopoietic stem cell activity and interactions with the niche. *Nat. Rev. Mol. Cell Biol.* **20**, 303–320 (2019).

74. Hooper, A. T. *et al.* Engraftment and Reconstitution of Hematopoiesis Is Dependent on VEGFR2-Mediated Regeneration of Sinusoidal Endothelial Cells. *Cell Stem Cell* **4**, 263–274 (2009).

75. Kopp, H.-G. *et al.* Tie2 activation contributes to hemangiogenic regeneration after myelosuppression. *Blood* **106**, 505–513 (2005).

76. Chen, Q. *et al.* Apelin+ Endothelial Niche Cells Control Hematopoiesis and Mediate Vascular Regeneration after Myeloablative Injury. *Cell Stem Cell* **25**, 768-783.e6 (2019).

77. Guo, P. *et al.* Endothelial jagged-2 sustains hematopoietic stem and progenitor reconstitution after myelosuppression. *J. Clin. Invest.* **127**, 4242–4256 (2017).

78. Rieger, K. *et al.* Mesenchymal stem cells remain of host origin even a long time after allogeneic peripheral blood stem cell or bone marrow transplantation. *Exp. Hematol.* **33**, 605–611 (2005).

79. Preciado, S. *et al.* Mesenchymal Stromal Cell Irradiation Interferes with the Adipogenic/Osteogenic Differentiation Balance and Improves Their Hematopoietic-Supporting Ability. *Biol. Blood Marrow Transplant.* **24**, 443–451 (2018).

80. Sugrue, T., Lowndes, N. F. & Ceredig, R. Mesenchymal stromal cells: radio-resistant members of the bone marrow. *Immunol. Cell Biol.* **91**, 5–11 (2013).

81. Arai, F. *et al.* Tie2/Angiopoietin-1 Signaling Regulates Hematopoietic Stem Cell Quiescence in the Bone Marrow Niche. *Cell* **118**, 149–161 (2004).

82. Greenbaum, A. *et al.* CXCL12 in early mesenchymal progenitors is required for haematopoietic stem-cell maintenance. *Nature* **495**, 227–230 (2013).

83. Nombela-Arrieta, C. *et al.* Quantitative imaging of haematopoietic stem and progenitor cell localization and hypoxic status in the bone marrow microenvironment. *Nat. Cell Biol.* **15**, 533–543 (2013).

84. McClune, B., Majhail, N. S. & Flowers, M. E. D. Bone Loss and Avascular Necrosis of Bone After Hematopoietic Cell Transplantation. *Semin. Hematol.* **49**, 59–65 (2012).

85. Gencheva, M. *et al.* Bone marrow osteoblast vulnerability to chemotherapy. *Eur. J. Haematol.* **90**, 469–478 (2013).

86. Rellick, S. L. *et al.* Bone Marrow Osteoblast Damage by Chemotherapeutic Agents. *PLoS ONE* **7**, e30758 (2012).

87. Lau, P., Baumstark-Khan, C., Hellweg, C. E. & Reitz, G. X-irradiation-induced cell cycle delay and DNA double-strand breaks in the murine osteoblastic cell line OCT-1. *Radiat. Environ. Biophys.* **49**, 271–280 (2010).

88. Méndez-Ferrer, S., Lucas, D., Battista, M. & Frenette, P. S. Haematopoietic stem cell release is regulated by circadian oscillations. *Nature* **452**, 442–447 (2008).

89. Lucas, D. *et al.* Chemotherapy-induced bone marrow nerve injury impairs hematopoietic regeneration. *Nat. Med.* **19**, 695–703 (2013).

90. Delanian, S., Lefaix, J.-L. & Pradat, P.-F. Radiation-induced neuropathy in cancer survivors. *Radiother. Oncol.* **105**, 273–282 (2012).

91. Kanate, A. S. *et al.* Indications for Hematopoietic Cell Transplantation and Immune Effector Cell Therapy: Guidelines from the American Society for Transplantation and Cellular Therapy. *Biol. Blood Marrow Transplant.* **26**, 1247–1256 (2020).

92. D'Souza, A., Lee, S., Zhu, X. & Pasquini, M. Current Use and Trends in Hematopoietic Cell Transplantation in the United States. *Biol. Blood Marrow Transplant.* **23**, 1417–1421 (2017).

93. Gyurkocza, B. & Sandmaier, B. M. Conditioning regimens for hematopoietic cell transplantation: one size does not fit all. *Blood* **124**, 344–353 (2014).

94. Chhabra, S. *et al.* Myeloablative vs reduced-intensity conditioning allogeneic hematopoietic cell transplantation for chronic myeloid leukemia. *Blood Adv.* **2**, 2922–2936 (2018).

95. Du, W. & Cao, X. Cytotoxic Pathways in Allogeneic Hematopoietic Cell Transplantation. *Front. Immunol.* **9**, 2979 (2018).

96. Nagler, A. & Shimoni, A. Conditioning. in *The EBMT Handbook* (eds. Carreras, E., Dufour, C., Mohty, M. & Kröger, N.) 99–107 (Springer International Publishing, Cham, 2019). doi:10.1007/978-3-030-02278-5_13.

97. Chiesa, R. & Veys, P. Reduced-intensity conditioning for allogeneic stem cell transplant in primary immune deficiencies. *Expert Rev. Clin. Immunol.* **8**, 255–267 (2012).

98. Yanada, M., Harada, K., Shimomura, Y., Arai, Y. & Konuma, T. Conditioning regimens for allogeneic hematopoietic cell transplantation in acute myeloid leukemia: Real-world data from the Japanese registry studies. *Front. Oncol.* **12**, 1050633 (2022).

99. Sengsayadeth, S. *et al.* Reduced intensity conditioning allogeneic hematopoietic cell transplantation for adult acute myeloid leukemia in complete remission - a review from the Acute Leukemia Working Party of the EBMT. *Haematologica* **100**, 859–869 (2015).

100. Çiftçiler, R. *et al.* Comparison of Myeloablative Versus Reduced-Intensity Conditioning Regimens for Allogeneic Hematopoietic Stem Cell Transplantation in Acute Myeloid Leukemia: A Cohort Study. *Turk. J. Hematol.* **36**, 88–96 (2019).

101. Barrett, A. J. & Battiwalla, M. Relapse after allogeneic stem cell transplantation. *Expert Rev. Hematol.* **3**, 429–441 (2010).

102. Cavazzana-Calvo, M. *et al.* Long-term T-cell reconstitution after hematopoietic stem-cell transplantation in primary T-cell–immunodeficient patients is associated with myeloid chimerism and possibly the primary disease phenotype. *Blood* **109**, 4575–4581 (2007).

103. Zou, Q. *et al.* Bone marrow stem cell dysfunction in radiation-induced abscopal bone loss. *J. Orthop. Surg.* **11**, 3 (2016).

104. Kouam, P. N., Rezniczek, G. A., Adamietz, I. A. & Bühler, H. Ionizing radiation increases the endothelial permeability and the transendothelial migration of tumor cells through ADAM10-activation and subsequent degradation of VE-cadherin. *BMC Cancer* **19**, 958 (2019).

105. Slayton, W. B. *et al.* The Role of the Donor in the Repair of the Marrow Vascular Niche Following Hematopoietic Stem Cell Transplant. *Stem Cells* **25**, 2945–2955 (2007).

106. Zhou, B. O. *et al.* Bone marrow adipocytes promote the regeneration of stem cells and haematopoiesis by secreting SCF. *Nat. Cell Biol.* **19**, 891–903 (2017).

107. Fletcher, R. E. *et al.* Posttransplantation cyclophosphamide expands functional myeloid-derived suppressor cells and indirectly influences Tregs. *Blood Adv.* **7**, 1117–1129 (2023).

108. Li, X.-M., Hu, Z., Jorgenson, M. L., Wingard, J. R. & Slayton, W. B. Bone marrow sinusoidal endothelial cells undergo nonapoptotic cell death and are replaced by proliferating sinusoidal cells in situ to maintain the vascular niche following lethal irradiation. *Exp. Hematol.* **36**, 1143-1156.e3 (2008).

109. Kondo, H. *et al.* Total-Body Irradiation of Postpubertal Mice with ^{137} Cs Acutely Compromises the Microarchitecture of Cancellous Bone and Increases Osteoclasts. *Radiat. Res.* **171**, 283–289 (2009).

110. Lee, G.-Y., Jeong, S.-Y., Lee, H.-R. & Oh, I.-H. Age-related differences in the bone marrow stem cell niche generate specialized microenvironments for the distinct regulation of normal hematopoietic and leukemia stem cells. *Sci. Rep.* **9**, 1007 (2019).

111. Kusumbe, A. P., Ramasamy, S. K. & Adams, R. H. Coupling of angiogenesis and osteogenesis by a specific vessel subtype in bone. *Nature* **507**, 323–328 (2014).

112. Porto, M. L. *et al.* Reactive oxygen species contribute to dysfunction of bone marrow hematopoietic stem cells in aged C57BL/6 J mice. *J. Biomed. Sci.* **22**, 97 (2015).

113. Ogawa, T., Kitagawa, M. & Hirokawa, K. Age-related changes of human bone marrow: a histometric estimation of proliferative cells, apoptotic cells, T cells, B cells and macrophages. *Mech. Ageing Dev.* **117**, 57–68 (2000).

114. Kusumbe, A. P. *et al.* Age-dependent modulation of vascular niches for haematopoietic stem cells. *Nature* **532**, 380–384 (2016).

115. Connor, K. M. *et al.* Understanding metabolic changes in aging bone marrow. *Exp. Hematol. Oncol.* **7**, 13 (2018).

116. Rübe, C. E. *et al.* Accumulation of DNA Damage in Hematopoietic Stem and Progenitor Cells during Human Aging. *PLoS ONE* **6**, e17487 (2011).

117. Cohen, H. J., Pieper, C. F., Harris, T., Rao, K. M. K. & Currie, M. S. The Association of Plasma IL-6 Levels With Functional Disability in Community-Dwelling Elderly. *J. Gerontol. A. Biol. Sci. Med. Sci.* **52A**, M201–M208 (1997).

118. Hasegawa, Y., Sawada, M., Ozaki, N., Inagaki, T. & Suzumura, A. Increased Soluble Tumor Necrosis Factor Receptor Levels in the Serum of Elderly People. *Gerontology* **46**, 185–188 (2000).

119. Kovtonyuk, L. V., Fritsch, K., Feng, X., Manz, M. G. & Takizawa, H. Inflamm-Aging of Hematopoiesis, Hematopoietic Stem Cells, and the Bone Marrow Microenvironment. *Front. Immunol.* **7**, (2016).

120. Beerman, I., Seita, J., Inlay, M. A., Weissman, I. L. & Rossi, D. J. Quiescent Hematopoietic Stem Cells Accumulate DNA Damage during Aging that Is Repaired upon Entry into Cell Cycle. *Cell Stem Cell* **15**, 37–50 (2014).

121. Ciurea, S. O. & Andersson, B. S. Busulfan in Hematopoietic Stem Cell Transplantation. *Biol. Blood Marrow Transplant.* **15**, 523–536 (2009).

122. Kebriaei, P. *et al.* Intravenous Busulfan Compared with Total Body Irradiation Pretransplant Conditioning for Adults with Acute Lymphoblastic Leukemia. *Biol. Blood Marrow Transplant.* **24**, 726–733 (2018).

123. Socié, G. *et al.* Busulfan plus cyclophosphamide compared with total-body irradiation plus cyclophosphamide before marrow transplantation for myeloid leukemia: long-term follow-up of 4 randomized studies. *Blood* **98**, 3569–3574 (2001).

124. Capotondo, A. *et al.* Brain conditioning is instrumental for successful microglia reconstitution following hematopoietic stem cell transplantation. *Proc. Natl. Acad. Sci.* **109**, 15018–15023 (2012).

125. Youshani, A. S. *et al.* Non-myeloablative busulfan chimeric mouse models are less pro-inflammatory than head-shielded irradiation for studying immune cell interactions in brain tumours. *J. Neuroinflammation* **16**, 25 (2019).

126. Wilkinson, F. L. *et al.* Busulfan Conditioning Enhances Engraftment of Hematopoietic Donor-derived Cells in the Brain Compared With Irradiation. *Mol. Ther.* **21**, 868–876 (2013).

127. Montecino-Rodriguez, E. & Dorshkind, K. Use of Busulfan to Condition Mice for Bone Marrow Transplantation. *STAR Protoc.* **1**, 100159 (2020).

128. Chicana, B. *et al.* Deletion of Vhl in Dmp1-Expressing Cells Causes Microenvironmental Impairment of B Cell Lymphopoiesis. *Front. Immunol.* **13**, 780945 (2022).

129. Sipkins, D. A. *et al.* In vivo imaging of specialized bone marrow endothelial microdomains for tumour engraftment. *Nature* **435**, 969–973 (2005).

130. Wu, J. W. *et al.* Intravital fluorescence microscopy with negative contrast. *PLOS ONE* **16**, e0255204 (2021).

131. Itkin, T. *et al.* Distinct bone marrow blood vessels differentially regulate haematopoiesis. *Nature* **532**, 323–328 (2016).

132. *Intravital Imaging of Dynamic Bone and Immune Systems*. vol. 1763 (Springer New York, New York, NY, 2018).

133. Kim, T. N. *et al.* Line-Scanning Particle Image Velocimetry: An Optical Approach for Quantifying a Wide Range of Blood Flow Speeds in Live Animals. *PLoS ONE* **7**, e38590 (2012).

134. Garcia-Perez, L. *et al.* Combining Mobilizing Agents with Busulfan to Reduce Chemotherapy-Based Conditioning for Hematopoietic Stem Cell Transplantation. *Cells* **10**, 1077 (2021).

135. Andrade, J. *et al.* Effects of Sublethal Irradiation on Patterns of Engraftment after Murine Bone Marrow Transplantation. *Biol. Blood Marrow Transplant.* **17**, 608–619 (2011).

136. Yanir, A., Schulz, A., Lawitschka, A., Nierkens, S. & Eyrich, M. Immune Reconstitution After Allogeneic Haematopoietic Cell Transplantation: From Observational Studies to Targeted Interventions. *Front. Pediatr.* **9**, 786017 (2022).

137. Van Os, R., Konings, A. W. T. & Down, J. D. Compromising Effect of Low Dose-rate Total Body Irradiation on Allogeneic Bone Marrow Engraftment. *Int. J. Radiat. Biol.* **64**, 761–770 (1993).

138. Down, J., Tarbell, N., Thames, H. & Mauch, P. Syngeneic and allogeneic bone marrow engraftment after total body irradiation: dependence on dose, dose rate, and fractionation. *Blood* **77**, 661–669 (1991).

139. *The European Blood and Marrow Transplantation Textbook for Nurses*. (Springer International Publishing, Cham, 2018). doi:10.1007/978-3-319-50026-3.

140. Griffin, J. M., Healy, F. M., Dahal, L. N., Floisand, Y. & Woolley, J. F. Worked to the bone: antibody-based conditioning as the future of transplant biology. *J. Hematol. Oncol.J Hematol Oncol* **15**, 65 (2022).

141. Sudo, T. *et al.* Group 2 innate lymphoid cells support hematopoietic recovery under stress conditions. *J. Exp. Med.* **218**, e20200817 (2021).

142. Singh, P., Kacena, M. A., Orschell, C. M. & Pelus, L. M. Aging-Related Reduced Expression of CXCR4 on Bone Marrow Mesenchymal Stromal Cells Contributes to Hematopoietic Stem and Progenitor Cell Defects. *Stem Cell Rev. Rep.* **16**, 684–692 (2020).

143. Ellis, S. L. *et al.* The relationship between bone, hemopoietic stem cells, and vasculature. *Blood* **118**, 1516–1524 (2011).

144. Saçma, M. *et al.* Haematopoietic stem cells in perisinusoidal niches are protected from ageing. *Nat. Cell Biol.* **21**, 1309–1320 (2019).

145. Ho, Y.-H. *et al.* Remodeling of Bone Marrow Hematopoietic Stem Cell Niches Promotes Myeloid Cell Expansion during Premature or Physiological Aging. *Cell Stem Cell* **25**, 407-418.e6 (2019).

146. Maryanovich, M. *et al.* Adrenergic nerve degeneration in bone marrow drives aging of the hematopoietic stem cell niche. *Nat. Med.* **24**, 782–791 (2018).

147. Ferrucci, L. *et al.* The origins of age-related proinflammatory state. *Blood* **105**, 2294–2299 (2005).

148. Mendelson, A. & Frenette, P. S. Hematopoietic stem cell niche maintenance during homeostasis and regeneration. *Nat. Med.* **20**, 833–846 (2014).

149. Siclari, V. A. *et al.* Mesenchymal progenitors residing close to the bone surface are functionally distinct from those in the central bone marrow. *Bone* **53**, 575–586 (2013).

150. Naveiras, O. *et al.* Bone-marrow adipocytes as negative regulators of the haematopoietic microenvironment. *Nature* **460**, 259–263 (2009).

151. Yao, Z. *et al.* Therapy-Induced Senescence Drives Bone Loss. *Cancer Res.* **80**, 1171–1182 (2020).

152. Green, D. E., Adler, B. J., Chan, M. E. & Rubin, C. T. Devastation of adult stem cell pools by irradiation precedes collapse of trabecular bone quality and quantity. *J. Bone Miner. Res.* **27**, 749–759 (2012).

153. Kang, M. I. *et al.* The short-term changes of bone mineral metabolism following bone marrow transplantation. *Bone* **26**, 275–279 (2000).

154. Mas-Bargues, C. *et al.* Relevance of Oxygen Concentration in Stem Cell Culture for Regenerative Medicine. *Int. J. Mol. Sci.* **20**, 1195 (2019).

155. Wang, L. D. & Wagers, A. J. Dynamic niches in the origination and differentiation of haematopoietic stem cells. *Nat. Rev. Mol. Cell Biol.* **12**, 643–655 (2011).

156. Mohyeldin, A., Garzón-Muvdi, T. & Quiñones-Hinojosa, A. Oxygen in Stem Cell Biology: A Critical Component of the Stem Cell Niche. *Cell Stem Cell* **7**, 150–161 (2010).

157. Spencer, J. A. *et al.* Direct measurement of local oxygen concentration in the bone marrow of live animals. *Nature* **508**, 269–273 (2014).

158. Xiao, Y. *et al.* Current insights into the bone marrow niche: From biology in vivo to bioengineering ex vivo. *Biomaterials* **286**, 121568 (2022).

159. Schipani, E., Wu, C., Rankin, E. B. & Giaccia, A. J. Regulation of Bone Marrow Angiogenesis by Osteoblasts during Bone Development and Homeostasis. *Front. Endocrinol.* **4**, (2013).

160. Clerici, W. J., Hensley, K., DiMartino, D. L. & Butterfield, D. A. Direct detection of ototoxicant-induced reactive oxygen species generation in cochlear explants. *Hear. Res.* **98**, 116–124 (1996).

161. *Stem Cell Mobilization: Methods and Protocols*. vol. 2017 (Springer New York, New York, NY, 2019).

162. Ceradini, D. J. *et al.* Progenitor cell trafficking is regulated by hypoxic gradients through HIF-1 induction of SDF-1. *Nat. Med.* **10**, 858–864 (2004).

163. Swartz, H. M. & Walczak, T. Developing in Vivo EPR Oximetry for Clinical use. in *Oxygen Transport to Tissue XX* (eds. Hudetz, A. G. & Bruley, D. F.) vol. 454 243–252 (Springer US, Boston, MA, 1998).

164. Le, Q.-T. & Courter, D. Clinical biomarkers for hypoxia targeting. *Cancer Metastasis Rev.* **27**, 351–362 (2008).

165. Wolfbeis, O. S. Luminescent sensing and imaging of oxygen: Fierce competition to the Clark electrode. *BioEssays* **37**, 921–928 (2015).

166. Borisov, S. M. Fundamentals of Quenched Phosphorescence O2 Sensing and Rational Design of Sensor Materials.

167. *Optical Imaging in Human Disease and Biological Research*. vol. 3233 (Springer Singapore, Singapore, 2021).

168. Dewhirst, M. W. *et al.* Quantification of longitudinal tissue pO2 gradients in window chamber tumours: impact on tumour hypoxia. *Br. J. Cancer* **79**, 1717–1722 (1999).

169. Niu, J., Peng, D. & Liu, L. Drug Resistance Mechanisms of Acute Myeloid Leukemia Stem Cells. *Front. Oncol.* **12**, 896426 (2022).

170. Driss, V. *et al.* Sub-clonal analysis of the murine C1498 acute myeloid leukaemia cell line reveals genomic and immunogenic diversity. *Immunol. Lett.* **192**, 27–34 (2017).

171. Battula, V. L. *et al.* AML-induced osteogenic differentiation in mesenchymal stromal cells supports leukemia growth. *JCI Insight* **2**, e90036 (2017).

172. Burnett, A., Wetzler, M. & Löwenberg, B. Therapeutic Advances in Acute Myeloid Leukemia. *J. Clin. Oncol.* **29**, 487–494 (2011).

173. Döhner, H., Weisdorf, D. J. & Bloomfield, C. D. Acute Myeloid Leukemia. *N. Engl. J. Med.* **373**, 1136–1152 (2015).

174. Frisch, B. J. *et al.* Functional inhibition of osteoblastic cells in an in vivo mouse model of myeloid leukemia. *Blood* **119**, 540–550 (2012).

175. Kim, Y.-W. *et al.* Defective Notch activation in microenvironment leads to myeloproliferative disease. *Blood* **112**, 4628–4638 (2008).

176. Konopleva, M. Y. & Jordan, C. T. Leukemia Stem Cells and Microenvironment: Biology and Therapeutic Targeting. *J. Clin. Oncol.* **29**, 591–599 (2011).

177. Wilson, A. & Trumpp, A. Bone-marrow haematopoietic-stem-cell niches. *Nat. Rev. Immunol.* **6**, 93–106 (2006).

178. Yazdani, Z., Mousavi, Z., Moradabadi, A. & Hassanshahi, G. Significance of CXCL12/CXCR4 Ligand/Receptor Axis in Various Aspects of Acute Myeloid Leukemia. *Cancer Manag. Res.* **Volume 12**, 2155–2165 (2020).

179. Cho, B.-S., Kim, H.-J. & Konopleva, M. Targeting the CXCL12/CXCR4 axis in acute myeloid leukemia: from bench to bedside. *Korean J. Intern. Med.* **32**, 248–257 (2017).

180. Pimenta, D. B. *et al.* The Bone Marrow Microenvironment Mechanisms in Acute Myeloid Leukemia. *Front. Cell Dev. Biol.* **9**, 764698 (2021).

181. Wegiel, B., Ekberg, J., Talasila, K. M., Jalili, S. & Persson, J. L. The role of VEGF and a functional link between VEGF and p27Kip1 in acute myeloid leukemia. *Leukemia* **23**, 251–261 (2009).

182. Stucki, A. *et al.* Endothelial cell activation by myeloblasts: molecular mechanisms of leukostasis and leukemic cell dissemination. *Blood* **97**, 2121–2129 (2001).

183. Zhou, J. *et al.* Osteopontin is required for the maintenance of leukemia stem cells in acute myeloid leukemia. *Biochem. Biophys. Res. Commun.* **600**, 29–34 (2022).

184. Duarte, D. *et al.* Inhibition of Endosteal Vascular Niche Remodeling Rescues Hematopoietic Stem Cell Loss in AML. *Cell Stem Cell* **22**, 64-77.e6 (2018).

185. Colmone, A. *et al.* Leukemic Cells Create Bone Marrow Niches That Disrupt the Behavior of Normal Hematopoietic Progenitor Cells. *Science* **322**, 1861–1865 (2008).

186. Lassailly, F., Foster, K., Lopez-Onieva, L., Currie, E. & Bonnet, D. Multimodal imaging reveals structural and functional heterogeneity in different bone marrow compartments: functional implications on hematopoietic stem cells. *Blood* **122**, 1730–1740 (2013).

187. Duarte, D. *et al.* Defining the *in vivo* characteristics of acute myeloid leukemia cells behavior by intravital imaging. *Immunol. Cell Biol.* **97**, 229–235 (2019).

188. Harris, A. C. *et al.* Comparison of pediatric allogeneic transplant outcomes using myeloablative busulfan with cyclophosphamide or fludarabine. *Blood Adv.* **2**, 1198–1206 (2018).

189. Nagler, A. *et al.* Allogeneic Hematopoietic Stem-Cell Transplantation for Acute Myeloid Leukemia in Remission: Comparison of Intravenous Busulfan Plus Cyclophosphamide (Cy) Versus Total-Body Irradiation Plus Cy As Conditioning Regimen—A Report From the Acute Leukemia Working Party of the European Group for Blood and Marrow Transplantation. *J. Clin. Oncol.* **31**, 3549–3556 (2013).

190. Mopin, A., Driss, V. & Brinster, C. A Detailed Protocol for Characterizing the Murine C1498 Cell Line and its Associated Leukemia Mouse Model. *J. Vis. Exp.* 54270 (2016) doi:10.3791/54270.

191. Chicana, B. *et al.* Deletion of Vhl in Dmp1-Expressing Cells Causes Microenvironmental Impairment of B Cell Lymphopoiesis. *Front. Immunol.* **13**, 780945 (2022).

192. Morimatsu, M. *et al.* Migration arrest of chemoresistant leukemia cells mediated by MRTF-SRF pathway. *Inflamm. Regen.* **40**, 15 (2020).

193. Ruzicka, M. *et al.* RIG-I-based immunotherapy enhances survival in preclinical AML models and sensitizes AML cells to checkpoint blockade. *Leukemia* **34**, 1017–1026 (2020).

194. Mopin, A. *et al.* Detection of residual and chemoresistant leukemic cells in an immune-competent mouse model of acute myeloid leukemia: Potential for unravelling their interactions with immunity. *PLOS ONE* **17**, e0267508 (2022).

195. Duy, C. *et al.* Chemotherapy Induces Senescence-Like Resilient Cells Capable of Initiating AML Recurrence. *Cancer Discov.* **11**, 1542–1561 (2021).

196. Ishikawa, F. *et al.* Chemotherapy-resistant human AML stem cells home to and engraft within the bone-marrow endosteal region. *Nat. Biotechnol.* **25**, 1315–1321 (2007).

197. Benito, J., Zeng, Z., Konopleva, M. & Wilson, W. R. Targeting hypoxia in the leukemia microenvironment. *Int. J. Hematol. Oncol.* **2**, 279–288 (2013).

198. Kim, C.-J. *et al.* Nuclear morphology predicts cell survival to cisplatin chemotherapy. *Neoplasia* **42**, 100906 (2023).

199. Iga, T. *et al.* Spatial heterogeneity of bone marrow endothelial cells unveils a distinct subtype in the epiphysis. *Nat. Cell Biol.* **25**, 1415–1425 (2023).

200. Li, J., Tan, J., Martino, M. M. & Lui, K. O. Regulatory T-Cells: Potential Regulator of Tissue Repair and Regeneration. *Front. Immunol.* **9**, 585 (2018).

201. Lužnik, Z., Anchouche, S., Dana, R. & Yin, J. Regulatory T Cells in Angiogenesis. *J. Immunol.* **205**, 2557–2565 (2020).

202. Kolabas, Z. I. *et al.* Distinct molecular profiles of skull bone marrow in health and neurological disorders. *Cell* **186**, 3706-3725.e29 (2023).

203. Kolabas, Z. I. *et al. Multi-Omics and 3D-Imaging Reveal Bone Heterogeneity and Unique Calvaria Cells in Neuroinflammation*. http://biorxiv.org/lookup/doi/10.1101/2021.12.24.473988 (2021) doi:10.1101/2021.12.24.473988.

204. Hao, F., Sholy, C., Wang, C., Cao, M. & Kang, X. The Role of T Cell Immunotherapy in Acute Myeloid Leukemia. *Cells* **10**, 3376 (2021).

205. Lamble, A. J. & Lind, E. F. Targeting the Immune Microenvironment in Acute Myeloid Leukemia: A Focus on T Cell Immunity. *Front. Oncol.* **8**, 213 (2018).